

PROPOSAL TO PAC38

Exclusive Vector Meson Electroproduction with CLAS12

H. Avakian³, J. Ball⁵, A. Biselli¹⁰, V. Burkert³, L. Elouadrhiri³, R. Ent³, A. Fradi^{1*},
F-X. Girod³, A. Goloskokov⁸, B. Guegan^{1,2}, M. Guidal^{1†*}, H.-S. Jo¹, K. Joo⁴, P. Kroll⁹, J-
M. Laget³, H. Moutarde⁵, A. Kubarovskiy^{2*}, V. Kubarovsky^{3,2}, C. Munoz¹², S. Niccolai¹,
K. Park³, B. Pire⁶, M. Price², S. Procureur⁵, F. Sabatie⁵, N. Saylor^{2,1}, D. Sokhan¹,
S. Stepanyan³, P. Stoler^{2†*}, L. Szymanowski^{6,7}, M. Ungaro⁴, E. Voutier¹¹, C. Weiss^{3*}

and the CLAS Collaboration

1 - Institut de Physique Nucleaire Orsay, France

2- Rensselaer Polytechnic Institute

3 - Jefferson Lab

4 - University of Connecticut

5 - IRFU/SPhN, Saclay, France

6 - CPHT, Ecole Polytechnique, CNRS. Palaiseau, France

7 - Soltan Institute, Warsaw, Poland

8 - Joint Institute for Nuclear Research, Moscow, Russia

9 - Wuppertal University, Wuppertal, Germany

10 - Fairfield University

11 - LPSC Grenoble, France

12 - Laboratoire de Physique Corpusculaire -Clermont-Ferrand, France

* spokespersons: A. Fradi, M. Guidal, A. Kubarovskiy, P. Stoler, C. Weiss

† contacts: M. Guidal and P. Stoler

Abstract

It is proposed to measure exclusive vector meson electroproduction with CLAS-12. The mesons which will be studied are the ϕ , ρ^0 , ρ^+ , and ω . The kinematic regions covered will be W from 2 GeV to 4.5 GeV, Q^2 from 1 to greater than 10 GeV² and $-t$ to greater than 10 GeV². The transition from soft physics to the dominance of QCD quarks and gluons will be explored. The ϕ and ρ mesons are complementary in that the electroproduction of the ρ is expected to be sensitive to primarily valence quark and quark antiquark correlations, while the ϕ is sensitive mainly to the distribution of gluons in the nucleon. The experiment will be run contemporaneously with the deeply virtual Compton scattering and pseudoscalar meson production. Many of the same physics issues, such as the approach to GPD and TDA descriptions of hard reactions, underly all three experiments. Because of the different characteristics of the final state particles, such as spin, parity, charge and mass, each will access different aspects of the underlying physics.

I. INTRODUCTION

Exclusive electroproduction processes $\gamma^*(Q^2) + N \rightarrow M + N$ ($M = \gamma, \text{meson}$) offer a unique opportunity to study nucleon structure as one varies both the size of the probe — the photon virtuality, Q^2 — and the momentum transfer to the nucleon, t . Such processes can reveal much more information about strong interaction dynamics and the internal structure of the nucleon and the produced meson than either inclusive electroproduction (Q^2 only) or elastic form factors ($t = -Q^2$). One may broadly organize the possible measurements into four kinematic regions:

- (1) Resonance region: $W < 2$ GeV, low to high Q^2 ,
- (2) Deep forward region: $W > 2$ GeV, high Q^2 , low t .
- (3) Large angle region: $W > 2$ GeV, high t /high u , low to high Q^2 .
- (4) Deep backward region: $W > 2$ GeV, low u , high Q^2 .

The different regions are governed by distinct reaction mechanisms and provide complementary information about meson and nucleon structure.

In exclusive processes at $Q^2 \gg 1 \text{ GeV}^2$ [at both low or high t , regions (2), (3) and (4)] one expects that the meson (and the nucleon in region (4)) is predominantly produced in configurations that are much smaller than the typical hadronic size, $R_{\text{had}} \sim 1 \text{ fm}$. This opens the prospect of describing the interaction of these configurations with the probe and the target on the basis of QCD, relating them to the universal partonic structure probed in other deep-inelastic processes. It is important to stress, however, that the basic idea of dominance of small-size configurations is more primary than specific QCD-based approaches (see below) and can be tested experimentally in a model-independent manner, e.g. by studying the change of kinematic dependences of the exclusive cross section with Q^2 , or by comparison of different reaction channels. Such reactions should therefore be analyzed in two stages: (a) Verify the approach to the small-size regime by testing model-independent features; (b) Learn about short-range nucleon and meson structure with the help of specific dynamical models.

In the limit of $Q^2 \rightarrow \infty$ and fixed x_B the asymptotic behavior of exclusive meson production at low t is governed by the pQCD hard scattering mechanism, closely related to that governing the asymptotic behavior of meson elastic form factors at high Q^2 [1, 2]. In this picture the small-size $q\bar{q}$ configurations making the meson are generated by perturbative one-gluon exchange acting on configurations of “normal” hadronic size. A QCD factorization theorem [3] states that the $\gamma^*N \rightarrow M + N$ amplitude can be expressed in terms of the generalized parton distributions (GPDs) in the nucleon [4–6], describing the emission/absorption of the active quark by the nucleon; the amplitude of the hard scattering process; and the distribution amplitude of the meson, describing the conversion of small-size $q\bar{q}$ pair to the physical meson in the final state. The factorization theorem provides the basic script for the theoretical analysis of such processes. In particular, it guarantees that the GPDs and distribution amplitudes (DA) are universal, process-independent objects that can be probed in other high-momentum transfer processes and calculated using lattice QCD.

There is strong evidence, however, that non-perturbative QCD interactions play an essential role in meson production at $Q^2 \sim \text{few GeV}^2$ studied at JLab, and possibly at all Q^2 where such reactions could currently be measured. This brings into focus issues such as soft QCD radiation (resummation, Sudakov suppression) and the non-perturbative vacuum structure of QCD. In particular, the spontaneous breaking of chiral symmetry in the QCD vacuum,

which is induced by non-perturbative forces with a characteristic range $\rho \ll R_{\text{had}} \sim 1 \text{ fm}$, may have a decisive influence on meson form factors [7] and exclusive meson production at JLab energies. The theoretical study of such non-perturbative QCD mechanisms in meson production is evolving and depends crucially on experimental input to discriminate between different scenarios.

In the collinear picture used to describe high- Q^2 meson production in QCD the process can happen in two distinct ways. In the first, a quark is “taken out” of the nucleon with momentum fraction $x_1 > 0$, undergoes a hard reaction, and is “put back” with momentum fraction $x_2 > 0$, with $x_1 - x_2 \equiv 2\xi = x_B/(x_B - 2)$ (see Fig. Ia). In this region the GPD behaves similarly to the parton densities measured in inclusive DIS. In the second, the nucleon emits a quark-antiquark pair which interacts with the photon to produce the outgoing pair, corresponding to $x_1 < 0$ and $x_2 > 0$ or vice versa (see Fig. Ib). Here the GPD describes the distribution amplitude for the emission of the $q\bar{q}$ pair by the nucleon. The GPDs naturally combine the two contributions; in fact, their behavior in the two regions is related in a subtle way by the requirement of Lorentz invariance (“polynomiality condition”). In the pQCD hard-scattering approach there is no principal difference between the two types of processes. When non-perturbative interactions come into play, however, the two types of processes can contribute very differently to the production amplitude. Theoretical arguments suggest that the “knockout” of a small-size $q\bar{q}$ pair, produced by non-perturbative interactions in the initial state, should account for a large part of the meson production amplitude in JLab kinematics, in channels where it is allowed by quantum numbers. A sizable number of small-size $q\bar{q}$ pairs with spin zero in the nucleon is expected due to the spontaneous chiral symmetry breaking [8]. In contrast, the scattering from a valence quark that has to produce the meson via non-perturbative interactions in the final state should be disfavored at low t . As $|t|$ is increased above $\sim 1 \text{ GeV}^2$ scattering from valence quarks should gradually become more important, as a large momentum has to be transferred to the nucleon. In this scenario meson production experiments could explore the role of correlated $q\bar{q}$ pairs in the nucleon — the imprint of chiral symmetry breaking in the QCD vacuum on the nucleon’s partonic structure.

An interesting “extreme” case is meson production in the backward region of small $|u|$ and high $|t|$ (see Fig. Ic). At high Q^2 this process corresponds to the removal of a small-size 3-quark system from the nucleon, leaving behind a state with mesonic quantum numbers

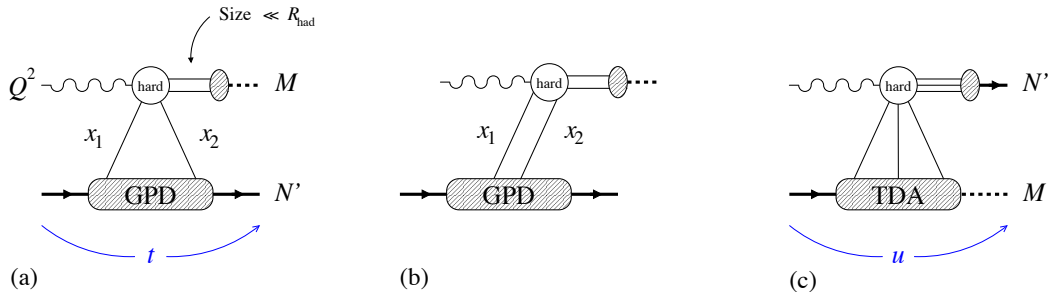


FIG. 1: (a, b) High- Q^2 exclusive meson production in the low- t , or forward, region: (a) Scattering from a quark (or antiquark); $x_{1,2}$ have the same sign. (b) Knockout of a quark-antiquark pair from the nucleon; $x_{1,2}$ have opposite sign. (c) High- Q^2 exclusive meson production in the low- u , or backward, region. The scattering process removes a three-quark system from the nucleon.

[9][23]. The pQCD description at $Q^2 \rightarrow \infty$ involves the so-called nucleon-to-meson transition distribution amplitude. Again, experience with nucleon form factors suggests that non-perturbative interactions play a paramount role at realistic Q^2 . The study of such processes, which have never been measured at high Q^2 , could provide interesting information about the coupling of small-size 3-quark clusters to mesonic systems and the role of chiral dynamics in hard processes, complementing studies of near-threshold meson production in high- Q^2 elastic form factors [11].

The electroproduction of vector mesons possesses a number of unique features which give it a special place in the extensive program of exclusive measurements planned with the 12 GeV Upgrade. The several available channels ($\phi, \rho^0, \rho^+, \omega$) allow one to separate different exchanges (quarks vs. gluons, flavor singlet vs. non-singlet) and lend themselves to model-independent comparative studies. ϕ meson production provides unique sensitivity to gluons even at JLab energies [12]; a GPD-based calculation including finite-size effects describes well the 6 GeV exclusive ϕ data [15]. Production of ϕ and ρ^0 was measured in the gluon-dominated (diffractive) regime at $W > 10$ GeV and is theoretically well understood, providing a reference point for the planned measurements at lower energies. At lower energies, hard electroproduction of ρ^0, ω , and ρ^+ , is sensitive to correlated $q\bar{q}$ pairs with scalar and pseudoscalar quantum numbers in the nucleon and provides a unique opportunity to test this dynamical picture. Finally, vector meson production has access to polarization observables through analysis of the decay angle distribution, which can provide information

on elements of the rho-meson density matrix which involve helicity amplitudes having both the lower and the higher twist contributions. Indeed, because the dominant chiral even distribution amplitude of a vector meson has twist 2 (respectively 3) for a longitudinally (respectively transversely) polarized state, the QCD calculation of the production amplitude is more involved for the latter case where factorization has not yet been proven. Model estimates exist however [13] and a consistent framework has been recently proposed [14]. To the extent that s-channel helicity conservation is approximately valid in some Q^2 range, one can also get information on the L/T ratio without costly measurements at different beam energies (Rosenbluth separation). The Q^2 dependence of the violations of s-channel helicity conservation are an important signal to be analyzed.

Here we propose a comprehensive study of exclusive vector meson electroproduction with CLAS12, including the ϕ , ρ^0 , ρ^+ and ω channels, in the kinematic region of high Q^2 , low and high $|t|$, as well as the backward region of small $|u|$. The objectives are to

- Verify the approach to the small-size regime by focusing on observables testing qualitative, model-independent features of the reaction mechanism, comparing different channels, and by making measurements over a wide range of $x_B(W)$, Q^2 and t ;
- Extract information about quark-antiquark correlations in the nucleon through measurements of ρ^0 , ρ^+ and ω production and comparison with theoretical model calculations;
- More exploratory, extract information about three quark correlations in the nucleon through measurements of ρ^0 , ρ^+ and ω production at small u and comparison with theoretical model calculations;
- Map the transverse spatial distribution of gluons in the nucleon through measurement of the t -dependence of the gluon GPD in ϕ production and relate it to high-energy data. More exploratory, map the transverse spatial distribution of strange quarks content of the nucleon through measurement of the u -dependence of the nucleon to meson TDA in ϕ backward production.

The proposed measurements would for the first time measure high- Q^2 exclusive vector meson production in both the low- $|t|$ region, $\lesssim 1 \text{ GeV}^2$, and the high- $|t|$ region, and thus provide

essential new information on the reaction mechanism. Comparison of low- and high- $|t|$ measurements is important to identify contributions from $q\bar{q}$ pair knockout. Furthermore, the proposed experiment would represent the first comprehensive study of vector meson channels in the kinematic region available with 12 GeV, enabling model-independent comparisons to clarify the reaction mechanism.

The proposed measurements complement the approved CLAS12 DVCS program (E12-09-003), which aims to extract information on the quark GPDs through the study of polarization observables in $N(e, e'\gamma)N'$. Insights into $q\bar{q}$ correlations in the nucleon and the flavor structure of GPDs H and E from vector meson production would directly impact on the analysis of DVCS data. They also complement the approved program in neutral pseudoscalar meson production (π^0, η, η' , E12-06-119), which probe meson production in a situation where spin-zero $q\bar{q}$ knockout is absent. The vector meson channels described in the present proposal would be measured simultaneously with these other channels.

The proposed study of $q\bar{q}$ correlations in the nucleon relate also to the planned measurements of π^+ production and the extraction of the pion form factor at high Q^2 (approved Hall C experiment E1206101). The pion pole term in the GPD \tilde{E} is an example of a specific $q\bar{q}$ correlation at peripheral transverse distances.

This proposal is organized as follows. In Sec. II we elaborate on the physics motivation. In Sec. III the experimental status of vector meson production is reviewed. Section IV presents the proposed program, and describe the observables to be studied and the proposed analysis. In Sec. V we present the projected experimental results with the upgraded CEBAF and CLAS12 based on extensive simulations.

II. PHYSICS MOTIVATION

This proposal aims at measuring the exclusive reactions $\gamma_v p \rightarrow \phi p$, $\gamma_v p \rightarrow \rho^0 p$, $\gamma_v p \rightarrow \rho^+ n$ and $\gamma_v p \rightarrow \omega p$ over as large a range of Q^2 , t and x_B as possible, as part of the CLAS12 program of experimentally mapping the characterization of nucleon structure invoking the framework of GPDs. It is important to point out at the very beginning that for meson production, the purely GPD approach, in which the interactions involving the virtual photon and the final state photon or meson are hard processes which are treated purely perturbatively, may occur at very high momentum transfers, so that at accessible momentum

transfers the GPD formalism may be taken as a basis with corrections from relatively soft processes. Thus, the primary goals of the present proposal is to observe the transition region characterizing the descriptions from soft to hard phenomena, and short range quark correlations within a nucleon. Evidence that the reach of CEBAF12/CLAS12 does indeed cover the transition interesting transition region is illustrated in Fig. 2. The left panel shows the results of a calculation by Ref. [16] of the evolution of the effective quark mass obtained using the Dyson-Schwinger equation, employing chiral symmetry, and tuned to LQCD calculations, to model the gluon dressing around the bare quark. The relative active quark momentum depends on Q^2 . One sees that in the kinematic region available the interaction transitions from one involving a soft dressed object toward the bare quark regime. The middle panel shows the t slope parameter B ($d\sigma/dt \propto \exp(Bt)$) as a function of Q^2 for the ρ , ϕ and J/Ψ vector mesons. The reduction in the t slope is an indication that the reaction region leading to the emission of a meson broadens and saturates to the full nucleon size where Regge type approaches have traditionally been effective in describing aspects of the data. The right panel shows the t slope parameter B as a function of W for ρ mesons. The reach of the proposed experiment for ρ and ϕ , indicated by the vertical red lines, appears to covers the region of x_B from about 0.8 down to 0.1, transitioning from the valence quark core to the $q - \bar{q}$ and gluon sea, which have larger spacial extents than the core.

A. Deep exclusive meson electroproduction and Generalized Parton Distributions.

In the deep-inelastic limit of high Q^2 , a QCD factorization theorem states that meson production is dominated by the scattering from a single, quasi-free quark in the proton [3]. In the leading-twist approximation, *i.e.*, in leading order of $1/Q^2$, the amplitude for longitudinal photon polarization can be expressed as a convolution of a hard scattering amplitude (describing the quark-level scattering process), the meson distribution amplitude (describing the hadronization of the outgoing quark/antiquark pair), and the generalized parton distributions in the proton (describing the emission/absorption of the “active” quark by the proton). The GPDs are universal, process-independent characteristics of the nucleon, which combine aspects of the usual parton densities with those of elastic form factors. The table below shows the relationships of the 4 GPDs to their underlying current structure. Their fascinating properties, and their potential for uniting traditional concepts of nucleon

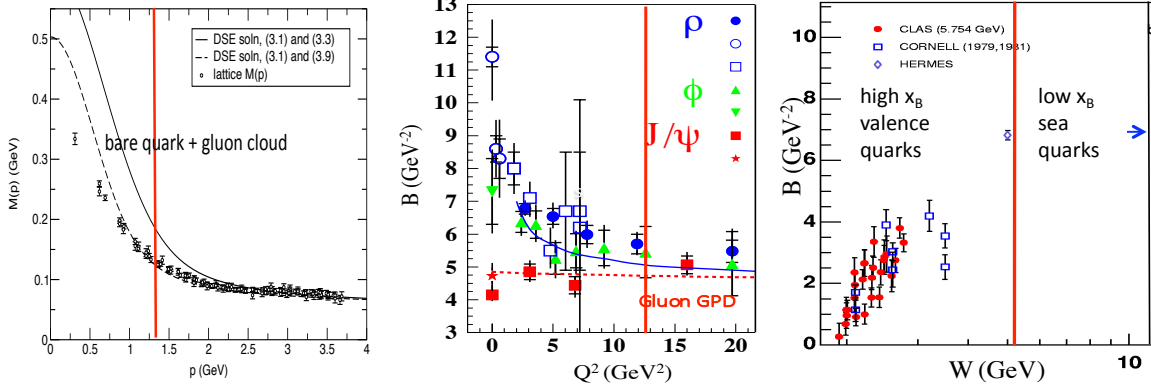


FIG. 2: Left: The results of a calculation by Ref. [16] of the evolution of the effective quark mass obtained using the Dyson-Schwinger equation, employing chiral symmetry and tuned to LQCD calculations, to model the gluon dressing around the bare quark. Center: The t slope parameter B ($d\sigma/dt \propto \exp(Bt)$) as a function of Q^2 for ρ , ϕ and J/ψ vector mesons. Right: The t slope parameter B as a function of W for ρ mesons. The kinematic reach of the proposed experiment are indicated by the vertical red lines.

structure in a single QCD-based description, have been widely discussed in recent years; see Refs. [17, 18, 21] for a review of the extensive literature. In the case of vector meson production the amplitude involves the vector-type GPDs, H and E , whose moments are related to the helicity conserving and helicity non-conserving nucleon form factors F_1 and F_2 , respectively.

Complementarily, for the pseudoscalar meson production the amplitude involves the axial vector-type GPDs, \tilde{H} and \tilde{E} , whose moments are related to the axial and pseudoscalar nucleon form factors.

	nucleon helicity	nucleon helicity
	non-flip	flip
$\Gamma = \gamma_\mu$ quarks unpolarized	H Dirac	E Pauli
$\gamma_\mu \gamma_5$ quarks polarized	\tilde{H} Axial	\tilde{E} Pseudoscalar

By measuring the vector meson production cross section in the deep-inelastic region we

can in principle extract information about the quark and gluon GPDs in the proton, and thus the momentum and spatial distribution of quarks and gluons, including flavor dependence.

The polarization of the virtual photon plays a crucial role in the transition from the soft to the hard regime. QCD factorization applies to the amplitudes for production by longitudinally polarized (L) photons, which dominate at large Q^2 [3]. The amplitudes for transversely polarized (T) photons can generally not be expressed in terms of GPDs. This is a consequence of the fact that longitudinal photons couple on average to configurations of substantially smaller transverse size than transverse ones. For testing the approach to the partonic reaction mechanism, and for extracting information about the GPDs, it is essential to separate contributions from L and T photons to the cross section. The differential cross section for exclusive meson production involving polarized electrons is given by

$$\begin{aligned} \frac{d\sigma}{dt d\phi} \propto & \sigma_T + \epsilon\sigma_L + \epsilon\sigma_{TT} \cos 2\phi^* \\ & + \sigma_{LT} \sqrt{2\epsilon(\epsilon+1)} \cos \phi^* + h \sqrt{2\epsilon(\epsilon+1)} \sigma_{LT'} \sin \phi^*, \end{aligned} \quad (1)$$

where ϕ^* is the meson's azimuthal angle and θ^* its polar angle with respect to the virtual photon in the plane of the virtual photon and scattered electron.

The quantity ϵ is the virtual photon polarization, h the beam helicity, and σ_L , σ_T , σ_{LT} and σ_{TT} are structure functions which depend on Q^2 , W and t . The unseparated cross sections can be measured up to $Q^2 \rightarrow 13 (\text{GeV}/c)^2$ and $-t \rightarrow 20 (\text{GeV}/c)^2$, depending on the W , Q^2 and the final state meson. The combinations $\sigma_T + \epsilon\sigma_L$, σ_{TT} and σ_{LT} can be separated via the azimuthal angle dependence of the cross section, and $\sigma_{LT'}$ via the single-beam spin asymmetry, which can be done over a wide range of Q^2 , W and t .

The energy range of JLab 12 will not allow high enough Q^2 to study the asymptotic scaling region for exclusive meson production, though all evidence indicated we will be ever to cover the all important transition regions, in which significant higher twist mechanisms, including the transverse and orbital angular momentum degrees of freedom play important roles.

In general, there are 8 spin-dependent quark-nucleon GPDs, 4 chiral even JPC 1^{++} and 4 chiral odd JPC 1^{+-} [18], and as noted [20], the quantum numbers and Dirac structure of π^0 electroproduction restrict the possible contributions of the 4 *chiral odd* GPDs, one of which, H_T , is related to the transversity distribution and the tensor charge. The roles they play in meson production has been dramatically demonstrated in refs [28] and [20]. This is an

exciting development, since the transverse photons are no longer considered an impediment for studying GPDs, but rather a window on the chiral odd GPDs and the transverse degrees of freedom to which they are associated.

The study of the Q^2 -dependence of both the chiral even GPDs, which to lowest order are accessed via longitudinal virtual photons, and the chiral odd GPDs, which are predominantly accessed via the transverse virtual photons will provide crucial tests of the approach to the hard mechanisms. This will require information about the four structure functions indicated above. For separation of σ_L and σ_T , the Rosenbluth technique is most often applied. However, a well known property of vector meson production is that, the measurement of the angular distribution of the meson's decay products in the helicity frame, under the assumption of s-channel helicity conservation, enables one to separate σ_L and σ_T . This technique has already been applied to 6 GeV CLAS data. This technique will be described in the ρ simulation section (V) below.

B. Backward meson u-channel electroproduction.

To study meson electroproduction, $\gamma^*(q)N(p_i) \rightarrow N'(p_2)M(p_f)$ at backward angles ($u = (p_i - p_f)^2$ fixed and small), in the Bjorken regime (Q^2 large and x_b fixed) one can write the amplitude in another factorized way (see Fig.3)

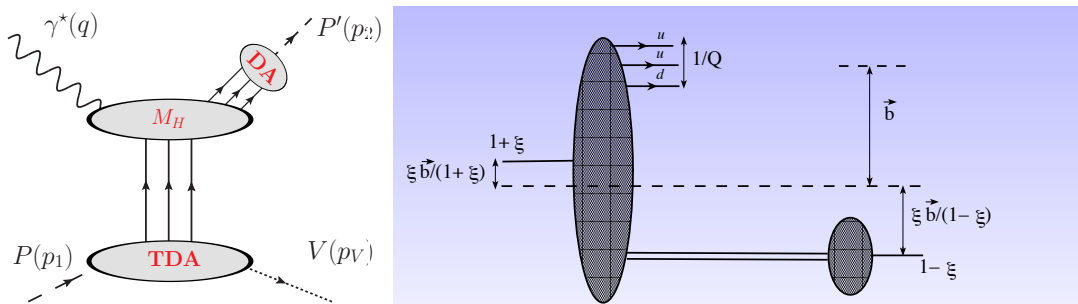


FIG. 3: Left: Schematic representation of u-channel meson production in terms of TDAs. Right: The interpretation in terms of a transverse impact parameter distribution.

where the hadronic structure enters through transition distribution amplitudes (TDAs) [22] defined as Fourier transforms of matrix elements of the three quark light cone non-local operator $\psi(z_1)\psi(z_2)\psi(z_3)$, the same operator that appears in baryonic Distribution Amplitudes (DAs). TDAs are universal non-perturbative objects describing the transitions between a

baryon and a meson or photon (e.g. $p \rightarrow \pi$, $p \rightarrow \rho$, $p \rightarrow \Phi$, $p \rightarrow \gamma$). They are an extension of the concept of GPDs and can be interpreted as the probability amplitude to find a vector meson in the nucleon at a given impact parameter.

Two cases are worth emphasizing : the case $M = \rho$ where two pions from the meson cloud in the nucleon resonate, and the case $M = \phi(1020)$ where one probes the strangeness content of the nucleon in a completely new way.

At the leading-twist accuracy, the u-channel QCD mechanism contributes only to σ_T .

The TDAs depend on the momentum fractions of the exchanged quarks x_1, x_2, x_3 . The TDAs also depend on $\Delta^2 = u$. A 2-dimensional Fourier transform $\vec{\Delta}_T \rightarrow \vec{b}_T$ allows one to express their impact representation $f(x_i, \xi, \vec{b}_T)$ and to determine the transverse location of the meson cloud inside the proton. In this way, we access information on the 3-D structure of the nucleon complementary to GPDs.

In the scaling regime, the amplitude for $\gamma_T^* P(p_1) \rightarrow P'(p_2) V^0(p_V)$ is a convolution of the proton DAs, a perturbatively-calculable hard-scattering amplitude and the TDAs. The scaling law at fixed ξ reads :

$$\sigma_T \approx \frac{\alpha_{em} \alpha_s^4}{\sqrt{(W^2 + M^2 + Q^2)^2 - 4W^2 M^2}} \times \frac{f(\xi)}{Q^6}. \quad (2)$$

Note that there is no difference in this scaling behaviour between the different polarization states of the produced vector meson, in contradistinction with the forward case in the GPD framework. A first estimate of the magnitude of cross sections in the case of the electro-production of a pseudoscalar meson is addressed in Ref.[23]. The techniques developed in Ref. [10] are more general and will enable rate estimates to be published soon.

III. CURRENT STATUS OF VECTOR MESON EXPERIMENTS

The current status of vector meson electroproduction is summarized in [12] and for ρ and ϕ electroproduction in [27] and [15] respectively. Data at high W have been obtained by Zeus and moderate W by Hermes. A program of experiments at lower W and low to moderate Q^2 has completed at Hall B with very interesting results.

Figure 4 shows the available ρ^0 longitudinal cross sections as functions of W for different values of Q^2 . Also shown are the results of GPD based calculations, VGG[24] and GK[13]. Several features should be noted. Both the VGG and GK parametrizations appear to satis-

factorily characterize the magnitude of the data at high W , while increasingly diverge as W decreases below 8 GeV. It is observed that the cross sections in Fig. 4 can also be accounted for by a Regge based calculation [29]. Regge based calculations are also successful in accounting for other meson electroproduction channels. This is not surprising because since the Regge formalism largely involves small t (large distance) exchanges of correlated $q\bar{q}$ pairs. Many of the phenomenological models of GPD's have been, and continue to be "Reggeized". Because of their empirical success, Regge descriptions will continue to play an important role to help guide construction of more phenomenological GPD models.

Reference [27] finds that the inclusion of an *ad hoc* "D" term introduced by in Ref. [25], which is meant to account for $q\bar{q}$ t -channel exchanges, can account rather well for the excess of cross section at lower W . However, to complicate the picture, the ρ^+ channel [26] also exhibits a large excess over the GPD prediction at lower W . This cannot be explained by introduction of a "D" term, which has isoscalar quantum numbers, since one cannot accommodate such a term for charged ρ^+ production.

The situation for ϕ production is quite different, and in several ways complementary to that of the ρ^0 . This is illustrated in Fig. 5 which shows the results of the GPD based calculations of Ref. [15]. For the ϕ , the calculations account for the available data at both low and high W , whereas for the ρ^0 , the calculation strongly underestimates the data at low W , similar to the result of Ref. [27].

It may be that the difference in behavior probably derives from the basic difference in reaction mechanism between the ρ^0 and ϕ . For vector meson production the reaction proceeds via two basic mechanisms, illustrated in Fig. 6. For the ϕ , due to its underlying dominant $s\bar{s}$ structure and the absence of strange quarks in the valence region, mechanisms which involve quark lines are highly suppressed. Thus, the ϕ production is highly dominated by the gluon GPD distribution in the nucleon, whereas at low W the ρ^0 production is probably dominated by quark GPDs with a much smaller proportion of gluon GPDs, whereas at high W both become dominated by multi-gluon *Pomeron* exchange.

Further evidence that ϕ electroproduction may already be gluon-GPD dominated may be found in the Q^2 dependence of the cross section already obtained at CLAS6 [30, 32], and shown in Fig. 7, in which a fit employing the function $1/(Q^2 + M_p^2)^n$ yields an exponent $n \sim 2.5$, which is not inconsistent with gluon-handbag expectations. But, this is controversial since power corrections strongly affect the value of n .

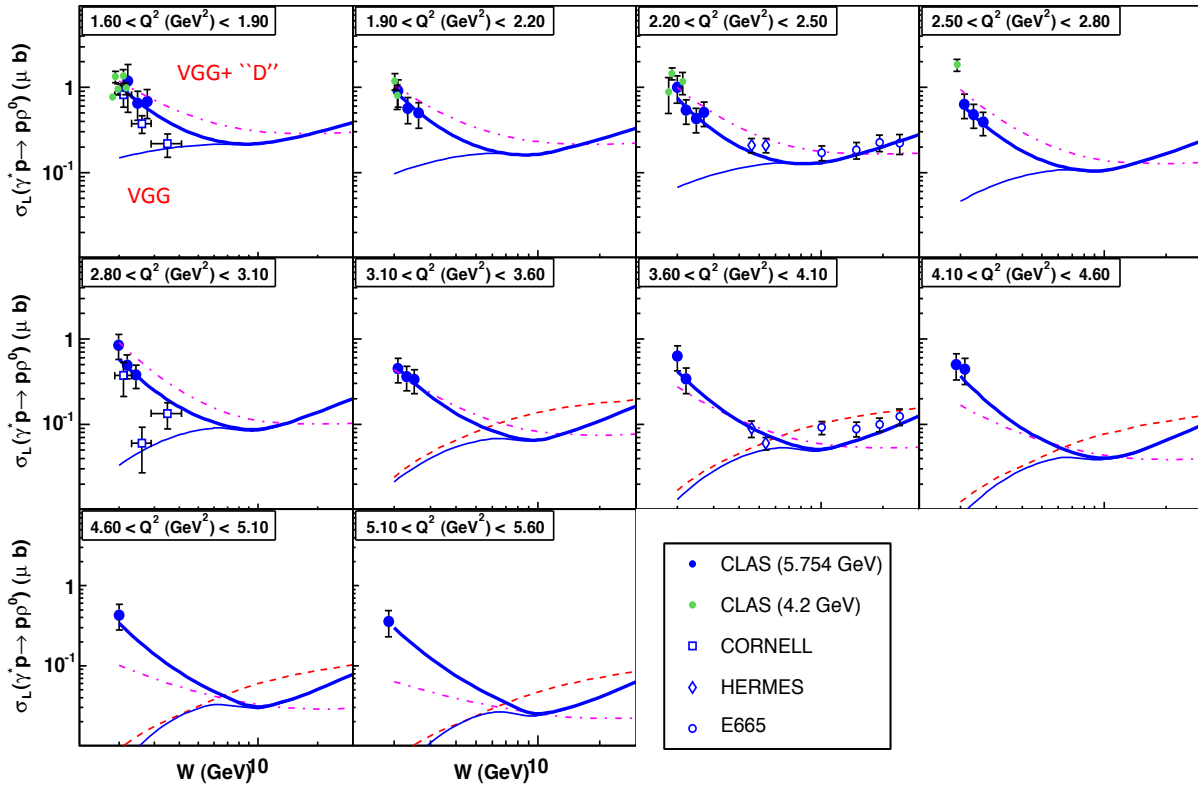


FIG. 4: Status of ρ^0 longitudinal electroproduction: σ_L vs. W for different values of Q^2 . The origins of the data are indicated by symbols corresponding to the panel on the lower right. The thin blue curve is the result of the “handbag” calculation with the VGG [24, 27] GPD parameterization. The thick blue curve is obtained the addition of a “D” term. The red dashed curve is due to a “handbag” calculation of Ref.[13], and the red dot-dashed curve is the result of a Regge based calculation of Ref.[29]

IV. PROPOSED EXPERIMENTAL PROGRAM

Much of the kinematic regions which cover the transition from soft physics to the dominance of QCD quarks and gluons are uniquely covered by the kinematic reach of JLab-12 and CLAS-12, that is:

- W from 2 GeV to greater than 5 GeV.
- Q^2 from 1 to greater than 12 or 13 GeV²
- $-(t - t_{min})$ from 0 to greater than 15 and in some kinematics approaching GeV²

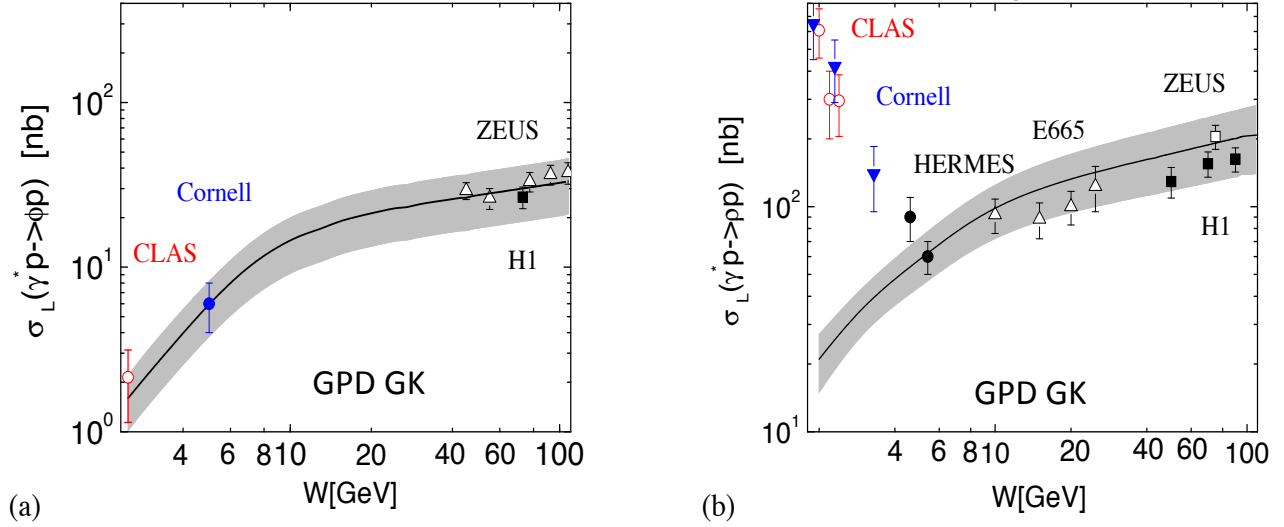


FIG. 5: Longitudinal cross sections for ϕ (left) and ρ^0 (right) electroproduction as functions of W .

The curves are the results of calculations by Goloskokov and Kroll

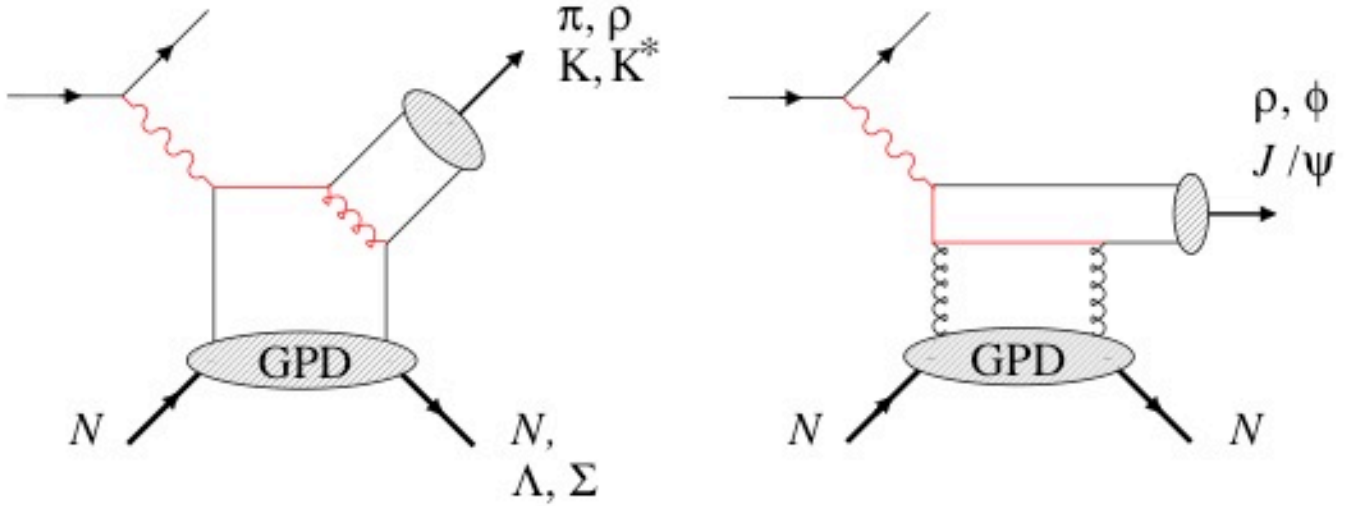


FIG. 6: Diagrams illustrating the leading quark and gluon contributions to the handbag mechanism.

For experiments aimed at studying the approach to the partonic regime and extracting information about the GPDs and u-channel production, it is necessary to characterize the contributions from the meson “dressing” at lowest Q^2 , its evolution with increasing Q^2 to soft processes involving quarks with gluon dressing, and finally to “peel” these away to approach the bare valence quark and gluon degrees of freedom. Since all these contributions have characteristic signatures as functions of Q^2, t and W we propose two basic strategies:

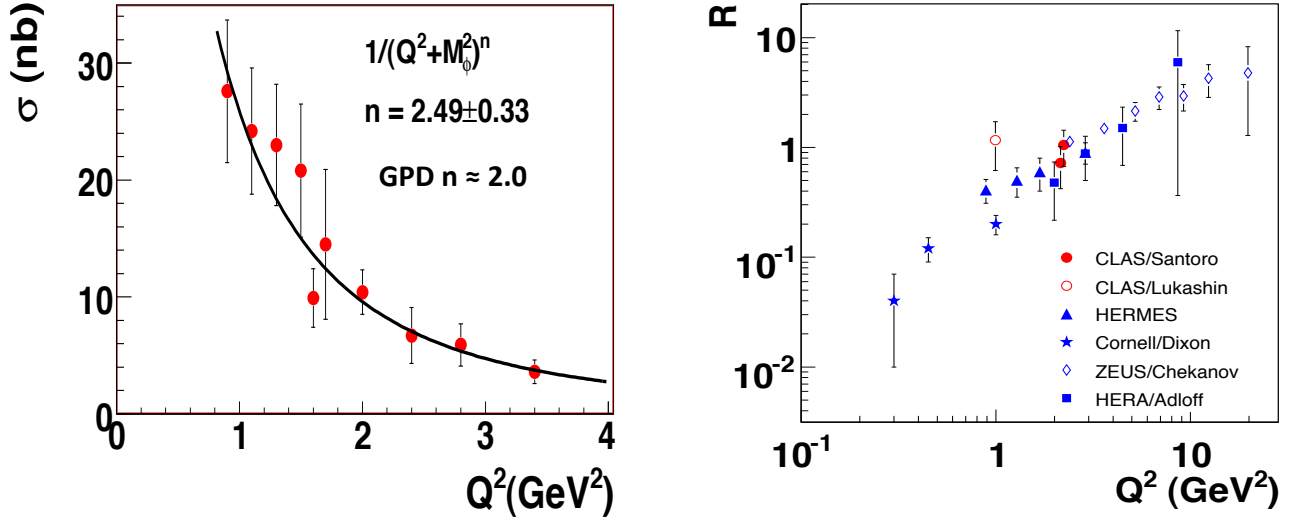


FIG. 7: Left: The Q^2 dependence of cross section for ϕ production obtained at CLAS6. The curve is a fit to the data with the function $1/(Q^2 + M_\phi^2)^n$ with an exponent $n \sim 2.5$. Right: Extracted R for ϕ

- (a) Choose observables and kinematics to maximize the contribution from small-size configurations,
- (b) Provide enough information for theoretical calculations to separate contributions from small-size and hadronic-size configurations.

Strategy (a) for t-channel production aimed at GPDs requires measurements at the highest possible Q^2 , and observables which select longitudinal photon polarization. For u-channel production one requires the highest possible $-t$ as well. Strategy (b) requires measurements over a wide range of Q^2 , W , and t , which allow one to observe systematic variations indicative of the transition from the hadronic to the partonic regime. The unique capabilities provided by the 12 GeV upgrade and the CLAS12 spectrometer make it possible to pursue both strategies at the same time.

First, as a basis we will measure the θ and ϕ dependence of the electroproduced mesons structure cross sections and separate $\sigma_T + \epsilon\sigma_L$, σ_{TT} and σ_{LT} from the ϕ dependence and σ'_{LT} from the beam polarization asymmetries. The σ_T and σ_L will be separated in two ways. The angular dependence of the decay products of the vector mesons will be measured to obtain $R = \sigma_L/\sigma_T$. We will also attempt to apply the Rosenbluth technique utilizing the

beam of 8 GeV already part of experiments E12-06-108 and E12-06-108 to obtain R over a limited kinematical range. The consistency between the two techniques will be required in their kinematic overlap regions, and serve as a check on each. We estimate that we will be able to obtain excellent statistics - see Section V on simulations..

Some of the measurements we plan to make include the following:

- Q^2 -dependence of cross sections. The simplest test of the approach to the hard reaction mechanism is provided by the Q^2 -dependence of the differential cross sections. QCD factorization predicts that the hard contribution to the (dominant) longitudinal cross section drops as $1/Q^6$, while the soft contributions to the longitudinal cross section, as well as the various transverse cross sections, drop at least as $1/Q^8$. We plan to test this prediction in the following ways:
 - Measure the unseparated differential cross section and see if it approaches a $1/Q^6$ behavior;
 - Measure the ratio σ_L/σ_T and see how fast it increases with Q^2 ;
 - Measure the interference cross sections σ_{TT} and σ_{LT} via the azimuthal angle dependence, and $\sigma_{LT'}$ via the single-spin asymmetry, and compare their Q^2 -dependence to that of the unseparated cross section.
- Measure the t -slope of the unseparated differential cross section, $d\sigma/dt$, in the forward peak; check if it decreases with Q^2 and becomes stable at large Q^2 .
- Measure the t -slopes of $d\sigma_L/dt$ and $d\sigma_T/dt$ separately. On general grounds one expects that L has a smaller t -slope than T , and that the L slope approaches a constant value at large Q^2 earlier than the unseparated cross section.
- In the case of u-channel production we will focus on the high $-t$ dependence of $d\sigma_T/dt$, and expect to observe a relative increase in cross section at the backward angles similar to what has already been observed for real photoproduction.
- Compare the t -slopes of ρ^0 , ρ^+ , ϕ and ω production as a function of Q^2 . To the extent that ρ^0 , ρ^+ and ω dominated by the quark GPD in the proton, while the ϕ is dominated by the gluon GPD, they should exhibit differences which are characteristic of the two mechanisms.

Present model calculations of the leading-twist contribution to pseudoscalar meson production amplitudes suffer from considerable theoretical uncertainties [35], caused both by the shortcomings of present ansätze for the GPDs, and by the uncertainties in the treatment of the hard scattering process (*e.g.* the choice of QCD scale). With the presently available data this uncertainty could not really be reduced by comparing with the data, since the relative importance of leading and higher-twist contributions in the data remained unclear. We expect a significant improvement of the situation with the data from the proposed experiment. The new data will extend our knowledge of longitudinal and transverse, as well as unseparated cross sections to substantially higher Q^2 and W , where the leading-twist contribution becomes more clearly visible. Even more important, the numerous tests of the reaction mechanism described above, and the detailed mapping of the Q^2 dependence of longitudinal as well as transverse cross sections, will allow us to tune phenomenological models containing both leading and higher-twist contributions, making it possible to extract information about the twist-2 contribution.

We stress that ϕ, ρ^0, ρ^+ and ω production discussed in the present proposal represents only one component of the extensive program of exclusive electroproduction measurements planned with CLAS12, and that the GPD analysis will, of course, include information from other channels such as DVCS and pseudoscalar meson production. Furthermore, these experiments which involve non-polarized targets will collect data simultaneously, so that a large group of collaborators will be working in concert to insure success of the program

The proposed measurements require clean identification of the reactions by way of detection of the products from the meson decay, in addition to the scattered electron and the recoil proton: $\phi \rightarrow K^+K^-$, $\rho^0 \rightarrow \pi^+\pi^-$, $\rho^+ \rightarrow \pi^+\pi^0$ and $\omega \rightarrow \pi^+\pi^-\pi^0$. Since we have measured and published cross sections for all these reactions with CLAS at $E_e = 5.75$ GeV this supports the feasibility indicated by our simulations at projected $E_\gamma = 11$ GeV. In particular, we expect reasonable rates for these reactions at the higher Q^2 values. Details of the simulations will be presented in Section VI.

V. ADDITIONAL OPPORTUNITIES

In this proposal, we have focused on the four main vector meson channels: ρ^0, ρ^+, ω and ϕ . Those have already been analyzed with the current CLAS detector and the 5.75

GeV electron beam and their detailed analysis is therefore "guaranteed". However, other channels whose nature or final state is very close to these channels can be measured. For instance, exclusive $f_0(980)$ and $f_2(1270)$ electroproduction, which have been seen in the 5.75 GeV $\pi^+\pi^-$ invariant mass spectra (see figure 20) shall also be analyzed. There are also factorization theorems and access to GPDs for these two scalar and tensor meson respectively [40–42]. Furthermore, the non-resonant 2-pion spectra could also be analyzed in terms of "Generalized Distribution Amplitudes", see Ref. [43, 44] for instance.

VI. CONCLUSION

Before passing to a discussion of the simulations we have carried out, which is quite lengthy, we summarize the gist of this proposal and the beam time requirements.

Based on these simulations (see Section VII below), we estimate that the measurement of the ρ^0 and ϕ exclusive electroproduction channels can be performed up to $Q^2 \approx 13 \text{ GeV}^2$, and ρ^+ and ω up to $Q^2 \approx 10 \text{ GeV}^2$, from essentially t_{min} to t_{max} for each Q^2 , and for x_B from ≈ 0.05 to 0.85 with the CLAS12 detector and the CEBAF 11 GeV beam. We will extract, for experimental observables W , x_B , Q^2 and t , differential cross sections, as well as L/T separated cross sections, ratios of cross sections for the different channels, etc... This experiment will provide a very large quantity of the most comprehensive data ever produced on vector meson electroproduction, and will provide a new level of stringent experimental constraints. This will further our understanding of the exclusive vector meson production on the nucleon in the valence region, which is currently poorly understood.

To carry out these measurement, we request the following running conditions :

- 1000 hours of beam time. The large amount of beam time is required by the decreasing count rates at high Q^2 and in the large t -large u region and the fact that multi-dimensional data analysis is necessary (for instance, the study of the decay angular distributions of the vector mesons to separate the longitudinal from the transverse parts of the cross section).
- LH_2 target
- $\mathcal{L} = 10^{35} \text{ cm}^{-2} \text{ s}^{-1}$
- Full field, negative particles bend toward the axis

- Electron beam : $E_e = 11$ GeV.
- Standard single electron trigger.

VII. SIMULATIONS

A. ρ^0 channel

1. Kinematics

We plan to measure the $ep \rightarrow ep\rho^0 \leftrightarrow \pi^+\pi^-$ reaction by detecting the scattered electron and at least two of the three charged hadrons of the final state, i.e. two particles among the recoil proton, the π^+ and the π^- . As we will see shortly, depending on the phase space which is probed, it is more advantageous to detect either the recoil proton and the π^+ or the π^+ and the π^- .

Fig. 8 shows the missing mass resolution of the two “topologies” $ep \rightarrow ep\pi^+X$ and $ep \rightarrow e\pi^+\pi^-X$ as determined by the FASTMC code, which is the software developed by the CLAS12 collaboration to estimate resolution and acceptances for the future CLAS12 detector.

In this figure, we also show the distributions of $MM_{ep \rightarrow ep\pi^+X}^2$ and of $MM_{ep \rightarrow e\pi^+\pi^-X}^2$ for the exclusive 3-pion electroproduction process $ep \rightarrow e\pi^+\pi^-\pi^0$, which gives continuums instead of peaks. It is seen that we clearly obtain good enough resolutions for the squared missing mass of the pion and for the squared missing mass of the proton to identify the exclusive ρ^0 electroproduction reaction from the 3-pion process. In these figures, the normalization has been taken equal for the two processes $ep \rightarrow ep\rho^0 \leftrightarrow \pi^+\pi^-$ and $ep \rightarrow e\pi^+\pi^-\pi^0$ over the same $(x_B, Q^2, -t)$ phase space. The assumption behind this is that the cross sections of these two processes are equal on this same phase space, which is a very conservative hypothesis.

Fig. 9 shows the kinematical planes (Q^2, x_B) , (Q^2, W) and (Q^2, t) which can be accessed with an 11 GeV electron beam. The distributions have been generated according to realistic cross sections. For this, we have used the event generator GENEV. This event generator, built by the Genova group participating to CLAS12, uses tables which contain the existing experimental data for the exclusive photoproduction of the ρ^0 meson. It then extrapolates to electroproduction by multiplying by the standard virtual photon flux factor Γ_V and by

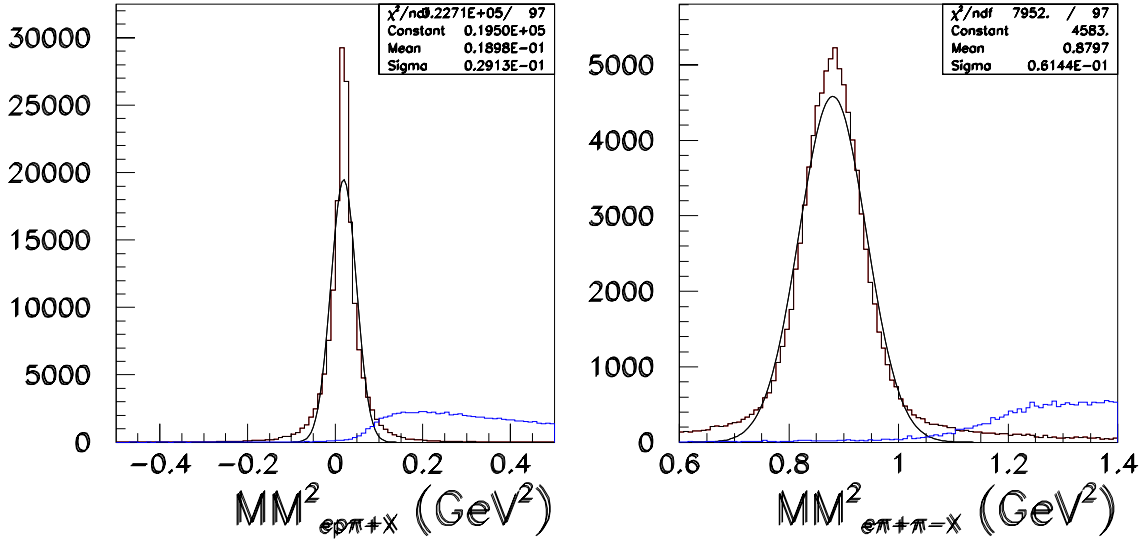


FIG. 8: Left : missing mass $MM^2_{ep\pi^+\pi^-X}$ in GeV^2 . Right : missing mass $MM^2_{e\pi^+\pi^-X}$ in GeV^2 . The black histograms are the event distributions for the $ep \rightarrow ep\rho^0 \leftrightarrow \pi^+\pi^-$ process, the black curves are the Gaussian fits to these peaks and the blue histograms are the event distributions for the $ep \rightarrow e\pi^+\pi^-\pi^0$ process.

form factors which are adjusted to the few existing electroproduction data. We will see further down the relatively good agreement of this event generator with the few ρ^0 electroproduction data which have been measured in part of the phase space covered by this proposal. In Fig. 9, the black areas show the theoretical phase spaces which are in principle accessible. The superposed red areas show these same phase spaces when the simultaneously detection of an electron, a proton and a π^+ is requested in CLAS12 (using the FASTMC code).

It is seen in Fig. 9 that events are lost at large Q^2 . The left plot of Fig. 11, which presents the polar angle of the scattered electron θ_e vs Q^2 , shows that large Q^2 values correspond to large θ_e and that these events are lost due to the lack of electron detection in CLAS12 over $\theta_e = 40^\circ$. Indeed, the CLAS12 EC calorimeters extend from $\theta \approx 5^\circ$ to $\approx 40^\circ$.

Fig. 9 also shows that in the “topology” electron, proton and π^+ detected, we miss large $-t$ events. The center panel of Fig. 11 shows that very large $-t$ events correspond to very low polar angles of the recoil proton, i.e. $\theta_p < 5^\circ$ (very forward protons). CLAS12 is lacking charged particles tracking in this very forward region. The right panel of Fig. 11 shows that large $-t$ events correspond in contrast to a wide range of polar angles of the π^- and that

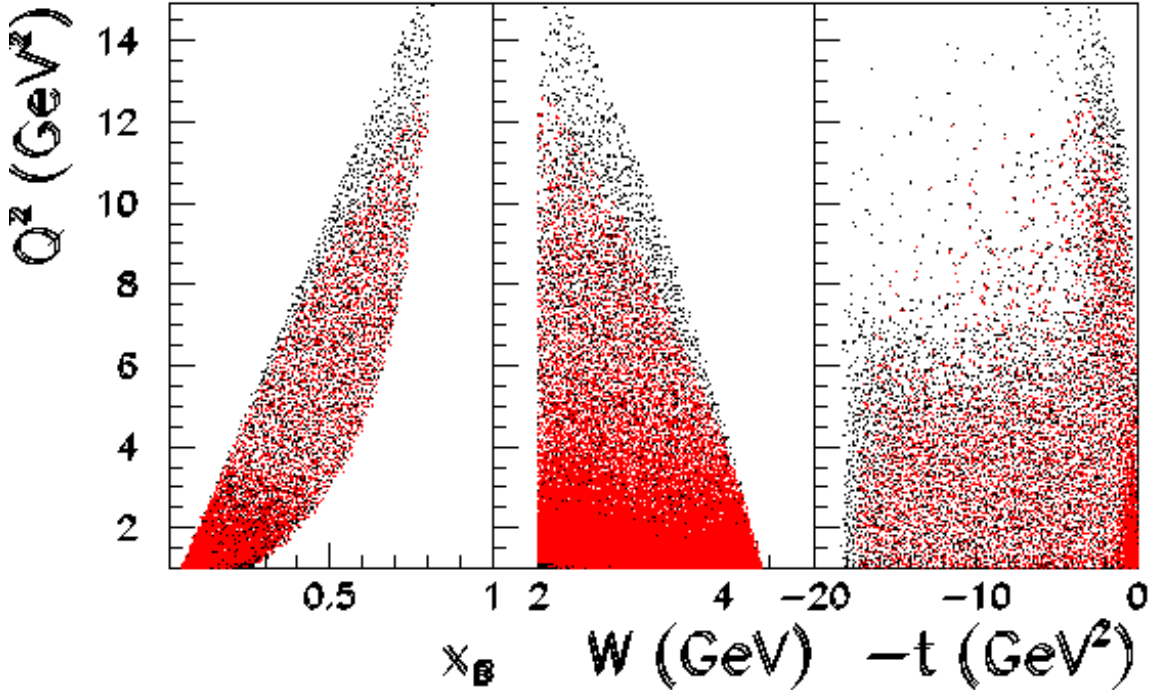


FIG. 9: Kinematic planes Q^2 vs x_B , W and t for the $ep \rightarrow ep\rho^0 \leftrightarrow \pi^+\pi^-$ reaction. Black points: without any requirement on the detection of the particles. Red points: with the requirement of the detection of an electron, a proton and a π^+ in CLAS12 (using the CLAS12 FASTMC code).

therefore, in order to access this kinematical region, it is more advantageous to detect the π^- instead of the proton (in addition to the electron and the π^+). We notice in Fig. 11 the “discontinuity” in the detected hadrons (red points) around $\theta = 40^\circ$ which marks the separation between the forward and central parts of CLAS12.

Finally, Fig. 12 shows the (θ, E) phase spaces of the final state electron, proton and π^+ according to our event generator.

2. Count rates

The acceptance (ratio of accepted events to generated ones) of CLAS12 has been determined by again using the FASTMC code. We show in Fig. 13 the x_B , Q^2 and t distributions of the generated events (black lines) and those of the accepted events (red, blue and green lines). The red curve corresponds to the “topology”: electron, proton and π^+ detected in CLAS12. The blue curve corresponds to the “topology”: electron, π^+ and π^- detected in CLAS12. We remark again what we pointed out in the previous subsection, i.e. that the

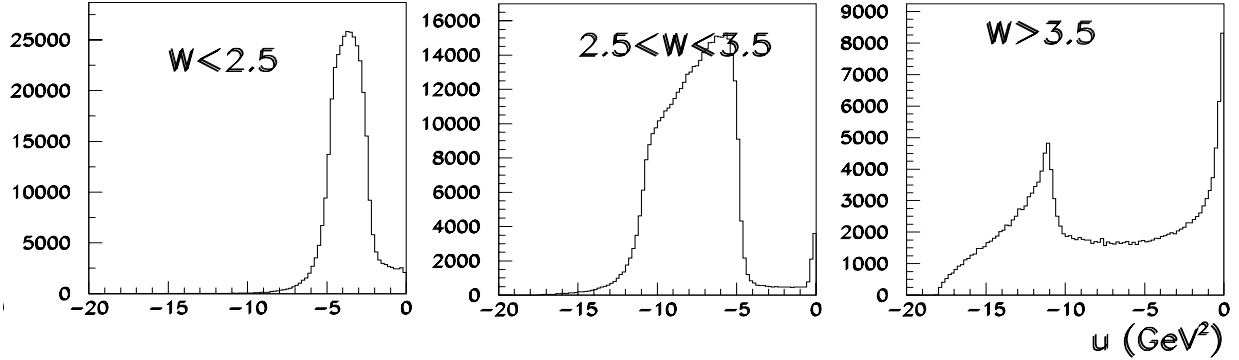


FIG. 10: The same events as in Fig. 9 plotted as a function of u , illustrating the predicted emergence [10] [23] of the u -channel process relative to the decrease in the overall ρ production with increasing W .

large $-t$ region is better accessed in the “topology”: electron, π^+ and π^- detected. By making the ratio of these distributions, we see that the (integrated) acceptance values of CLAS12, determined by FASTMC, for the $ep \rightarrow ep\rho^0 \leftrightarrow \pi^+\pi^-$ reaction are in average of the order of 10%, of course depending on the kinematics. For sake of completeness, we also present (green curve) in Fig. 13 the “topology” : an electron, a proton, a π^+ and a π^- detected in CLAS12, i.e. all four particles of the final state detected in CLAS12. This corresponds of course to the lowest acceptance. The analysis of this “topology” can nevertheless be useful for double-checking purposes (normalization issues, background subtraction checks, etc...).

In order to estimate the expected count rates, we have used the event generator GENEV which reproduces relatively correctly the existing data, for the normalization as well as for the various kinematical dependences. The total cross section for the $ep \rightarrow ep\rho^0 \leftrightarrow \pi^+\pi^-$ process is thus estimated, integrated over all the phase space of concern, i.e. $E_e=11$ GeV, $Q^2 > 1$ GeV², $W > 2$ GeV, to:

$$\sigma_{tot} \approx 10^{-3} \mu b \quad (3)$$

With a luminosity of $10^{35} \text{cm}^{-2} \text{s}^{-1}$ and 1000 hours of beam time, this leads to about 1 billion “theoretical” ρ^0 events, among which only about 10% will be detected in CLAS, as seen previously.

As a start, we propose to take bins of width of 0.5 GeV² for Q^2 (meaning 22 bins from 1

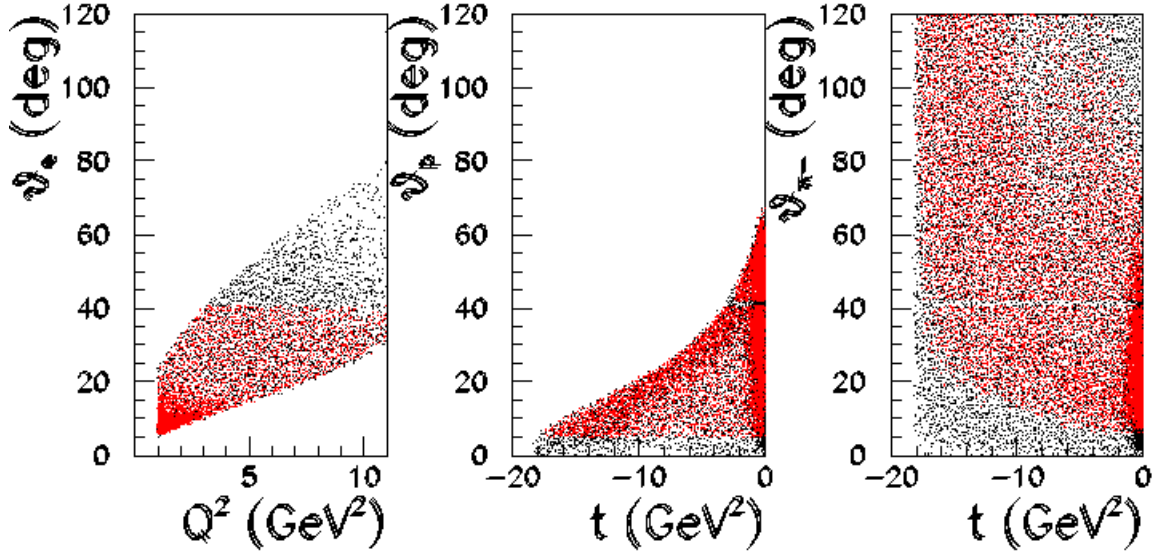


FIG. 11: Left panel: θ_e vs Q^2 . Center panel: θ_p vs t . Right panel: θ_{π^-} vs t . Black points: without any requirement on the detection of the particles. Red points: with the requirement of the detection of an electron, a proton and a π^+ in CLAS12 for the left and center panels and with the requirement of the detection of an electron, a π^+ and a π^- for the right panel (using the CLAS12 FASTMC code).

to 13 GeV^2), of width of 0.05 for x_B (meaning 15 bins from 0.05 to 0.8) and of width of 0.5 GeV^2 for t (meaning 40 bins from 0 to 20 GeV^2). This binning leads to a “pavement” of the (x_B, Q^2, t) phase space such as the one of Fig. 14. In each (x_B, Q^2) cell, the reconstructed $\frac{d\sigma}{dt}$ with its expected (statistical) error bar is shown (black points) as a function of $-t$. It is clear that details are barely distinguishable in this figure. It is just meant to give an overall view of the phase space covered and of some general features. Before “zooming” in some sections of the figure so as to see details, let’s make a couple of general remarks. For instance, the red points show the measurement of $\frac{d\sigma}{dt}$ for the $ep \rightarrow epp^0$ reaction at CLAS with the 5.75 GeV beam [36]. The important gain in the (x_B, Q^2, t) phase space coverage with the 11 GeV beam is evident. We can also notice the evolution of t_{max} (blue vertical line in every panel) which, at fixed x_B increases as Q^2 increases.

Let us now focus on a few particular zones of Fig. 14. Fig. 15 is a zoom on the green cell of Fig. 14 which corresponds to $0.25 < x_B < 0.45$ and $1.5 < Q^2 < 3.5 \text{ GeV}^2$ and where most of the 5.75 GeV measurements carried out with CLAS6 lie. Fig. 15 shows only the $-t$ region up to 3 GeV^2 . We notice that our event generator reproduces and models very

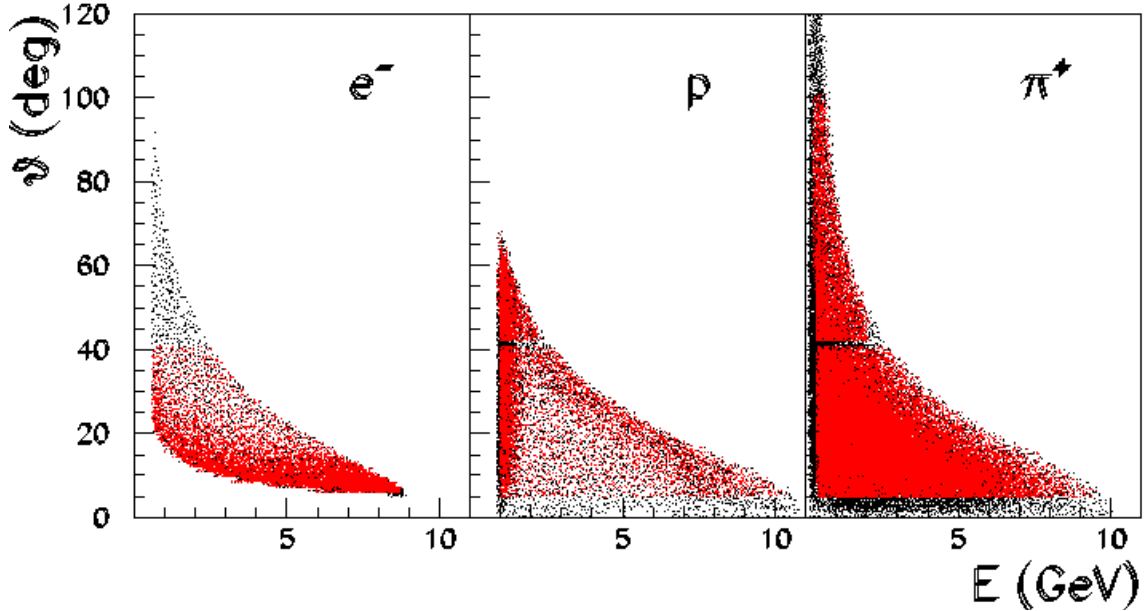


FIG. 12: Polar angle θ vs energy E for the electron (left panel), the proton (center panel) and the π^+ (right panel) in the $ep \rightarrow ep\rho^0 \leftrightarrow \pi^+\pi^-$ reaction according to our event generator. Black points: without any requirement on the detection of the particles. Red points: with the requirement of the detection of an electron, a proton and a π^+ in CLAS12.

correctly the measured cross sections (t -dependence and overall normalization) since the (measured) red points overlay almost everywhere the (simulated) black points (our model tends to underestimate a bit the data at large x_B though). We also notice that the 5.75 GeV measurements cover only the small t region, up to 2.5 GeV^2 (however, t_{max} is very close to 3 GeV^2 in this restricted kinematical region, see Fig. 14).

We recall that the black points are issued from our simulations and represent the cross sections that we expect to measure. Their (statistical) error bars are almost invisible in Fig. 15. One has to realize that, for instance, for the first t bin (i.e. starting at t_{min}) of the lower left (x_B, Q^2) bin of this figure (i.e. $0.25 < x_B < 0.30$ and $1.5 < Q^2 < 2 \text{ GeV}^2$), one has, according to our simulations, about 5 million events accepted. As Q^2 and $-t$ increase, these rates drop in general but they are still of the order of several hundred thousands for instance at $-t=2 \text{ GeV}^2$ in the upper right bin of Fig. 15 (i.e. $0.40 < x_B < 0.45$ and $3 < Q^2 < 3.5 \text{ GeV}^2$). As we will discuss further, our main source of uncertainty is actually expected to be of a systematic nature, in particular stemming from the subtraction of the non-resonant 2-pion continuum under the ρ^0 peak (see subsection VII A 3).

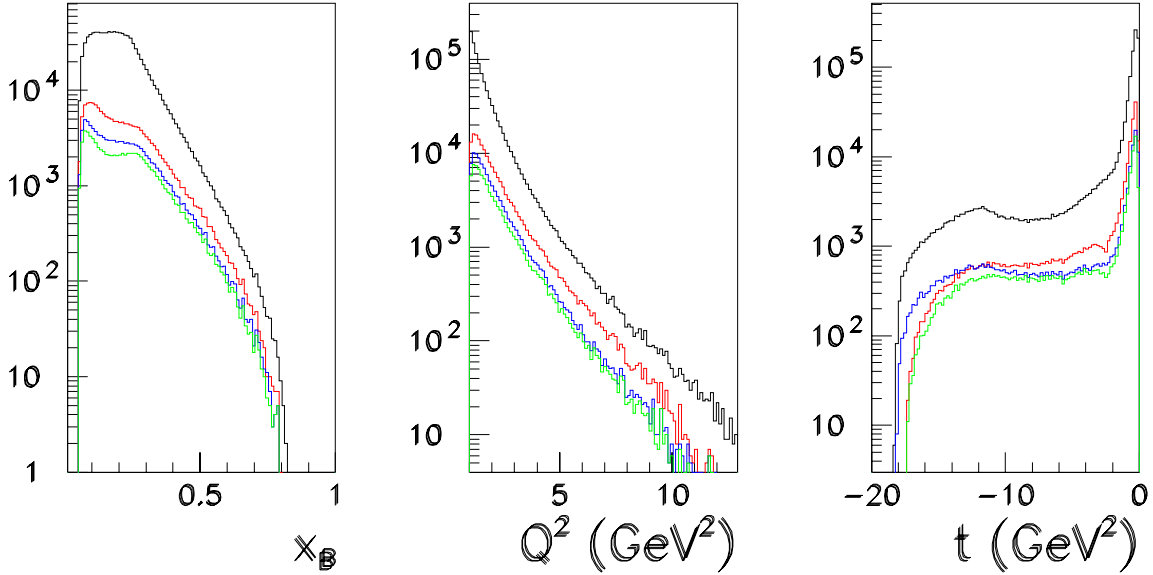


FIG. 13: Distributions of the generated events (black curves) and of the accepted events (red; blue and green curves) in CLAS12, as determined by FASTMC, as a function of x_B , Q^2 and t . The red curve corresponds to the “topology” : an electron, a proton and a π^+ detected in CLAS12, the blue curve corresponds to the “topology” : an electron, a π^+ and a π^- detected in CLAS12 and the green curve corresponds to the “topology” : an electron, a proton, a π^+ and a π^- detected in CLAS12.

Fig. 16 is now a zoom of Fig. 14 corresponding to the red cell on this latter figure covering the region $0.05 < x_B < 0.25$ and $1 < Q^2 < 4 \text{ GeV}^2$. It shows that we aim in the present proposal at measuring the whole t domain, up to t_{max} . As outlined in the physics motivation, there might be some interesting process related to TDAs at backward (ρ^0) angles, i.e. large $|t|$ or small $|u|$. In absence of any experimental information in this region, we have introduced in our event generator such a backward process under the form of an exponential e^u form with an arbitrary normalization approximatively equal to $1/50$ the forward peak. It should be clear that there is evidently no guarantee that such peak really exists and if it does that it has such normalization and such u -, Q^2 -, x_B -dependences, etc... Fig. 16 simply illustrates with which accuracy we can measure this peak under the (arbitrary) conditions aforementioned. One can also notice that this backward peak is much less pronounced than the forward one. It is due to the finite size of the (x_B, Q^2) bins and to the fact that t_{max} evolves rapidly with x_B and Q^2 , thus smearing and diluting this backward peak.

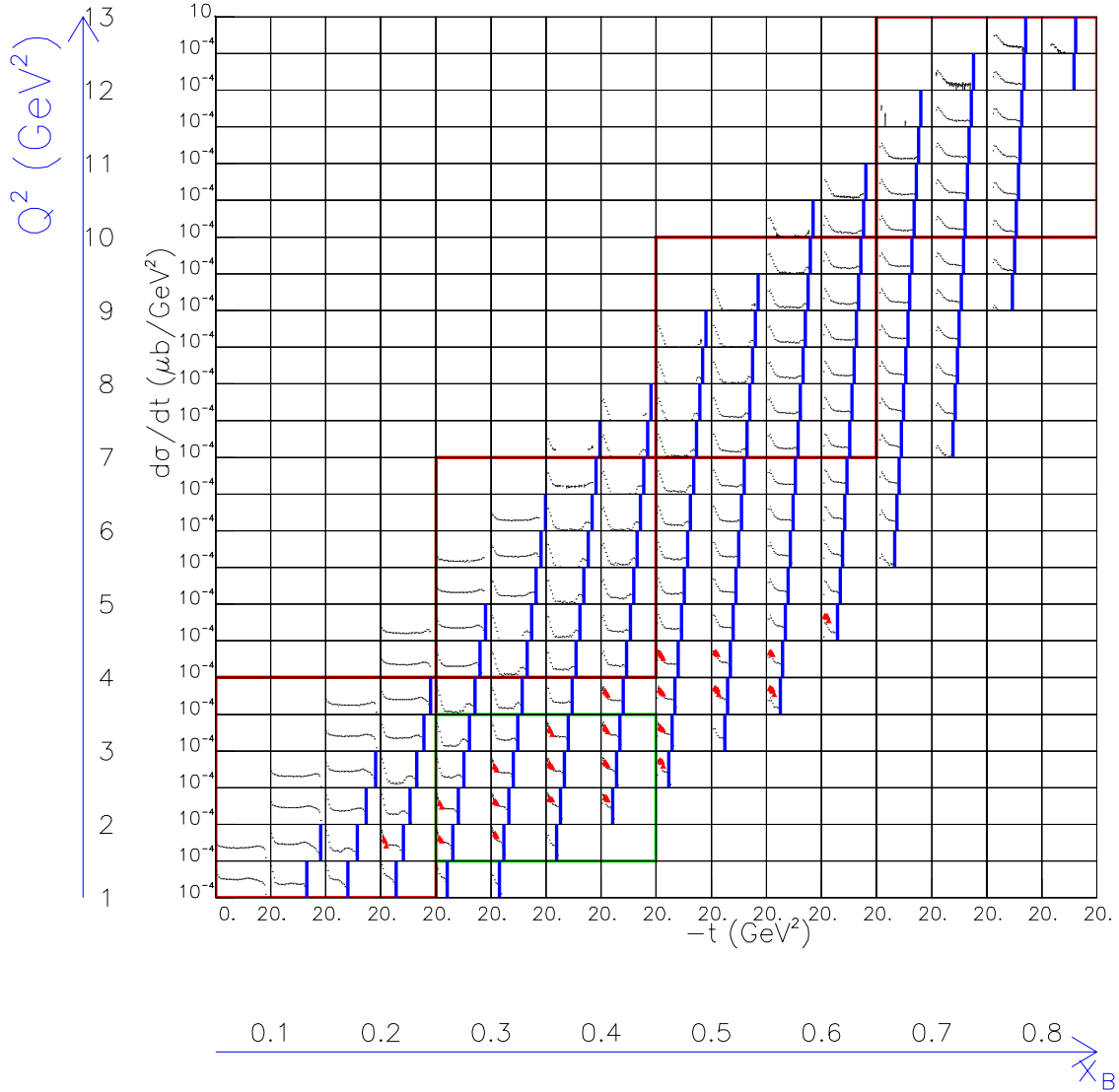


FIG. 14: $\frac{d\sigma}{dt}$ for the reaction $ep \rightarrow epp^0$ as a function of $-t$ (ranging from 0 to 20 GeV^2) for each (x_B, Q^2, t) bin accessible with a 11 GeV beam and the CLAS12 detector (with $Q^2 > 1 \text{ GeV}^2$ and $W > 2 \text{ GeV}$). The black points correspond to the simulations (1000 hours of beam time at a luminosity of $10^{35} \text{ cm}^{-2} \text{ s}^{-1}$) and the red points to the 5.75 GeV measurement [36]. The vertical blue line shows t_{max} for every (Q^2, x_B) cell.

Once again, the statistical error bars on this figure are barely visible. Due to the relatively important high cross section of the $\gamma^* p \rightarrow p\rho^0$ process, the high luminosity in CLAS12, the 1000 hours of beam time, the relatively good acceptance of CLAS12, we have estimated, for instance, for the upper right (x_B, Q^2) of Fig. 16 (i.e. $0.20 < x_B < 0.25$ and $3.5 < Q^2 < 4 \text{ GeV}^2$), count rates as high as $\approx 100,000$ at the smallest $|t|$ bin. At larger $|t|$, count

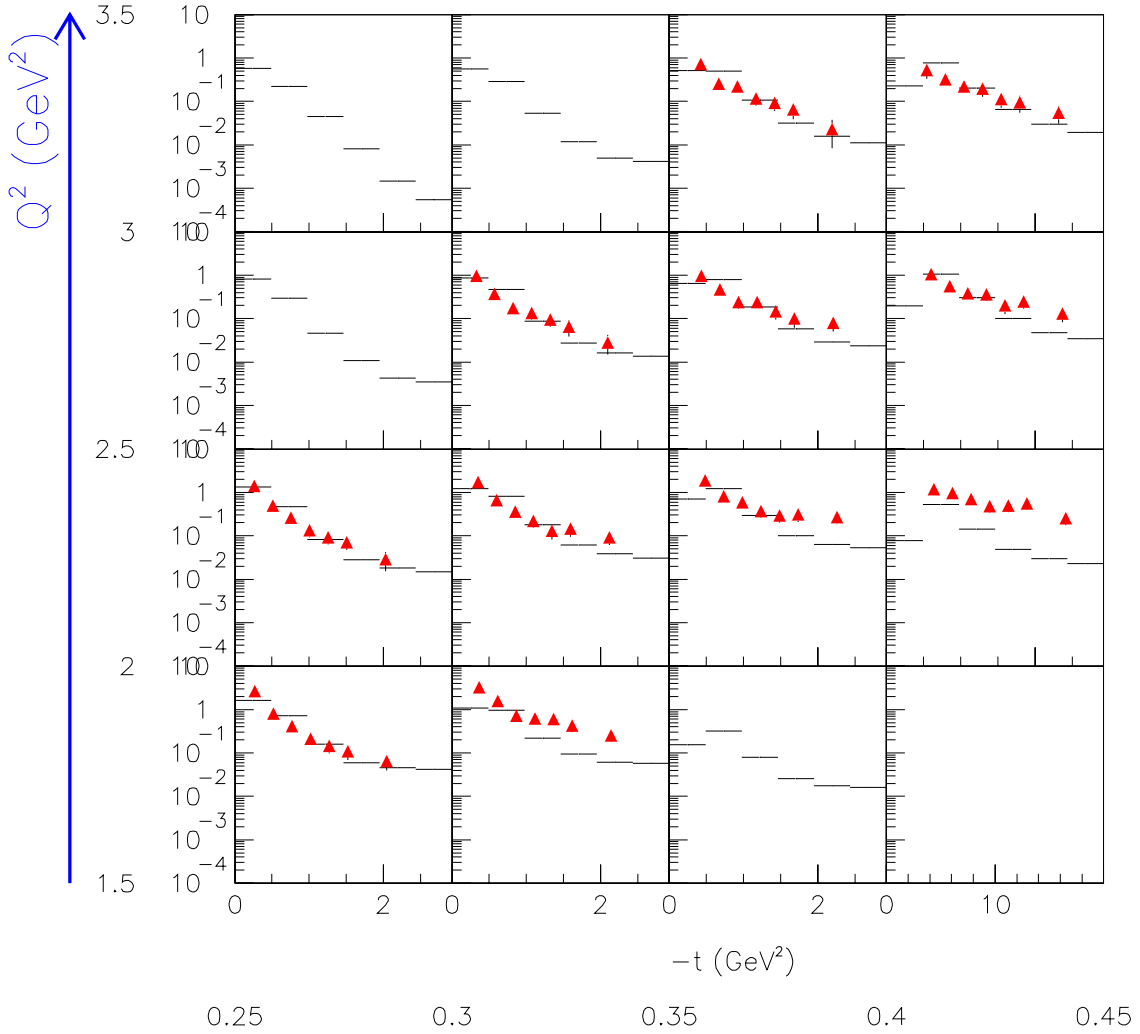


FIG. 15: $\frac{d\sigma}{dt}$ for the reaction $ep \rightarrow ep\rho^0$ as a function of $-t$ (ranging from 0 to 3 GeV^2) in the specific region $0.25 < x_B < 0.45$ and $1.5 < Q^2 < 3.5 \text{ GeV}^2$. Same definition of the black and red points as in Fig. 14. The error bars of the black points are purely statistical.

rates will of course drop, essentially proportionally to the cross section. We recall that the cross section of the $\gamma^*p \rightarrow p\rho^0$ process is currently unknown in such kinematical region and that we only make a guess in Fig. 16 with the particular event generator that we are using (extrapolation from GENEV).

Figs. 17, 18 and 19 finally show the zooms on the three other (x_B, Q^2) zones of Fig. 14 (red boxes), i.e. respectively $0.25 < x_B < 0.45$ and $4 < Q^2 < 7 \text{ GeV}^2$, $0.45 < x_B < 0.65$ and $7 < Q^2 < 10 \text{ GeV}^2$, and $0.65 < x_B < 0.85$ and $10 < Q^2 < 13 \text{ GeV}^2$. These figures show that we are able to measure with the CLAS12 detector and the CEBAF 11 GeV electron beam, very

precisely, in terms of statistics, the (reduced) differential cross sections $\frac{d\sigma}{dt}$ of the $ep \rightarrow ep\rho^0$ reaction up to $Q^2 \approx 13 \text{ GeV}^2$ in the valence region. According to the particular event generator (extrapolation from GENEV) that we have used, we still expect, for instance for the upper right (x_B, Q^2) of Fig. 19 (i.e. $0.80 < x_B < 0.85$ and $12.5 < Q^2 < 13 \text{ GeV}^2$), count rates of the order of ≈ 100 at the smallest $|t|$ bins. These count rates obviously depend on the behavior at large Q^2 of the $\gamma^*p \rightarrow p\rho^0$ cross section. If it turns out to be falling with Q^2 faster (slower) than in our particular event generator, these count rates will of course be lower (higher).

It is clear from these figures that we should be able to very accurately (at least, statistically) extract the observables that we outlined in the introduction, i.e. the Q^2 dependence of $\frac{d\sigma}{dt}$ at fixed x_B and $-t$ (in order to check the scaling behavior), the t - (at forward angles) and u - (at backward angles) slopes as a function of Q^2 and x_B , the s -dependence of $\frac{d\sigma}{dt}$ at $\cos(\theta)_{cm}=90^\circ$, etc...

Of course, systematic errors have to be added to these statistical errors. These systematic errors are actually expected to be the main source of uncertainty. As mentioned earlier, the most important source is anticipated to be stemming from the subtraction of the important non-resonant 2-pion continuum lying under the ρ^0 peak. We discuss this issue in the following subsection.

3. Subtraction of the non-resonant 2-pion background under the ρ^0 peak

Fig. 20 shows some typical $\pi^+\pi^-$ invariant mass spectra that we obtained at CLAS with the 6 GeV beam [36]. The ρ^0 peak (as well as the $f_0(980)$ and $f_2(1270)$ peaks in some bins) is clearly visible but sits on top of a $\pi^+\pi^-$ continuum background. This (physical) background has several origins, the main sources being the exclusive electroproduction of a pion and a nucleon resonance, the latter decaying into a pion and a nucleon (such as $ep \rightarrow e\pi^-\Delta^{++} \hookrightarrow p\pi^+$) or simply incoherent exclusive 2-pion production $ep \rightarrow ep\pi^+\pi^-$. In Ref. [36], in absence of any realistic model describing simultaneously the $\pi^+\pi^-$, $p\pi^+$ and $p\pi^-$ invariant mass spectra in the energy regime which concerns us, we modeled the $\pi^+\pi^-$ continuum under the ρ^0 peak by an incoherent sum of a phase space distribution for the 3-body $\gamma^*p \rightarrow p\pi^+\pi^-$ process and of two Breit-Wigners for the $f_0(980)$ and $f_2(1270)$. In Ref. [36], we associated with this background subtraction procedure a systematic error bar

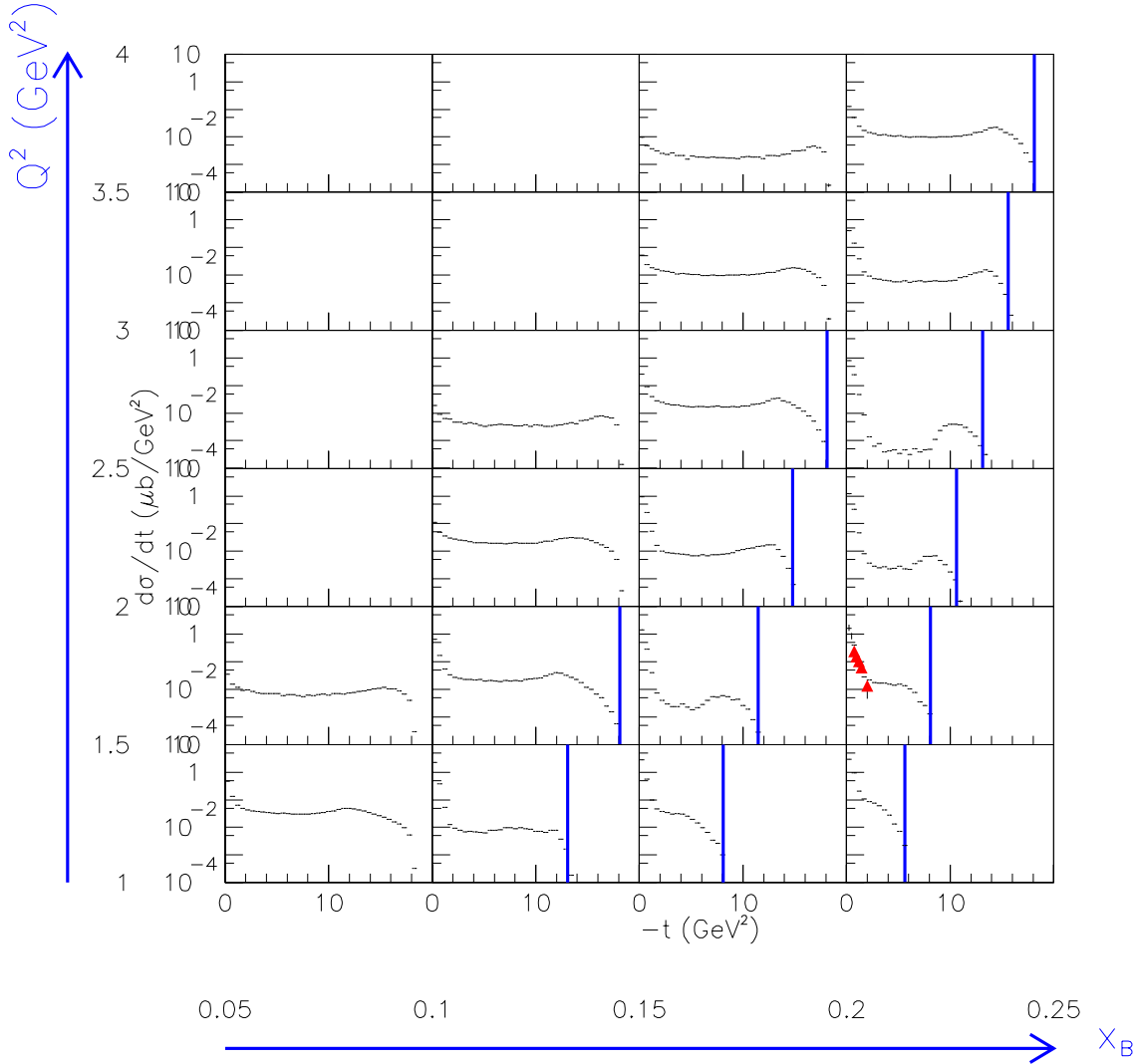


FIG. 16: $\frac{d\sigma}{dt}$ for the reaction $ep \rightarrow ep\rho^0$ as a function of $-t$ (ranging from 0 to 20 GeV^2) in the specific region $0.05 < x_B < 0.25$ and $1 < Q^2 < 4 \text{ GeV}^2$. Same definition of the black and red points and of the vertical blue lines as in Fig. 14. The error bars of the black points are purely statistical.

of the order of 20%, which became then the most important source of uncertainty in our final cross sections.

With the 11 GeV beam, the situation is expected to be more favorable in terms of ratio signal to background, i.e. ρ^0 to incoherent $\pi^+\pi^-$ pairs. Indeed, most of the sources contributing to the $\pi^+\pi^-$ continuum under the ρ^0 peak are expected to fall with energy faster than the ρ^0 signal. Fig. 21 shows for instance the $\pi^+\pi^-$ invariant mass spectra obtained at HERMES ($E_e=27 \text{ GeV}$) and Fig. 22 the one obtained at Cornell ($E_e=11 \text{ GeV}$). Although we will unavoidably have to assign a systematic error to the subtraction of the

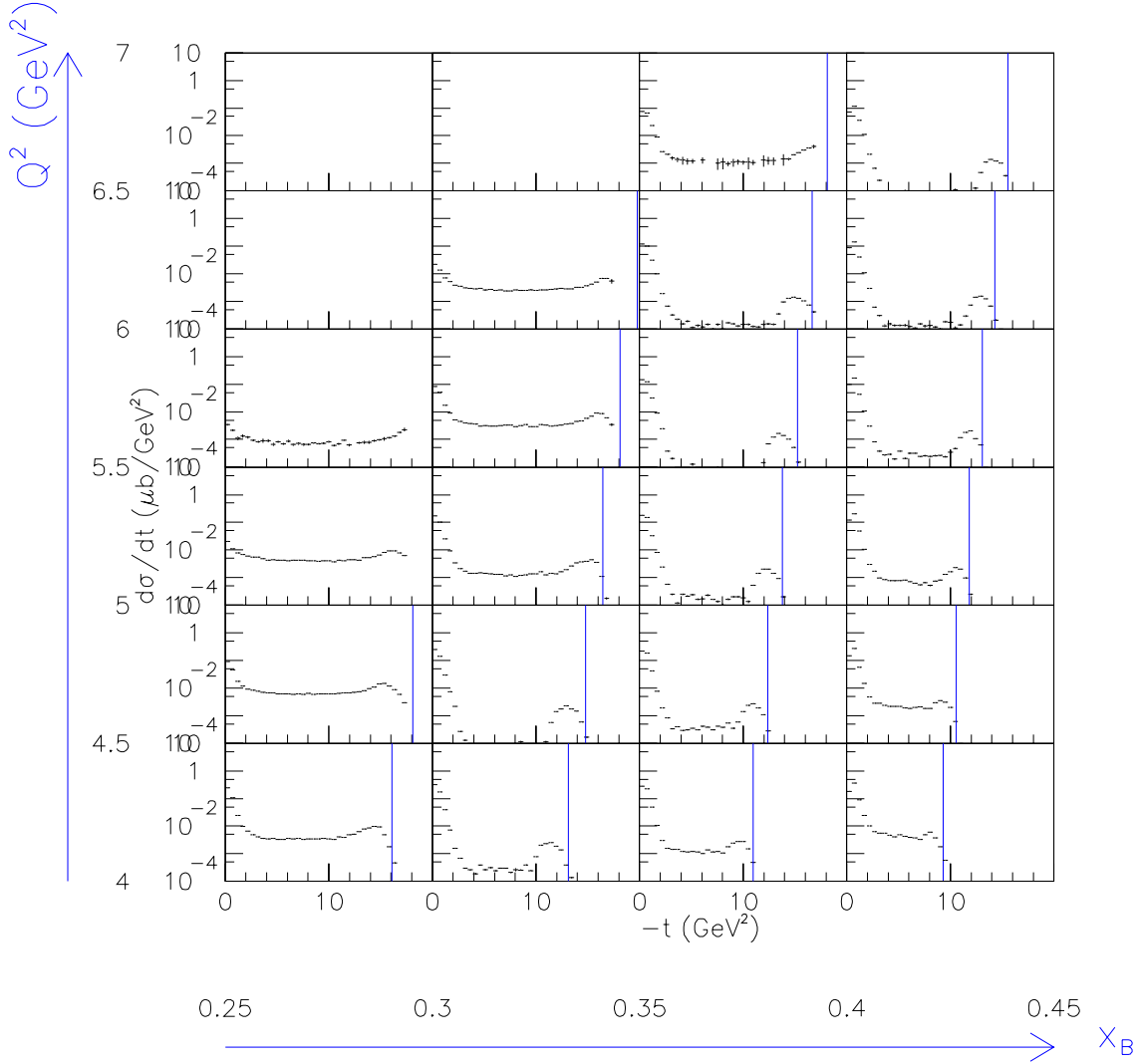


FIG. 17: $\frac{d\sigma}{dt}$ for the reaction $ep \rightarrow epp^0$ as a function of $-t$ (ranging from 0 to 20 GeV^2) in the specific region $0.25 < x_B < 0.45$ and $4 < Q^2 < 7 \text{ GeV}^2$. Same definition of the black and red points and of the vertical blue lines as in Fig. 14.

$\pi^+ \pi^-$ continuum, it can be anticipated that it will be much smaller than the 20% that we estimated in Ref. [36], due to the lower magnitude of this continuum. Besides, we can expect that, in the next 4 to 5 years, significant theoretical progress will have been accomplished for a realistic description of the $ep \rightarrow ep\pi^+\pi^-$ reaction, ideally including all the processes contributing to it at the amplitude level, thus further minimizing the systematic uncertainty associated to this subtraction. An educated and rather conservative guess could be that we will obtain less than 10% systematic uncertainty due to this background subtraction

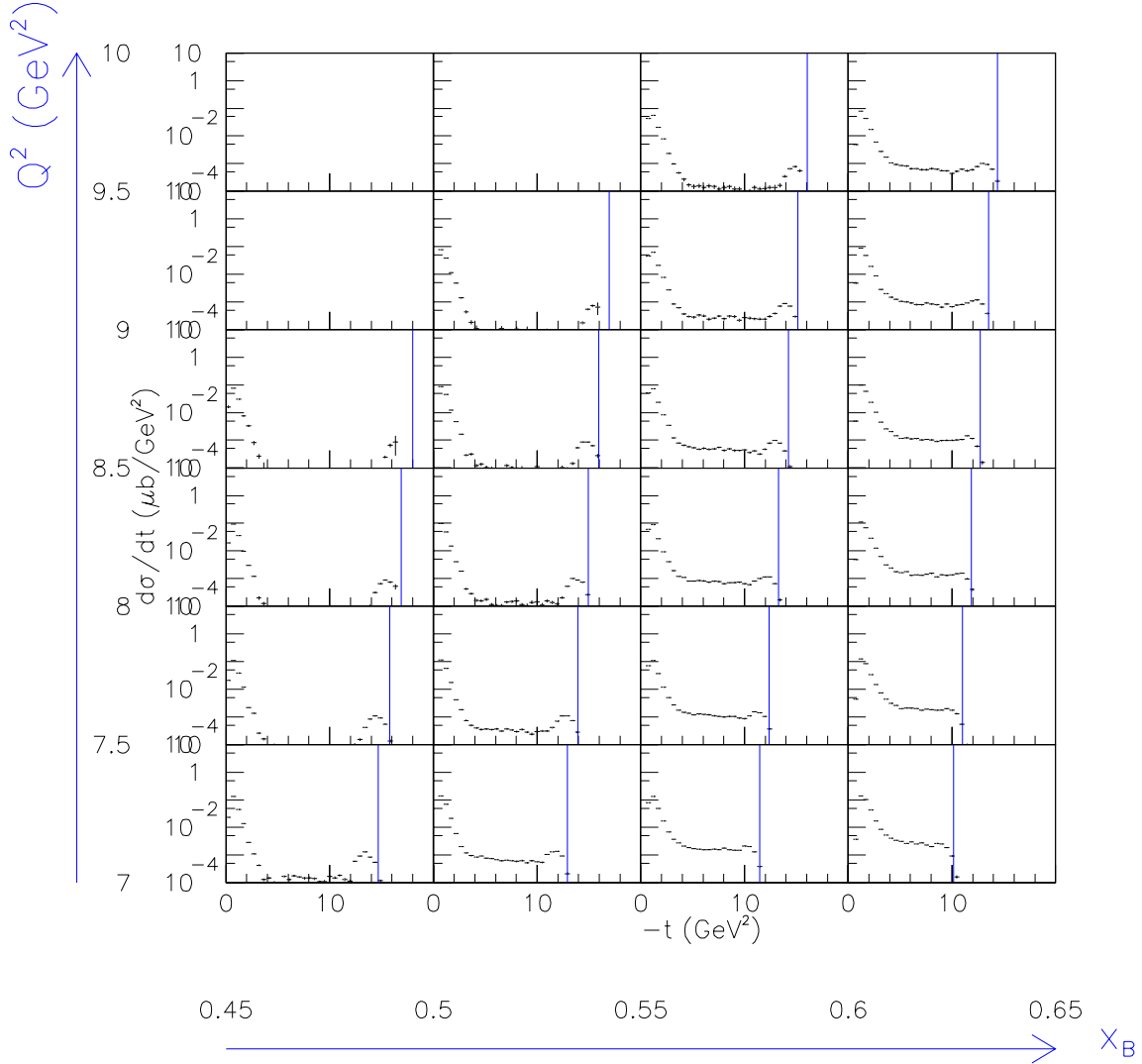


FIG. 18: $\frac{d\sigma}{dt}$ for the reaction $ep \rightarrow ep\rho^0$ as a function of $-t$ (ranging from 0 to 20 GeV^2) in the specific region $0.45 < x_B < 0.65$ and $7 < Q^2 < 10 \text{ GeV}^2$. Same definition of the black points and of the vertical blue lines as in Fig. 14.

procedure.

4. Longitudinal/transverse separation

Vector mesons have this particular advantage that there is a straightforward access to their polarization state via the analysis of their (pion) decay angular distributions. Also, because they carry the same quantum numbers as the initial state virtual photon, there is the dominant feature in their production mechanism which consists in the conservation

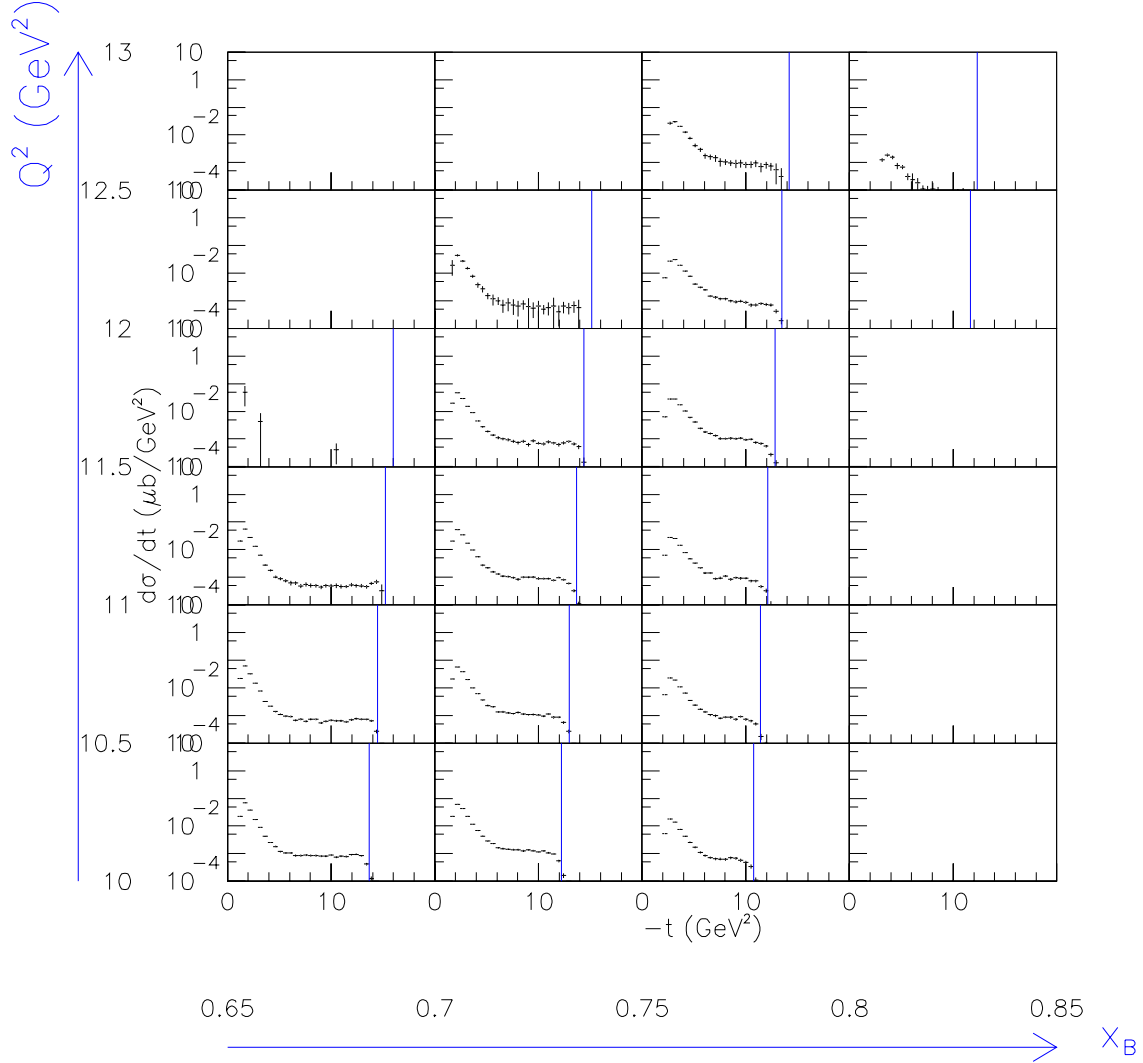


FIG. 19: $\frac{d\sigma}{dt}$ for the reaction $ep \rightarrow ep\rho^0$ as a function of $-t$ (ranging from 0 to 20 GeV^2) in the specific region $0.65 < x_B < 0.85$ and $10 < Q^2 < 13 \text{ GeV}^2$. Same definition of the black points and of the vertical blue lines as in Fig. 14.

of helicity between the initial state virtual photon and the final state vector meson. This feature is called “s-channel helicity conservation” (SCHC) and it has been experimentally verified to a level close to 80% in most exclusive vector meson electroproduction channels over a wide kinematical range, from low to large W and Q^2 . The SCHC rule therefore allows one to experimentally separate the longitudinal and the transverse parts of the $\gamma^*p \rightarrow p\rho^0$ reaction, i.e. respectively σ_L and σ_T . As was outlined in the physics motivation part of this proposal, this separation is crucial since the factorisation theorem which allows to access

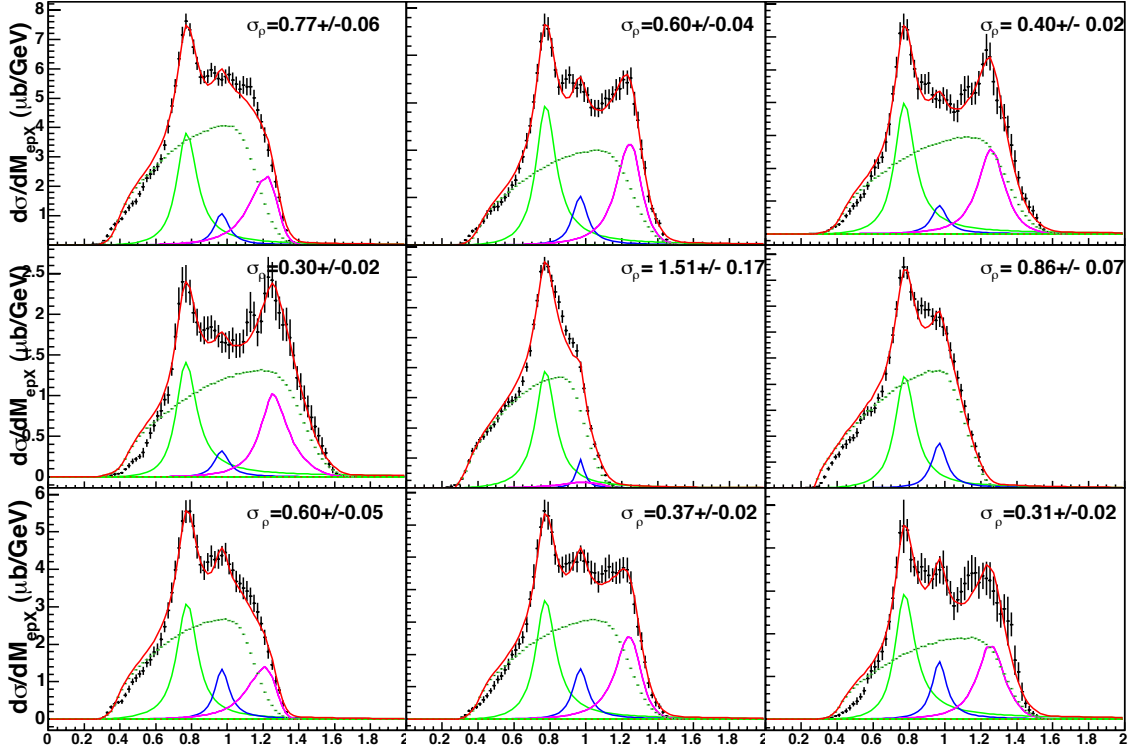


FIG. 20: $\pi^+\pi^-$ invariant mass spectra obtained at CLAS with the 5.75 GeV beam [36] for a few (x_B, Q^2) bins (from top left to bottom right : $(0.37, 2.35)$, $(0.37, 2.65)$, $(0.37, 2.95)$, $(0.37, 3.35)$, $(0.43, 2.35)$, $(0.43, 2.65)$, $(0.43, 2.95)$, $(0.43, 3.35)$ and $(0.43, 3.85)$). σ_ρ is expressed in μbarns . The x -axis is in GeV. The black points are the (acceptance-corrected and normalized) experimental data. These data were fitted by the (incoherent) sum of a (skewed) Breit-Wigner for the ρ^0 peak (light green curve), of a (skewed) Breit-Wigner for the $f_0(980)$ peak (blue curve), of a (skewed) Breit-Wigner for the $f_2(1270)$ peak (purple curve) and of the phase space distribution of the $\gamma^*p \rightarrow p\pi^+\pi^-$ process (dotted yellowish curve). The red curve is the sum of all these four contributions.

the non-perturbative quantities of interest (GPDs, TDAs,...) has been proven to hold only for the longitudinal part of the cross section.

We therefore plan to study the angular distribution of the decay pions of the ρ^0 . We define $\cos(\theta_{HS})$ as the polar angle of the π^+ in the so-called Helicity Frame where the ρ^0 is at rest and the z -axis is given by the ρ^0 direction in the $\gamma^* - p$ center-of-mass system. This variable and others are illustrated in Fig. 23. The $\cos(\theta_{cm})$ distribution is then expected to follow the general and model independent distribution [39]:

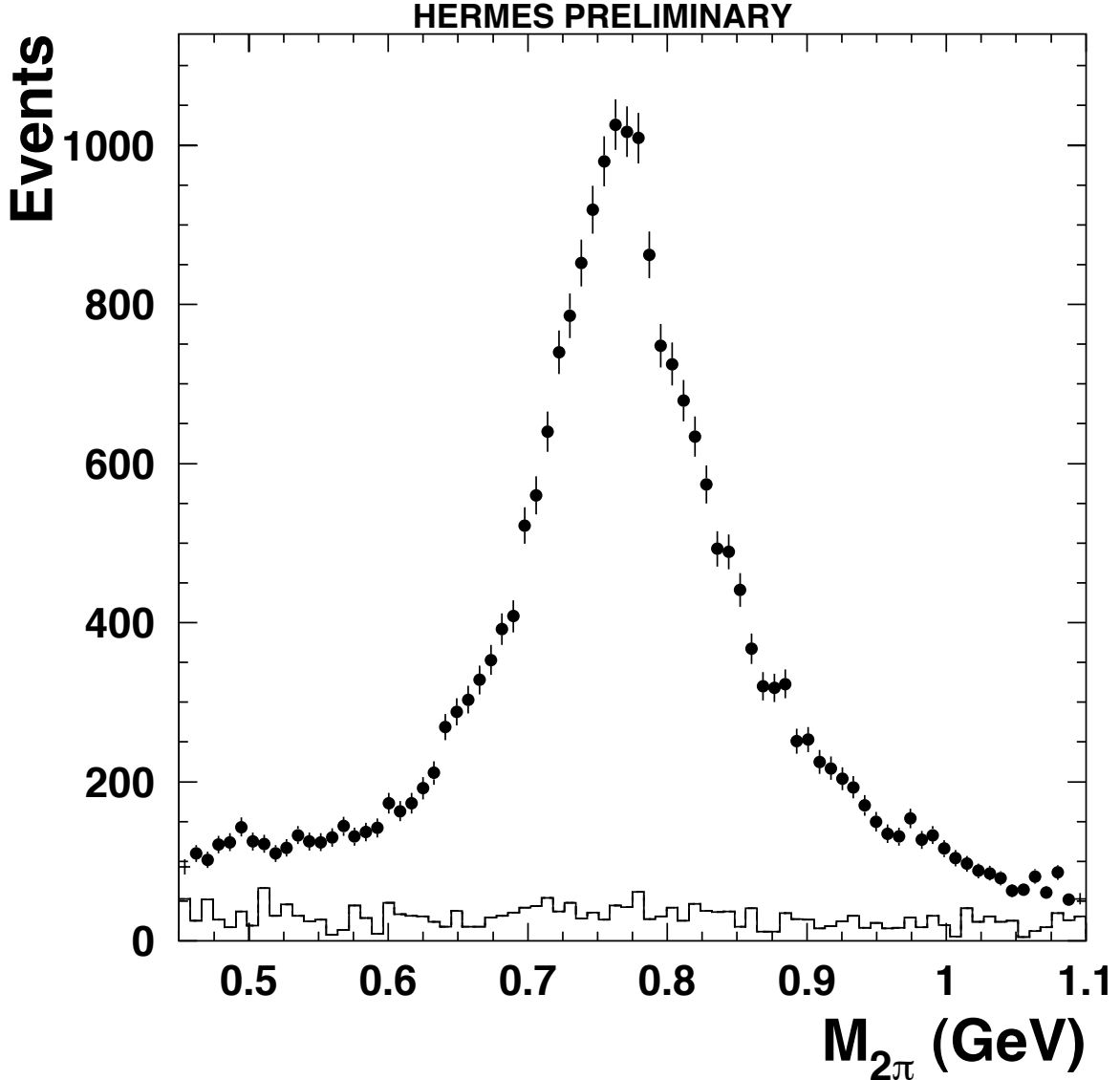


FIG. 21: An example of the 2-pion invariant mass distribution at the ρ^0 mass obtained at HERMES, overlaid with Monte Carlo estimated background contribution from DIS fragmentation. Figure taken from [37].

$$W(\cos \theta_{HS}) = \frac{3}{8} [(1 - r_{00}^{04}) + (3r_{00}^{04} - 1) \cos^2 \theta_{HS}]. \quad (4)$$

where r_{00}^{04} is a so-called “spin density matrix element” (SDME) which is a bilinear combination of the helicity amplitudes that describe the $\gamma^*p \rightarrow \rho^0 p$ transition. If SCHC applies, there is a direct relation between the measured r_{00}^{04} SDME and the ratio $R = \frac{\sigma_L}{\sigma_T}$:

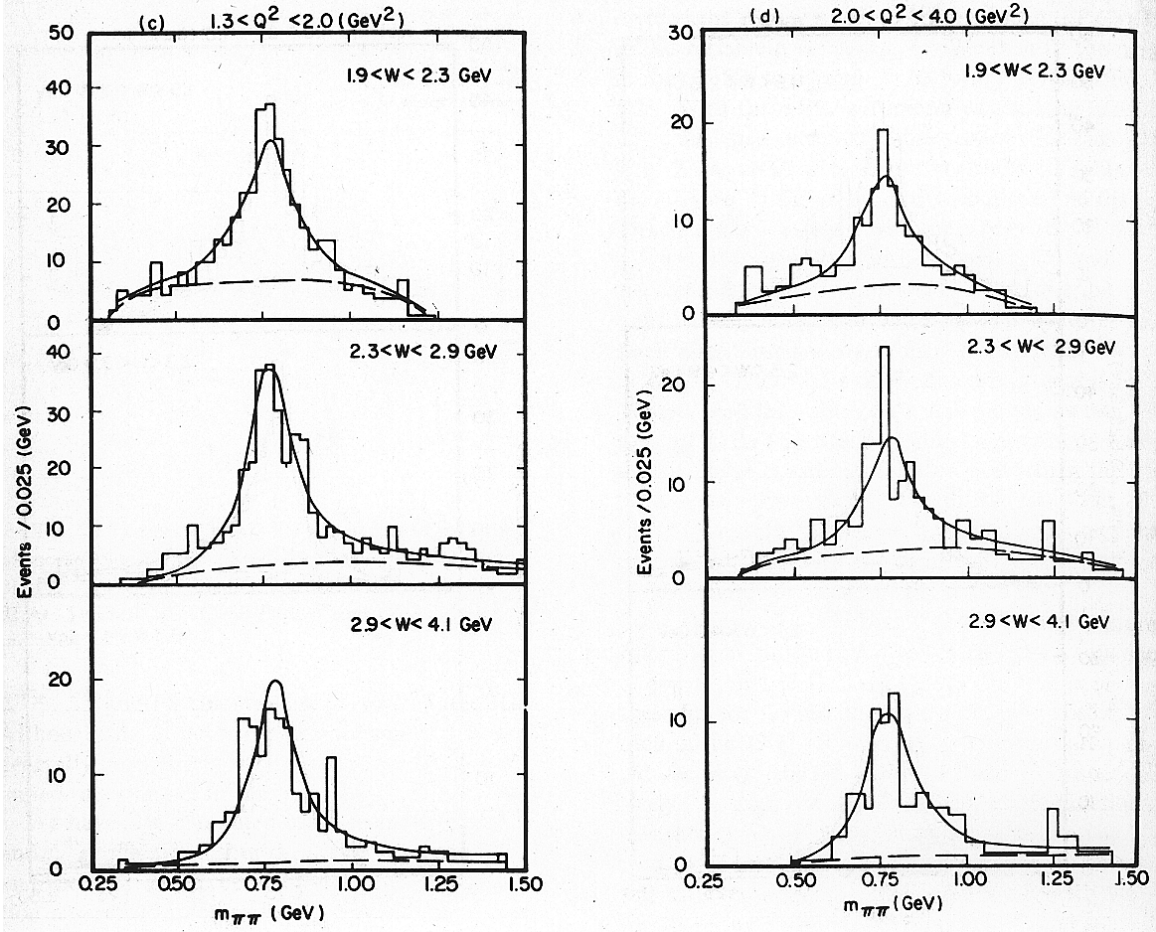


FIG. 22: $\pi^+\pi^-$ invariant mass distributions as measured in Cornell [38] in the Q^2 ranges 1.3 - 2.0 GeV^2 (left) and 2.0 - 4.0 GeV^2 (right) as function of the energy W . The solid curves are the fits to the total mass distribution whereas the dashed curves are the sum of the $e\rho\pi^-\Delta^{++}$, $e\pi^+\Delta^0$ and phase-space $e\rho\pi^+\pi^-$ contributions determined by the fits.

$$R = \frac{\sigma_L}{\sigma_T} = \frac{1}{\epsilon} \frac{r_{00}^{04}}{1 - r_{00}^{04}}. \quad (5)$$

We have simulated the ρ^0 decay angular distributions that we expect for the present experiment. Fig. 24 shows the simulated $\cos(\theta_{cm})$ distributions for the particular bin $(0.1; |x_B| 0.15, 1.5; Q^2; 2)$ for two t ranges ($0 < -t < 1$ -left plots- and $4 < -t < 8$ -right plots-). In these plots, the red histogram shows the number of accepted events (either an electron, a proton and a π^+ accepted or an electron, a π^+ and a π^- accepted) that we expect with the 11 GeV beam and the $10^{35} \text{cm}^{-2} \text{s}^{-1}$ luminosity. The vertical scale corresponds to this red histogram and shows that the number of events in each $\cos(\theta_{cm})$ bins is of the order of a

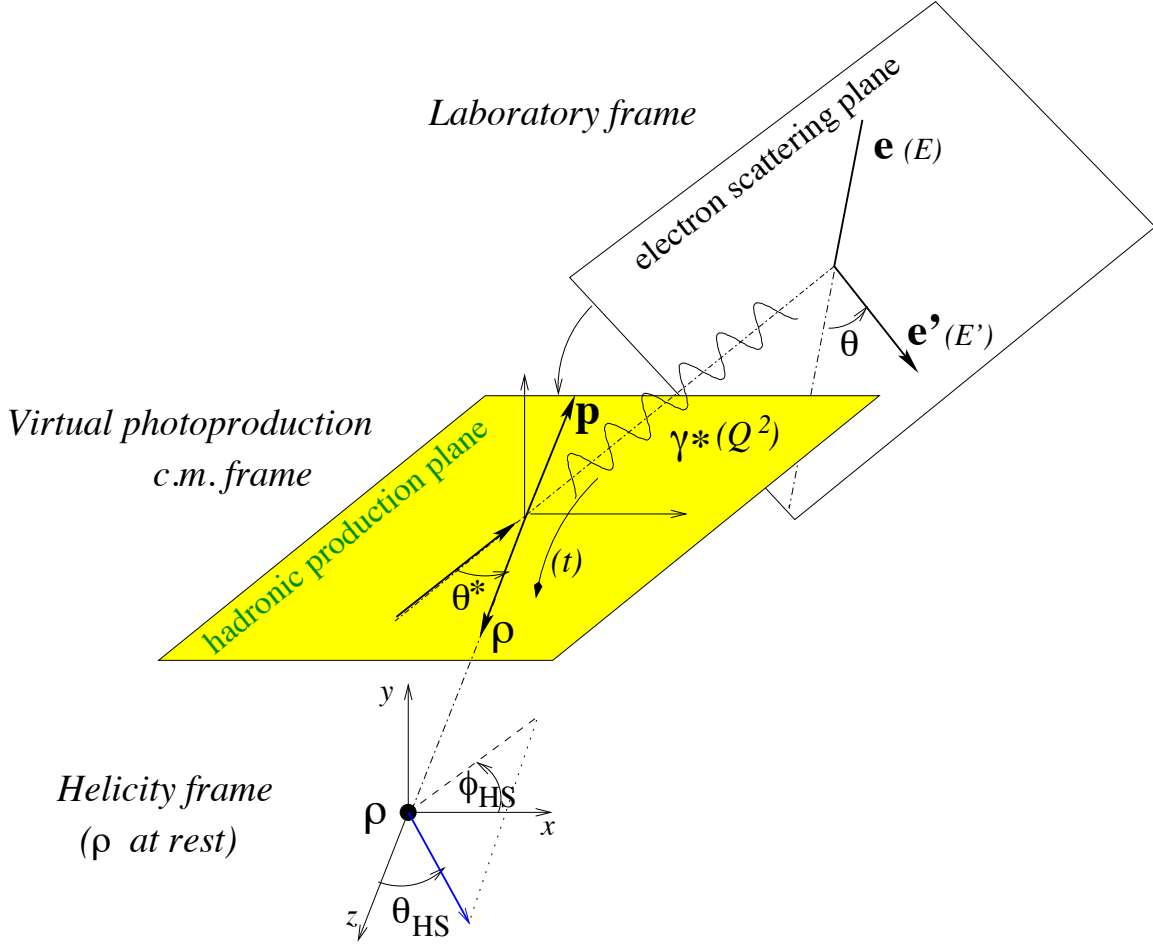


FIG. 23: Reference frames and relevant variables for the description of the $ep \rightarrow e'p\rho^0 \leftrightarrow \pi^+\pi^-$ reaction.

several hundred thousands in average (we recall that this bin corresponds to a particularly low Q^2 value). For the large $-t$ range -right figures-, i.e. away from the diffractive and exponentially falling t distributions and where the cross sections are the smallest, count rates are lower. The count rates are not directly proportional to the cross sections since the CLAS12 acceptance, which is larger at large $-t$, also enters into account. The black points in Fig. 24 are actually the red points corrected by the CLAS12 acceptance. It can indeed be seen that the $\cos(\theta_{cm})$ distribution of the red histogram (i.e. the number of accepted events in CLAS12) is not uniform and will need to be acceptance-corrected. The difference between the upper and lower plots of Fig. 24 is the nature of the error bars. In the upper plots, it is purely the statistical error bar while for the lower panels, it is the quadratic sum of the statistical error and of 10% which correspond to the expected systematic error due,

in major part, to the subtraction of the non-resonant 2-pion background under the ρ^0 peak (see section VII A 3).

The black curve in Fig. 24 is a fit to the black points by Eq. 4. The fitted value of r_{00}^{04} and its error is displayed in every panel. The figure shows that the 10% systematic error that we have introduced is by far the dominant source of uncertainty, even at large $-t$. The error on r_{00}^{04} is obviously higher when the systematic errors are introduced. Fig. 24 nevertheless shows that r_{00}^{04} can be extracted in this particular (x_B, Q^2) bin at a few percent level.

Fig. 25 shows the same simulations for another (x_B, Q^2) bin: $0.7 \leq x_B \leq 0.75, 10.5 \leq Q^2 \leq 11$, i.e. at a large Q^2 than the bin of Fig. 24, again for two t ranges ($0 < -t < 1$ -left plots- and $6 < -t < 10$ -right plots-). The red histograms, to which the vertical scale corresponds, are the expected number of accepted events. It is seen that we have less counts than in Fig. 24, of course due to the highest Q^2 value. Again, the black points are the red points corrected by the CLAS12 acceptance and the upper plots have only a statistical error bar while the lower plots have the quadratic sum of the statistical error and of anticipated 10% systematic error. Fig. 25 shows that even at large Q^2 and large $-t$, we should be able to extract the r_{00}^{04} SDME at the few percent level.

We have focused here on the particular r_{00}^{04} SDME, which is the particular one which gives access to the important ratio $R = \frac{\sigma_L}{\sigma_T}$. A more complete analysis of the decay angular distribution of the ρ^0 is obviously possible, giving access to all other SDMEs, providing important additional informations on the various helicity amplitudes participating to the process $\gamma^* p \rightarrow \rho^0 p$. For a polarized beam and an unpolarized target, 23 SDMEs are accessible. We do not discuss here in details the extraction of all these SDMEs since this involves an elaborated and sophisticated 3-dimensional angular analysis procedure whose accuracy is strongly dependent on the detailed understanding of the CLAS12 acceptance and also on the relative values of the SDMEs which are barely known in this energy region. It should nevertheless be clear that there will definitely be enough statistics and accuracy to perform such analysis, given an appropriate binning.

B. ϕ Simulations

The event generator for ϕ production has a commonly used form which has been used to fit CLAS published data.

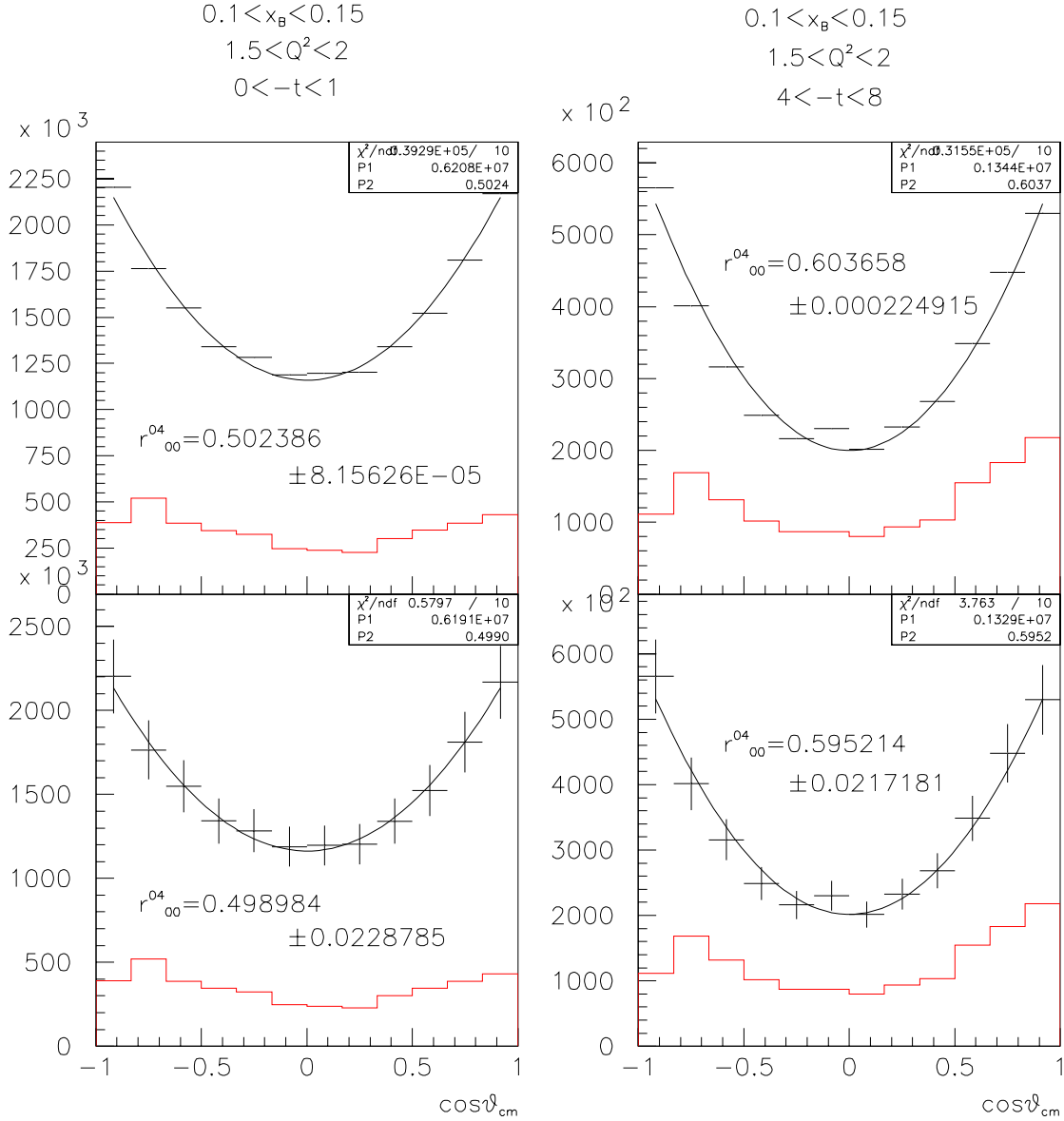


FIG. 24: Polar angle $\cos(\theta_{cm})$ distribution of the decay pion in the center of mass of the ρ^0 for the bin ($0.1 < x_B < 0.15$, $1.5 < Q^2 < 2$) and for two different $-t$ ranges ($0 < -t < 1$ -left plots- and $4 < -t < 8$ -right plots-). The red histogram, to which the vertical scale corresponds, is the expected number of accepted events (either an electron, a proton and a π^+ accepted or an electron, a π^+ and a π^- accepted). The black points are the expected reconstructed distributions. The difference between the black and red points is therefore the acceptance correction which has been applied to the black points. The black curve is the result of the fit of the black points by Eq. 4. Upper panels correspond to purely statistical error bars while lower panels correspond to the quadratic sum of the statistical error and of 10% systematic error.

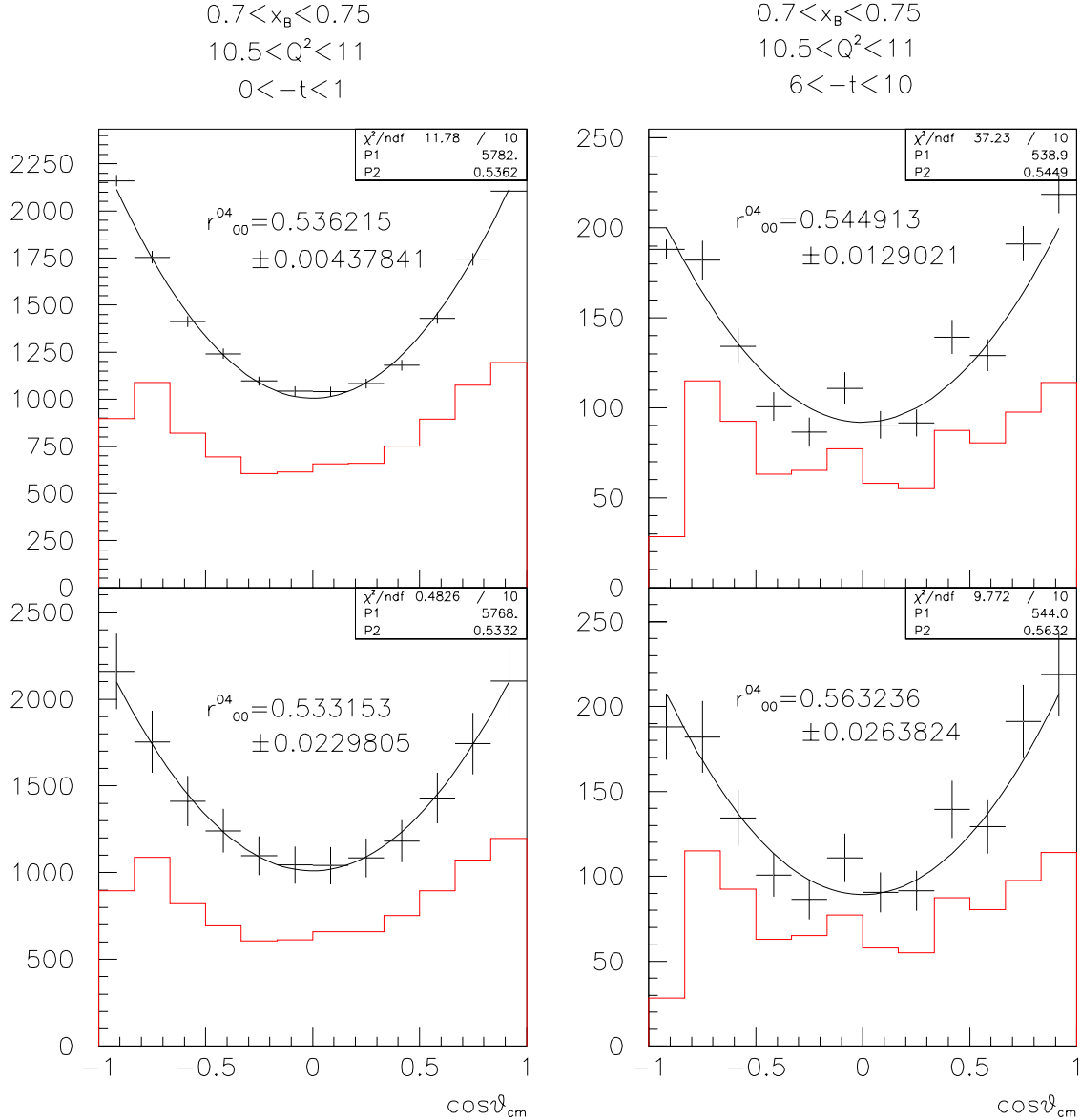


FIG. 25: Polar angle $\cos(\theta_{cm})$ distribution of the decay pion in the center of mass of the ρ^0 for the bin ($0.7 < x_B < 0.75$, $10.5 < Q^2 < 11$) and for two different $-t$ ranges ($0 < -t < 1$ -left plots- and $4 < -t < 8$ -right plots-). The red histogram, to which the vertical scale corresponds, is the expected number of accepted events (either an electron, a proton and a π^+ accepted or an electron, a π^+ and a π^- accepted). The black points are the expected reconstructed distributions. The difference between the black and red points is therefore the acceptance correction which has been applied to the black points. The black curve is the result of the fit of the black points by Eq. 4. Upper panels correspond to purely statistical error bars while lower panels correspond to the quadratic sum of the statistical error and of 10% systematic error.

$$\frac{d\sigma}{dQ^2 dx_B dt d\phi} = \Gamma(Q^2, x_B, M_p) \frac{1}{2\pi} \left[\sigma_T + \epsilon \sigma_L + \epsilon \sigma_{TT} \cos 2\phi + \sqrt{\epsilon(\epsilon + 1)} \sigma_{LT} \cos \phi + \lambda \sqrt{2\epsilon(\epsilon - 1)} \sigma'_{LT} \sin \phi \right]$$

The structure functions had the following forms

$$\sigma_T = \frac{\sigma^T \cdot e^{B_T(x_B) \cdot t}}{(Q^2 + M^2)^n} \quad B_T(x_B) = \alpha^T \cdot 2 \cdot 1.1 \cdot \ln(x_B)$$

$$\sigma_L = \frac{\sigma^L \cdot e^{B_L(x_B) \cdot t}}{(Q^2 + M^2)^n} \quad B_L(x_B) = \alpha^L \cdot 2 \cdot 1.1 \cdot \ln(x_B)$$

$$\sigma_{TT} = \frac{\sigma^{TT} \cdot (t - t_{min}) \cdot e^{B_{TT}(x_B^t) \cdot t}}{(Q^2 + M^2)^n} \quad B_{TT}(x_B) = \alpha^{TT} \cdot 2 \cdot 1.1 \cdot \ln(x_B)$$

$$\sigma_{LT} = \frac{\sigma^{LT} \cdot (t - t_{min}) \cdot e^{B_{LT}(x_B^t) \cdot t}}{(Q^2 + M^2)^n} \quad B_{LT}(x_B) = \alpha^{LT} \cdot 2 \cdot 1.1 \cdot \ln(x_B)$$

$$\sigma'_{LT} = 0$$

The constants $\alpha^T, \alpha^L, \alpha^{TT}, \alpha^{LT}$ and n are adjusted so that the cross sections agree with the measured CLAS ϕ production results [32]. Their values are $\alpha^T = 0.899$, $\alpha^L = 0.4359$, $\alpha^{TT} = 0.7188$, $\alpha^{LT} = 0.5799$ and $n = 2.428$.

The variables used are defines as follows:

The virtual photon flux is given by
$$\Gamma = \frac{2\alpha \cdot W \cdot (W^2 - M_p^2)}{(2\pi \cdot (s_{tot} - M_p^2)^2 \cdot Q^2) \cdot (1 - \epsilon)}$$
,

the virtual photon polarization is
$$\epsilon = \frac{(1 - y - (y \cdot x_B \cdot M_p)^2 / Q^2)}{(1 - y + y^2 / 2 + (y \cdot x_B \cdot M_p)^2 / Q^2)}$$

the Bjorken variable
$$x_B = \frac{Q^2}{(W^2 - M_p^2 + Q^2)}$$

the electron fractional loss
$$y = \frac{Q^2}{x_B \cdot (s_{tot} - M_p^2)}$$

The Mandelstam variable
$$s_{tot} = M_e^2 + 2 \cdot E \cdot M_p + M_p^2$$
.

The number of measured events in the experiment is related to the cross section by

$$N = \sigma \cdot L_{int} \cdot Br \cdot eff.$$

which is related to the differential cross section at Q^2, W and t as

$$\sigma = \frac{1}{\Gamma} \frac{d^2\sigma}{dQ^2 \cdot dW}$$

The differential cross section at Q^2, W and t is then related to the number of observed events in an interval $\Delta Q^2 \cdot \Delta W \cdot \Delta t$ by

$$\frac{d^3\sigma}{dQ^2 \cdot dW \cdot dt} = \frac{N}{\Delta Q^2 \cdot \Delta W \Delta t \cdot L \cdot Br \cdot eff.}$$

1. ϕ decay modes

The ϕ meson has the following leading decay modes: $\phi \rightarrow K^+K^-$ with a branching ratio of 49% and $\phi \rightarrow K_S^0 K_L^0$ with $K_S^0 \rightarrow \pi^+\pi^-$ with a branching ratio of 34%. We anticipate utilizing all analysis tools at our disposal to minimize continuum pion backgrounds. Fortunately, the exclusivity of the reaction of interest will offer several handles for selection of kaons.

The first line of selection will utilize the time of flight (TOF) difference of pions and kaons having the same measured momentum. However, as the momenta increases the (TOF) difference decreases, so that at momenta between 4 and 5 GeV² the TOF resolution of the CLAS12 spectrometer (.08 ns) makes a TOF cut less affective. But, the low threshold Cerenkov detector threshold for pion detection is about 2.2 GeV, so that the low threshold Cerenkov detector becomes effective in vetoing pion background from the kaon events. Further selection of kaons occurs by obtaining missing mass of the detected e, p and K^\pm , and applying selection cuts around the resulting K^\pm peak in the missing mass spectrum. Other handles include missing momentum, energy and coplanarity cuts. Finally, at a particular $Q^2, Wandt$ there is a strong correlation between the momentum and direction of the detected kaon and missing kaons emerging from the ϕ since the ϕ has a very narrow energy width ($\Gamma \sim 4.3$ MeV) and the decay kinetic energy of each kaon in the ϕ cm frame is only 17 MeV. Thus, boosted into the lab they will tend to be rather co-directional.

Rather detailed simulations are being carried out for the $K^+ - K^-$ decay channel, the status of which are discussed below.

For the simulation the CLAS12 Fast-MC program was used. 10^7 events were generated, which corresponds 60 days beam time at the CLAS12 luminosity $L = 1 \times 10^{35} \text{ cm}^2\text{s}^{-1} \sim 100$ events/nb at the CLAS published cross sections. The particles required to be detected were the e, p and K^+ . As in earlier experiments[32]the K^- is assumed to be constructed from the missing mass of the e, p, K^+ . Background especially due to Λ production was not yet simulated. Because the acceptance and event rates are rather high, the coincidence of all the final state particles e, p, K^+, K^- will be investigated.

The Cross section was calculated for 0.5 GeV intervals of W , 1.0 GeV^2 intervals of Q^2 , and 0.5 GeV intervals of t . The differential cross section was calculated as function of t from 0 to 10 GeV with step 1.0 GeV The following figures give examples the acceptances and event statistics based on 60 days of 11 GeV beam at a luminosity of $1 \times 10^{35} \text{ cm}^2\text{sec}^{-1}$.

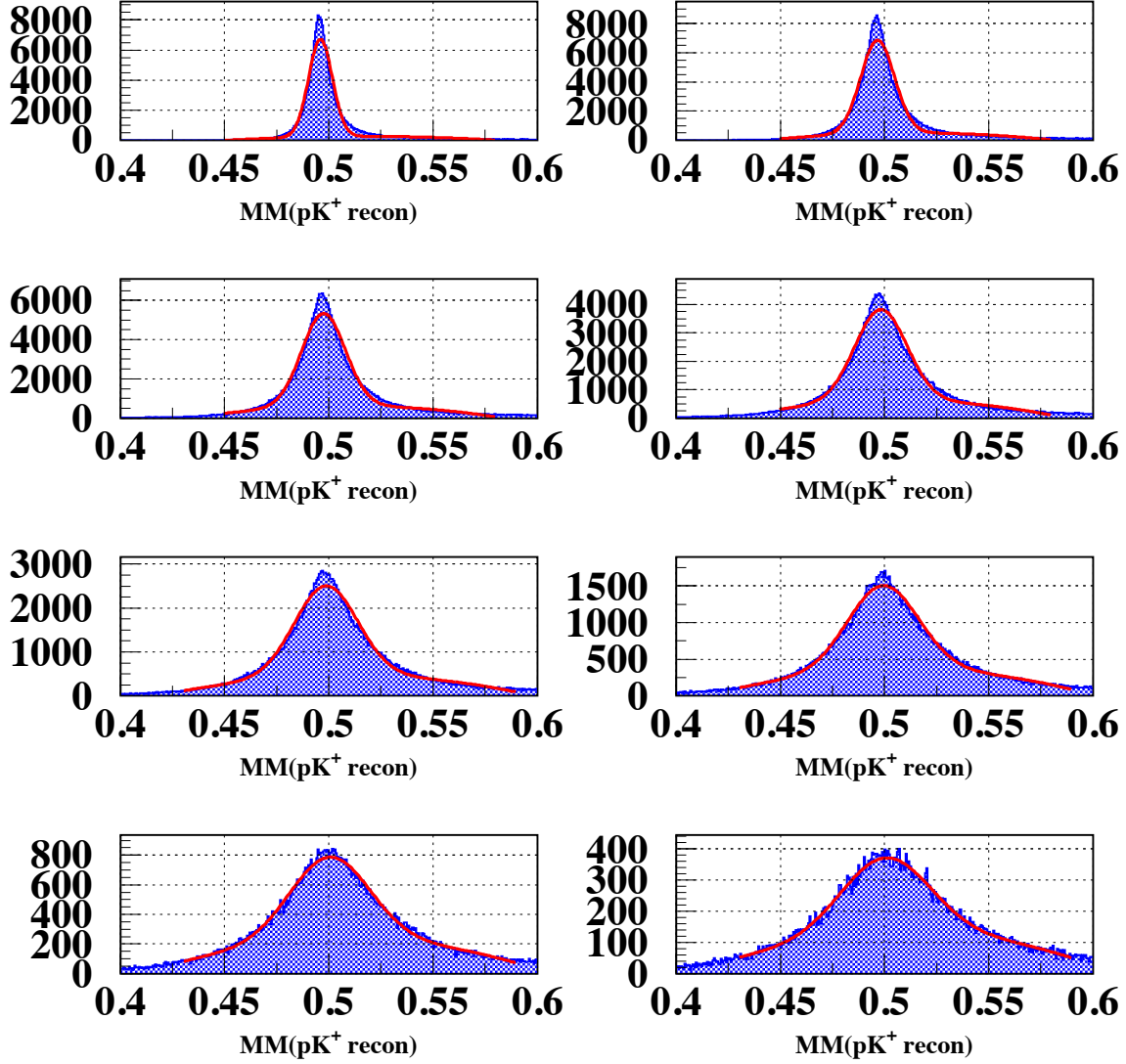


FIG. 26: Left: Missing mass distribution for detected e, pK^+X . Right: The resolution σ of the missing mass as a function of missing momentum, from 1.45 (upper left) to 4.45 (lower right) GeV^2/c . Note that the resolution on the missing K^+ becomes progressively broader as its momentum increases.

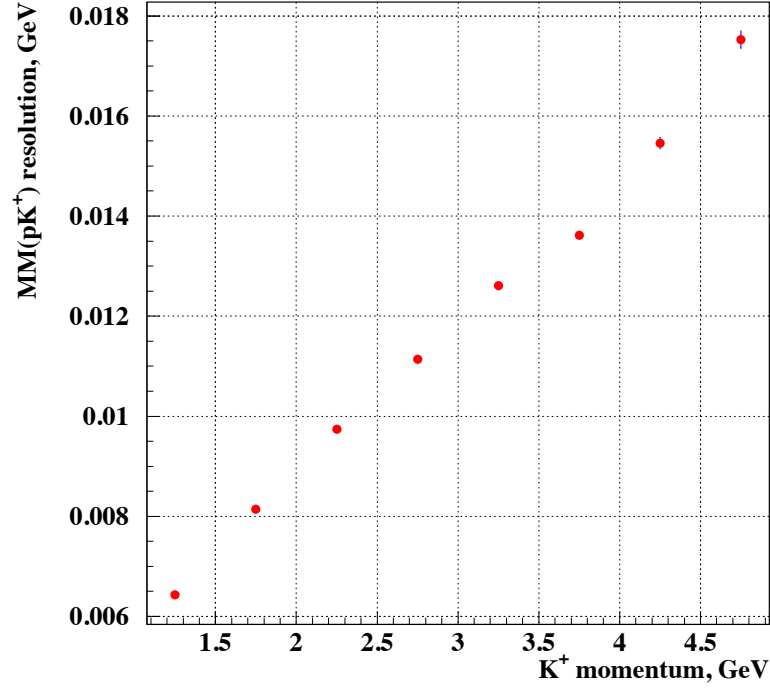


FIG. 27: Missing mass resolution σ_{rms} vs. K^+ momentum p corresponding to the curves in Fig 26

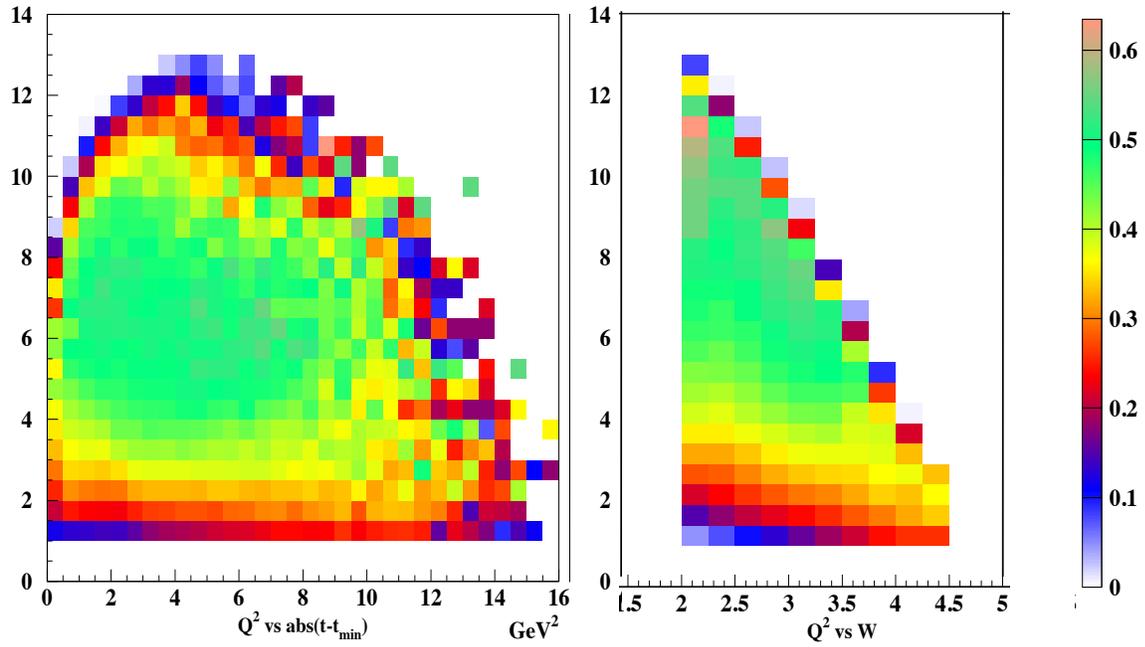


FIG. 28: Acceptance for ϕ production. Left: as a function of Q^2 and $t - t_{min}$ integrated over W . Right: as a function of Q^2 and W integrated over t .

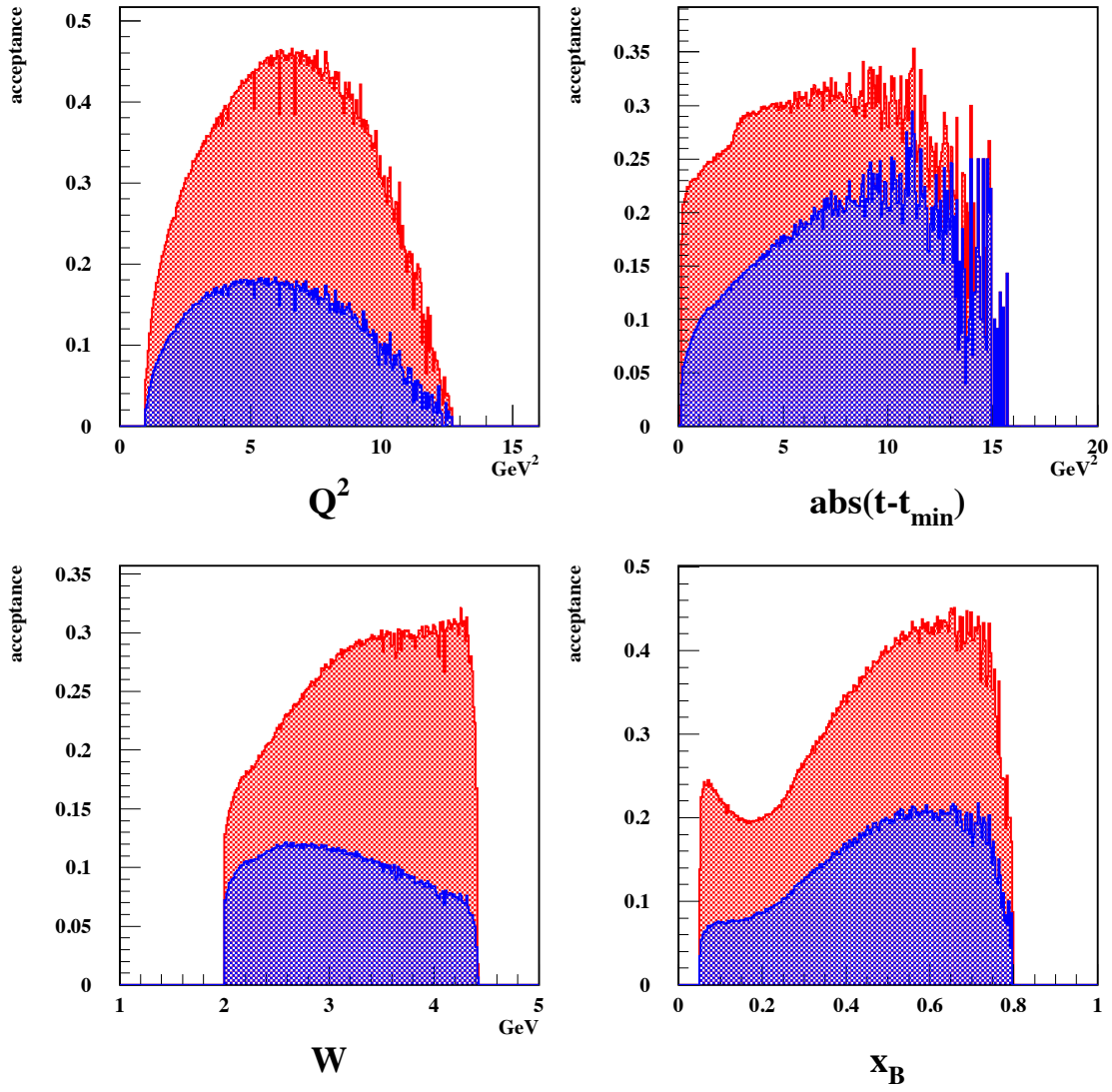


FIG. 29: Acceptance for ϕ production as a function of Q^2 , $t - t_{\min}$, W and x_B . For each graph, the acceptance is the integral over all the other kinematic variables. The red represents the case where detection of the e' , p and K^+ are required, while the blue also requires the detection of the K^- as well.

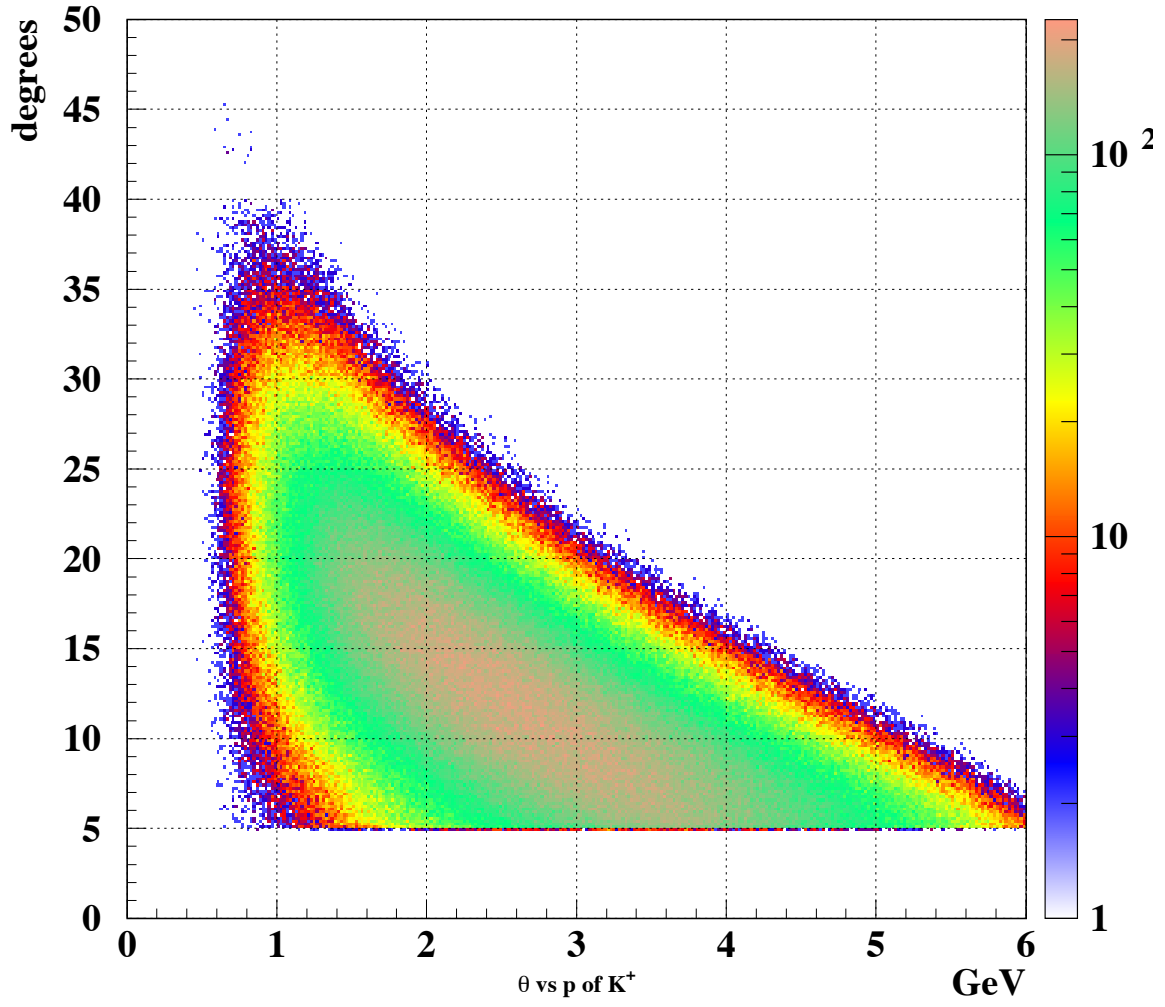


FIG. 30: Angular distribution of the detected K^+ mesons corresponding the decay of the ϕ with the requirement that K^+, p and e are detected.

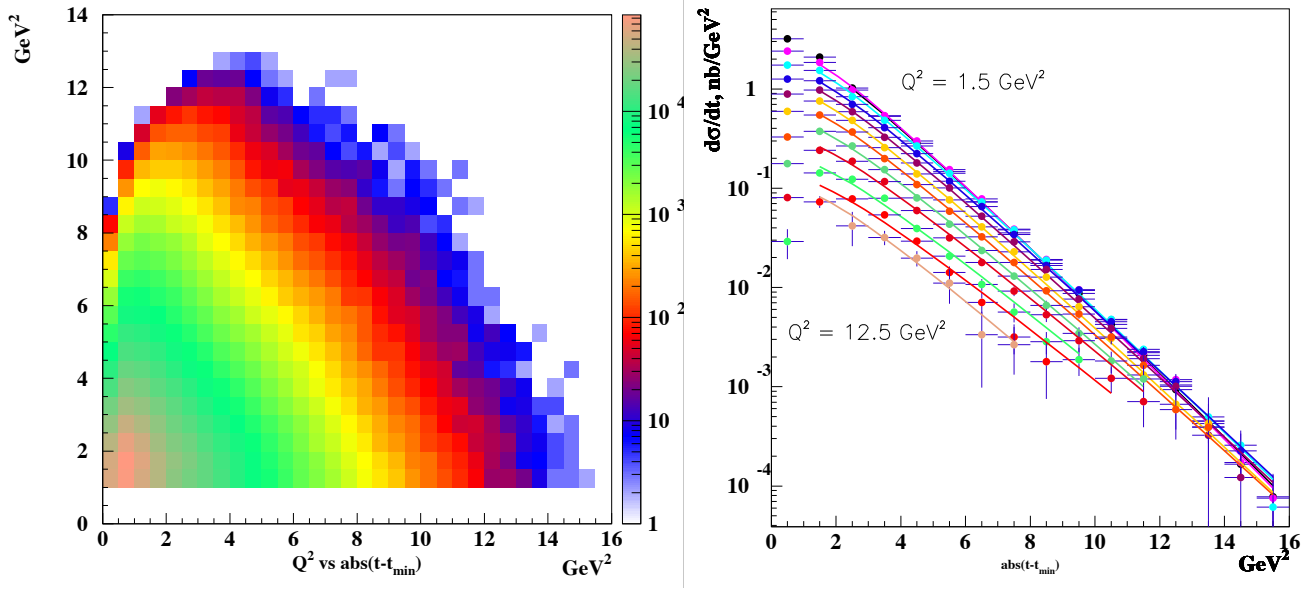


FIG. 31: Left: Total number of events for ϕ production as a function of Q^2 : and $t - t_{\min}$. Right: Cross section as a function of t for Q^2 bins corresponding to the figure at left. All accepted W were included

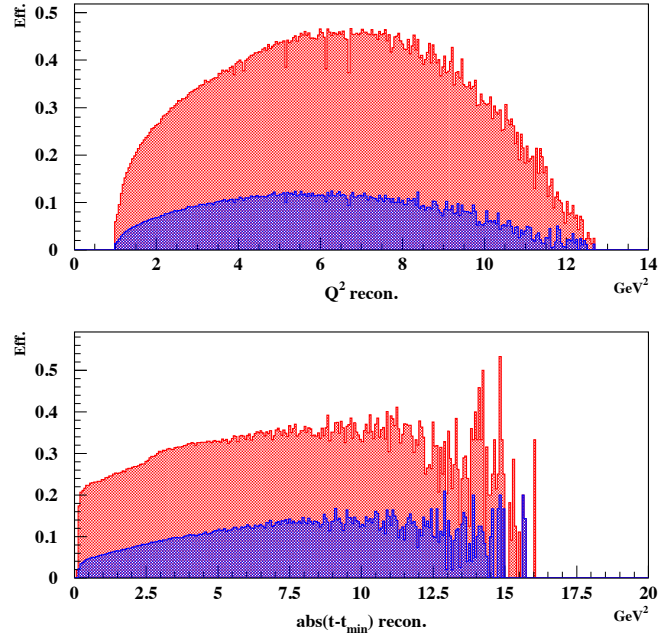


FIG. 32: The acceptances for $\phi \rightarrow K^+K^-$ (red) and for $\phi \rightarrow K_S^0 K_L^0$ with $K_S^0 \rightarrow \pi^+ \pi^-$ (blue)

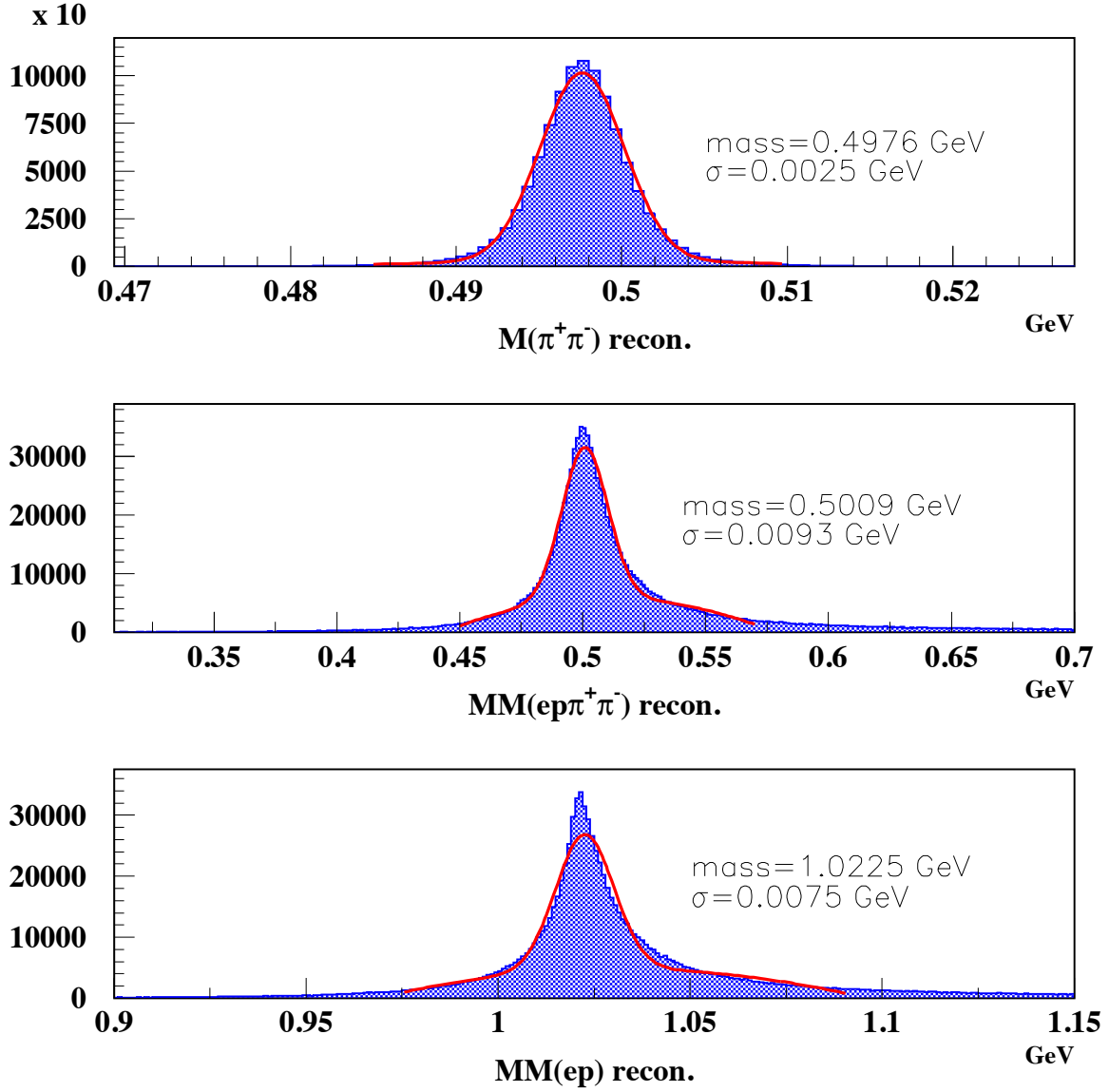


FIG. 33: Resolution for $K_S^0 \rightarrow \pi^+\pi^-$, $MM(ep\pi^+\pi^-)$ and $MM(ep)$ spectra. The ϕ -meson should be visible in the missing mass of electron and proton if we reconstruct K_S^0 using detected pair of pions.

$$Q^2 = 2.5 \text{ GeV}^2$$

2011/05/27 1

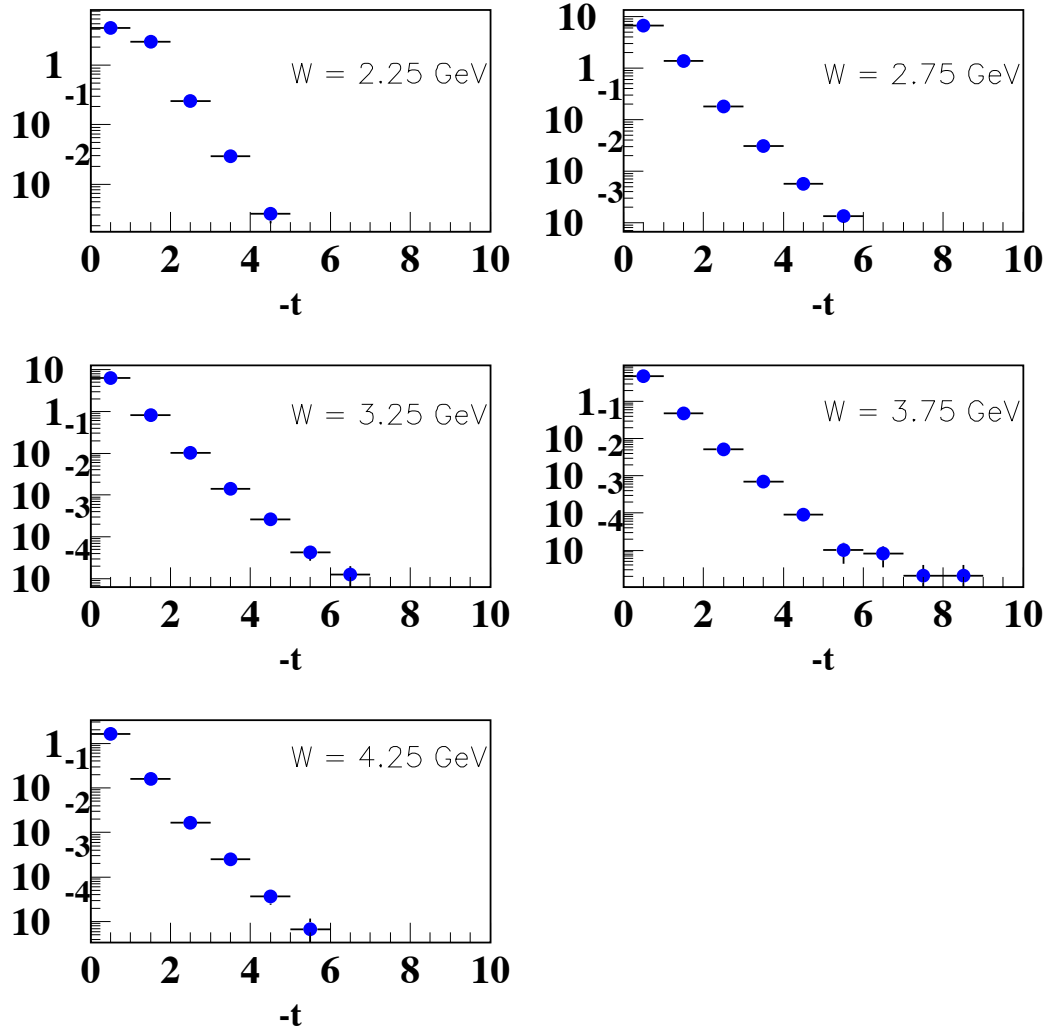


FIG. 34: Cross section as a function of t for $Q^2 = 2.5$ and bins in W corresponding to those of Fig. 31.

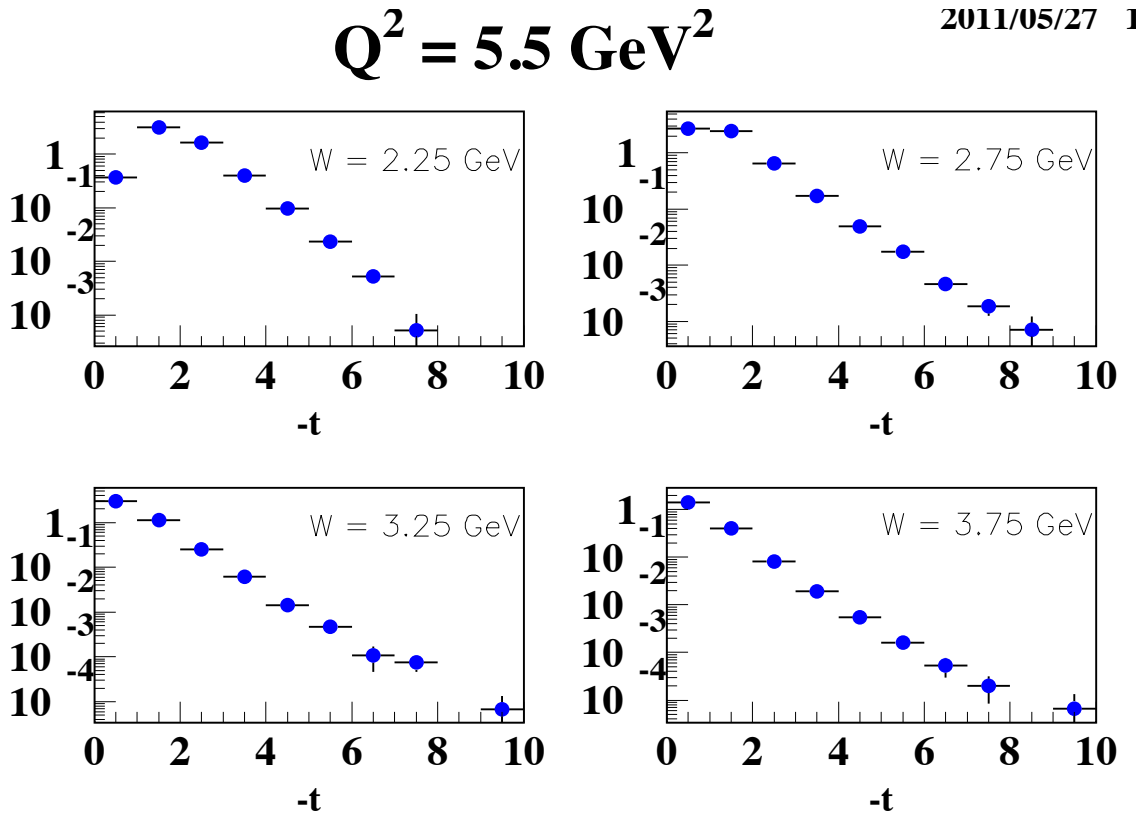
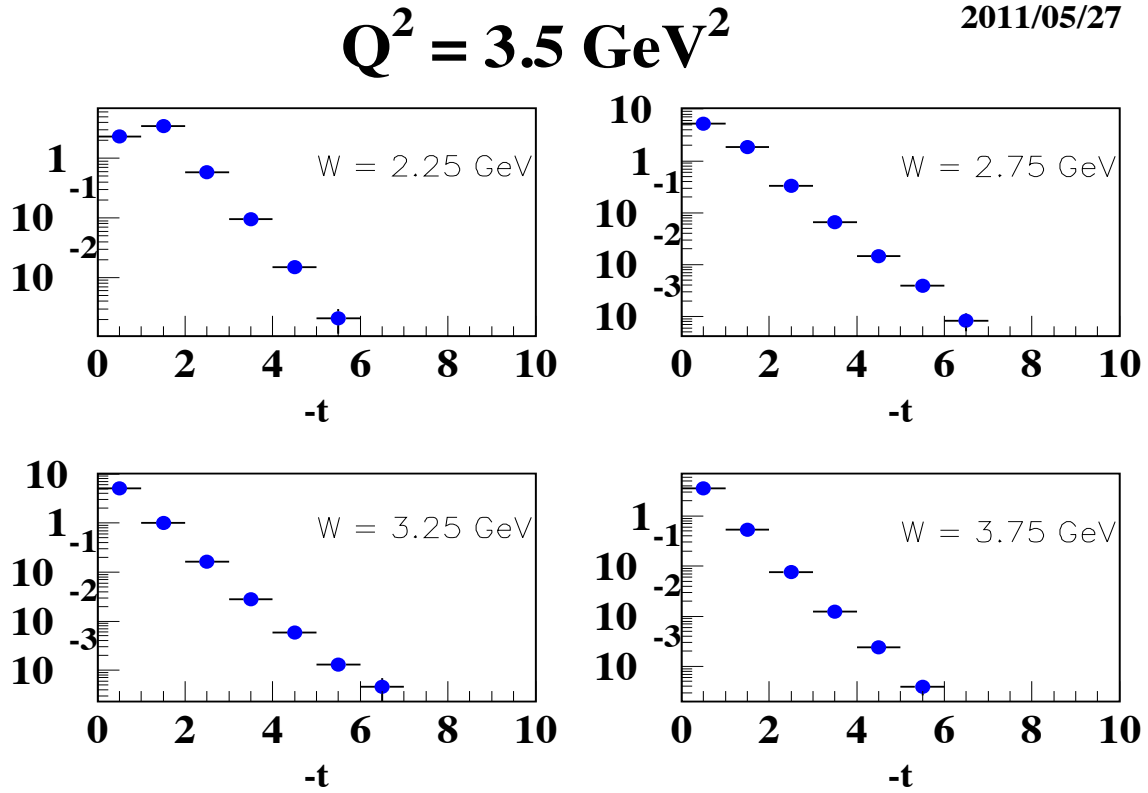
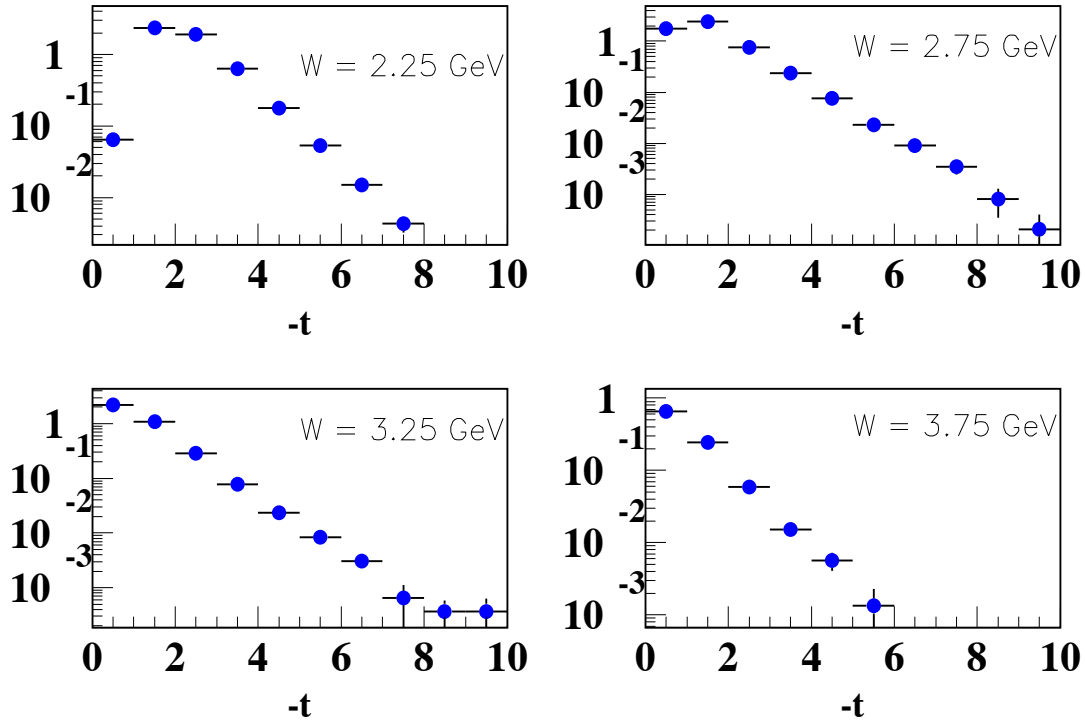


FIG. 35: Cross section as a function of t for $Q^2 = 3.5$ and $5.5 \text{ GeV}^2/c$ and bins in W corresponding to those of Fig. 31.

$$Q^2 = 6.5 \text{ GeV}^2$$

2011/05/27 17



$$Q^2 = 8.5 \text{ GeV}^2$$

2011/05/27

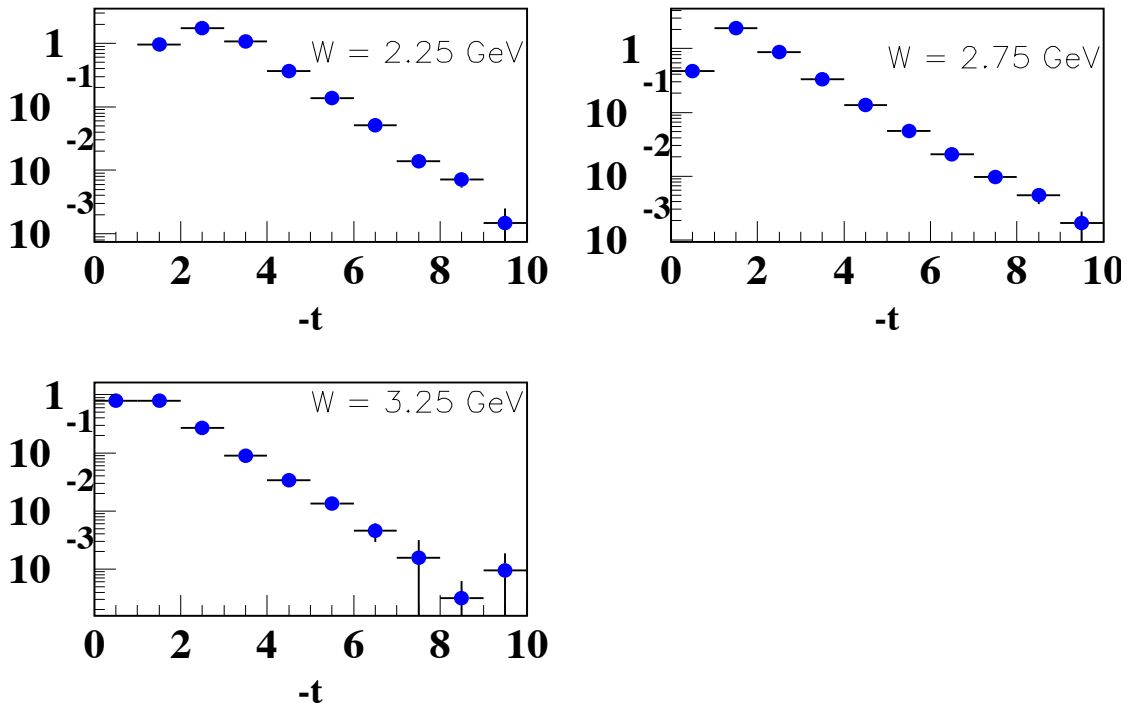
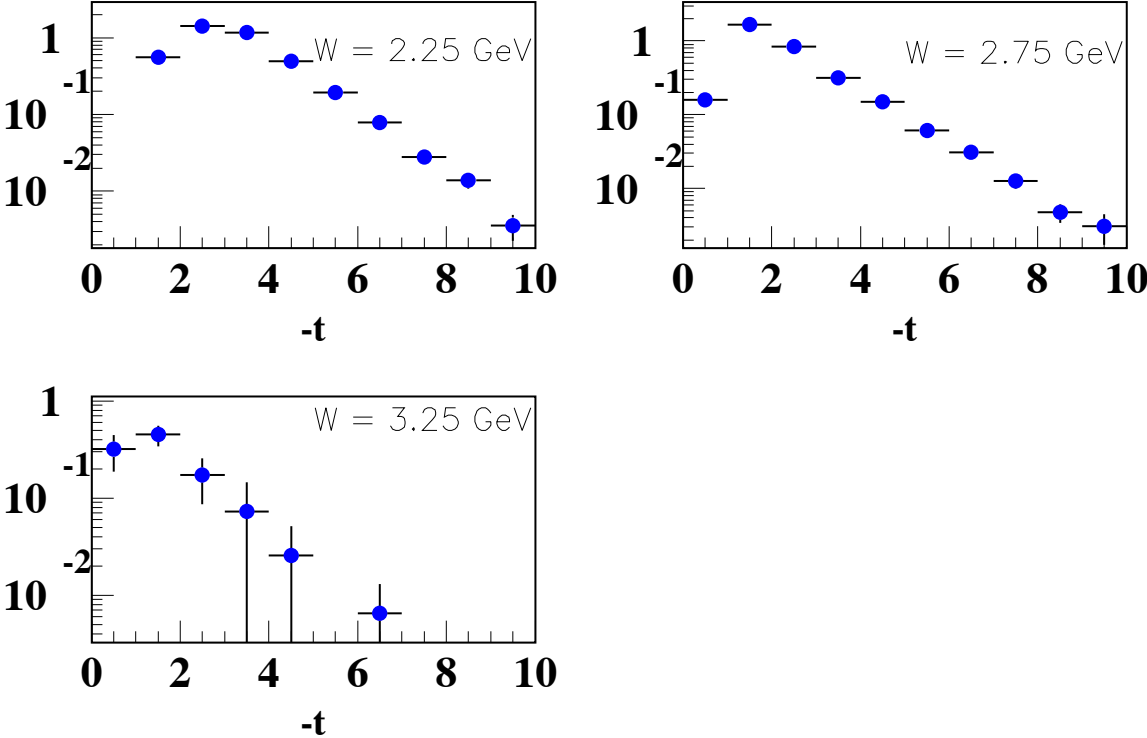


FIG. 36: Cross section as a function of t for $Q^2 = 6.5$ and $8.5 \text{ GeV}^2/c$ and bins in W corresponding to to those of Fig.31.

$Q^2 = 9.5 \text{ GeV}^2$

2011/05/27 1'



$Q^2 = 10.5 \text{ GeV}^2$

2011/05/27 17.

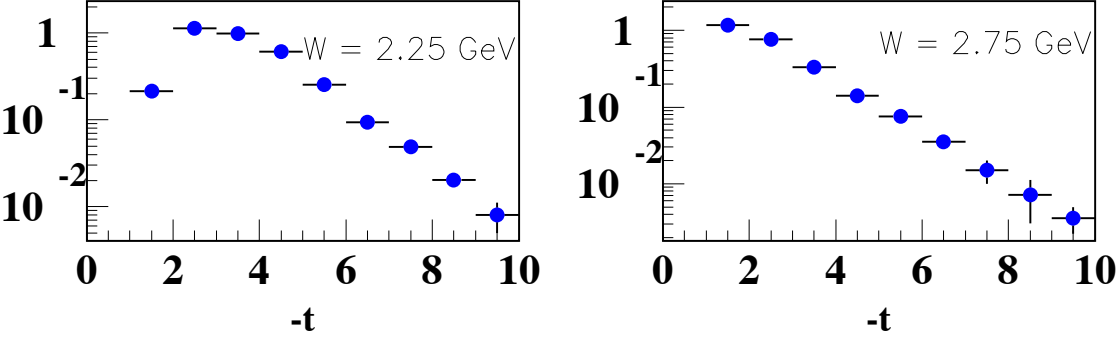


FIG. 37: Cross section as a function of t for $Q^2 = 9.5$ and $10.5 \text{ GeV}^2/c$ and bins in W corresponding to those of Fig. 31.

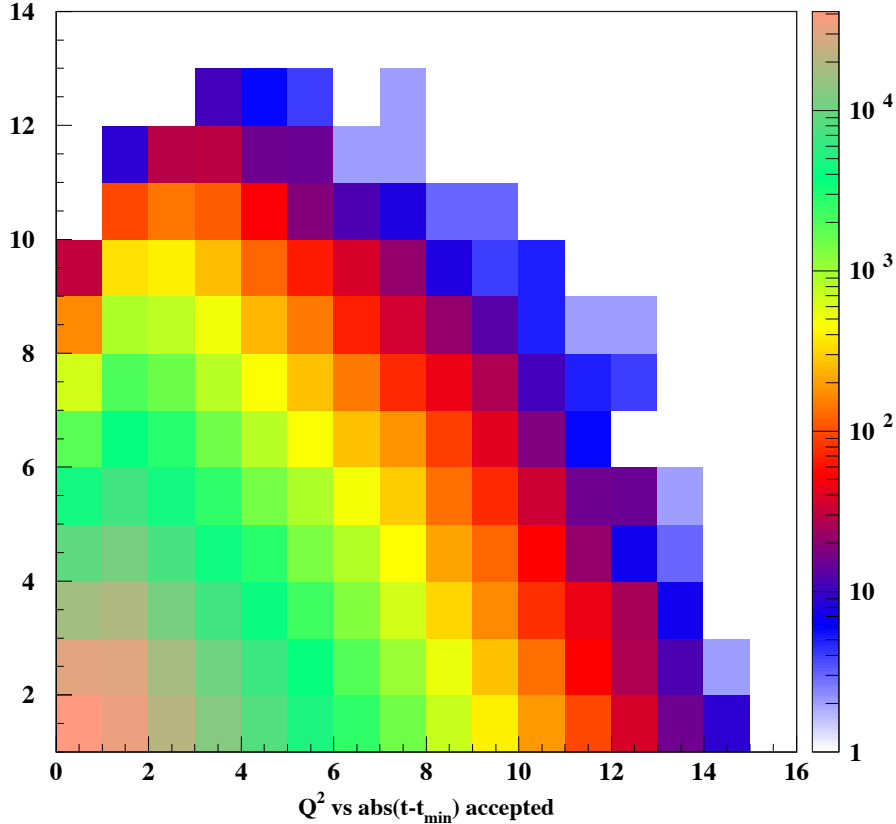


FIG. 38: Total number of accepted events for ϕ production in the $K_s K_L$ decay channel as a function of Q^2 and $t - t_{\min}$.

C. ρ^+ channel

1. Kinematics

We plan to measure the $ep \rightarrow en\rho^+ \leftrightarrow \pi^+\pi^0 \leftrightarrow \gamma\gamma$ reaction by detecting the scattered electron, the π^+ and the two photons coming from the decay of the π^0 . The neutron is determined from the missing mass $M_X(e\pi^+\pi^0 X)$. Fig. 39 shows the invariant mass of the two photons after passing through the FASTMC code which estimates the resolutions and the acceptances for the future CLAS12 detector. The $IM(\gamma\gamma)$ distribution is fitted with gaussian to describe the π^0 peak and 3rd degree polynomial to describe the combinatorial background. It is seen that a resolution for the invariant mass of the pion ≈ 17 MeV is obtain.

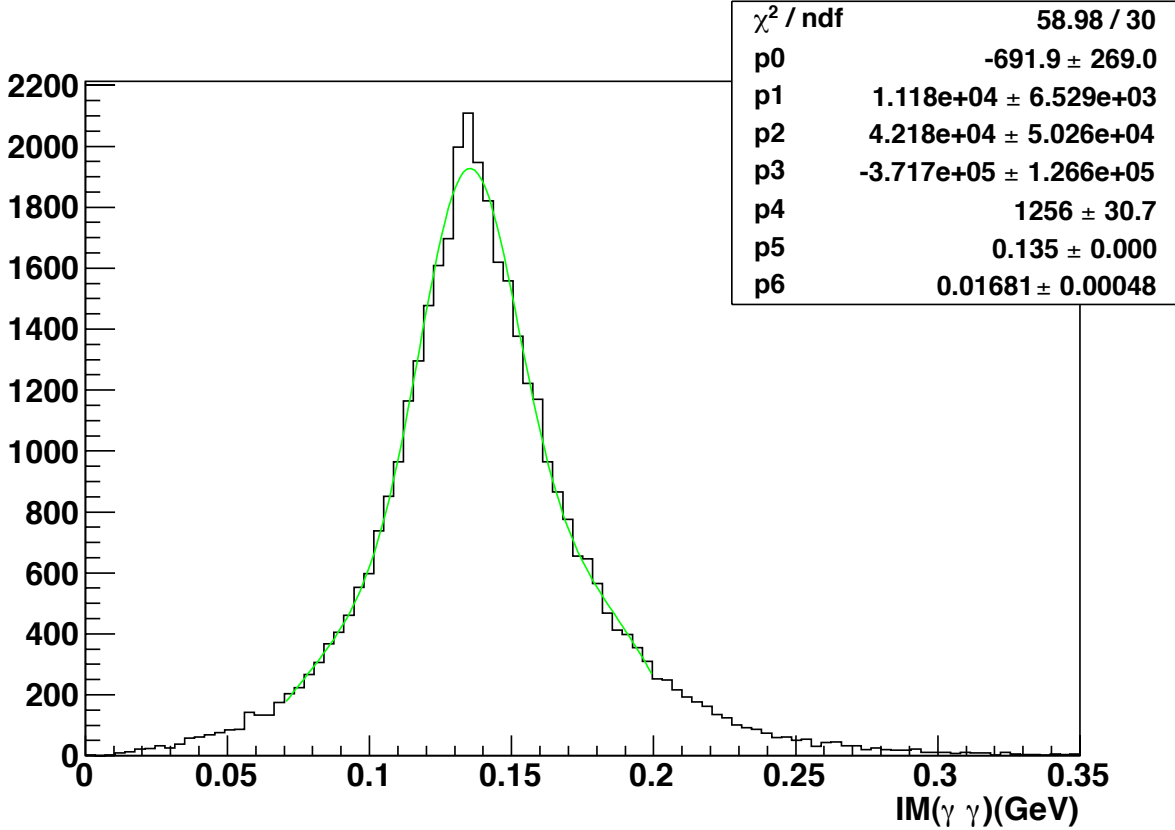


FIG. 39: In black, distribution of the invariant mass $IM(\gamma\gamma)$ for the $ep \rightarrow en\rho^+ \leftrightarrow \pi^+\pi^0 \leftrightarrow \gamma\gamma$ process. The green curve is the Gaussian + polynomial fit to the π^0 peak + background.

Fig. 40 shows the missing mass $M_X(e\pi^+\pi^0X)$ for the $ep \rightarrow en\rho^+ \leftrightarrow \pi^+\pi^0$ process (in black). This distribution is fitted with a gaussian to describe the neutron peak and 3rd degree polynomial to describe the background. The resolution of the neutron peak is ≈ 75 MeV. In Fig. 40, we also show, in blue, the distribution of $M_X(e\pi^+\pi^0X)$ for the exclusive 3-pion electroproduction process $ep \rightarrow e\pi^+\pi^-\pi^0$, which gives continuum instead of the neutron peak. In this figure, the normalization has been taken equal for the two processes $ep \rightarrow en\rho^+ \leftrightarrow \pi^+\pi^0$ and $ep \rightarrow e\pi^+\pi^-\pi^0$ over the same $(x_B, Q^2, -t)$ phase space. The assumption behind this is that the cross sections of these two processes are equal on this same phase space, which is a very conservative hypothesis. Fig. 40 shows that we shall be able to distinguish the exclusive ρ^+ electroproduction reaction from the 3-pion process.

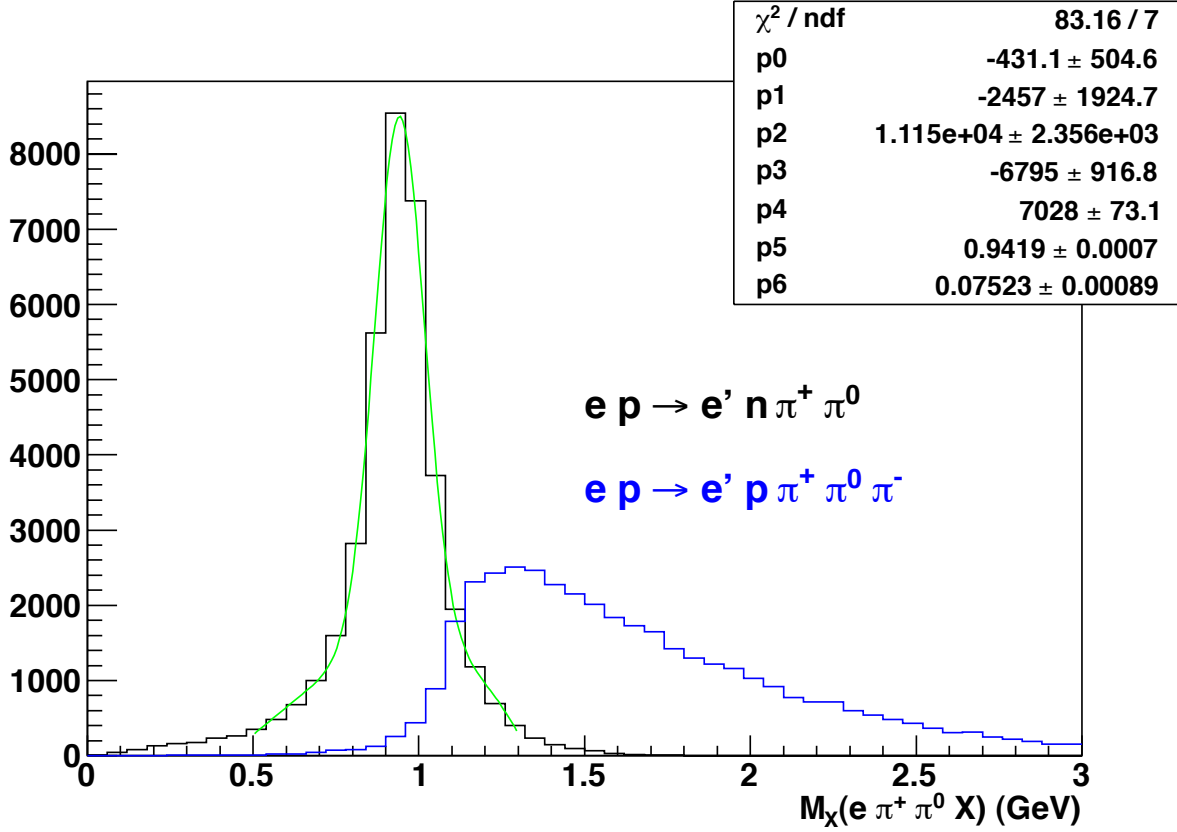


FIG. 40: In black, distribution of the missing mass $M_X(e\pi^+\pi^0 X)$ for the $ep \rightarrow en\rho^+ \leftrightarrow \pi^+\pi^0$ process. The green curve is the Gaussian + polynomial fit to the neutron peak + background. In blue, distribution of the missing mass $M_X(e\pi^+\pi^0 X)$ for the $ep \rightarrow e\pi^+\pi^-\pi^0$ process.

Fig. 41 shows the kinematical planes (Q^2, x_B) , (Q^2, W) and (Q^2, t) which can be accessed with an 11 GeV electron beam for the $ep \rightarrow en\rho^+ \leftrightarrow \pi^+\pi^0 \leftrightarrow \gamma\gamma$ process. The distributions have been generated according to realistic cross sections using the generator GENEV. In Fig. 41, the black areas show the theoretical phase spaces which are in principle accessible. The superposed colored areas show these same phase spaces when we request the detection in CLAS12 (using the FASTMC code) of an electron, a π^+ and 2 photons in the final state.

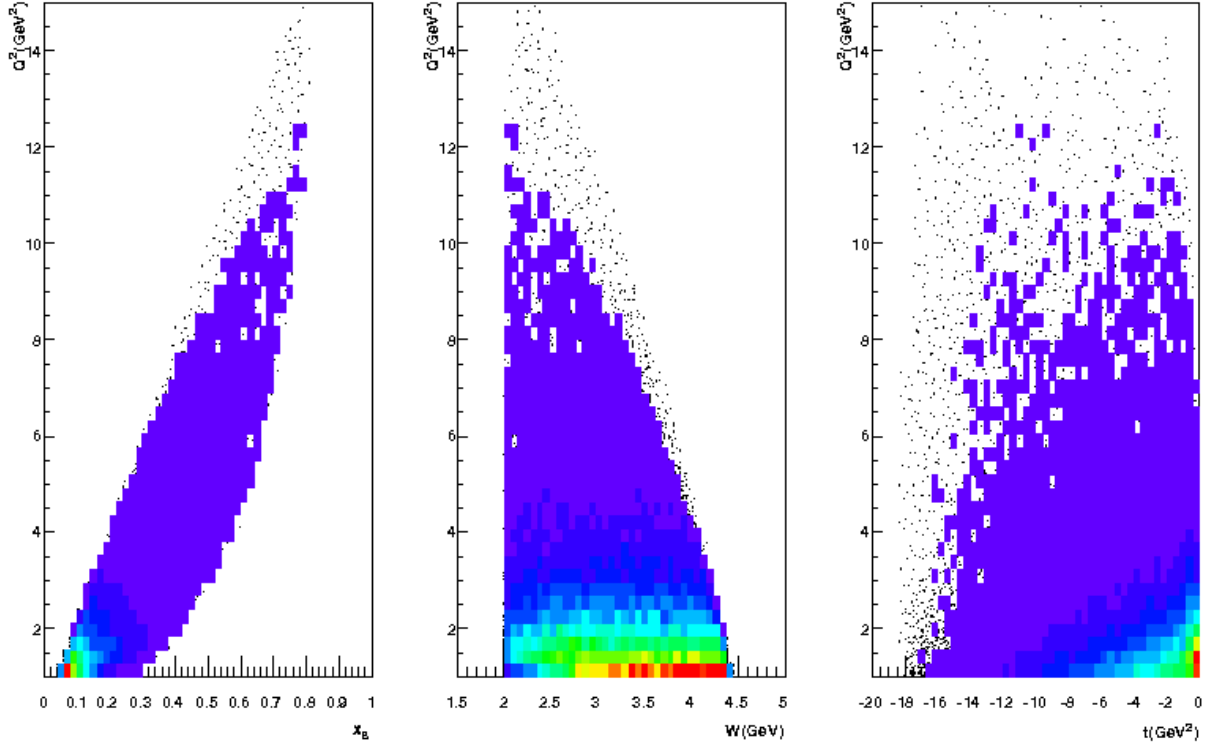


FIG. 41: Kinematic planes Q^2 vs x_B , W and t for the $ep \rightarrow en\rho^+ \leftrightarrow \pi^+\pi^0 \leftrightarrow \gamma\gamma$ reaction. Black points: without any requirement on the detection of the particles. Colored points: with the requirement of the detection of an electron, a π^+ and 2 photons in CLAS12 (using the CLAS12 FASTMC code).

Fig. 42 shows the (θ, E) phase spaces of the required detected particles in the final state: the electron, the π^+ and the two photons coming from the decay of the π^0 . The electrons are detected in the electromagnetic calorimeter (EC) which extend to $\approx 40^\circ$. Note in Fig. 42 the “discontinuity” in the detected π^+ around $\theta = 40^\circ$ which marks the separation between the forward and central parts of CLAS12. Finally, the photons are detected in two regions: small θ region ($2.5^\circ < \theta < 4.5^\circ$) which corresponds to the Forward Tagger and large θ region (up to $\approx 40^\circ$) which corresponds to the electromagnetic calorimeter (EC).

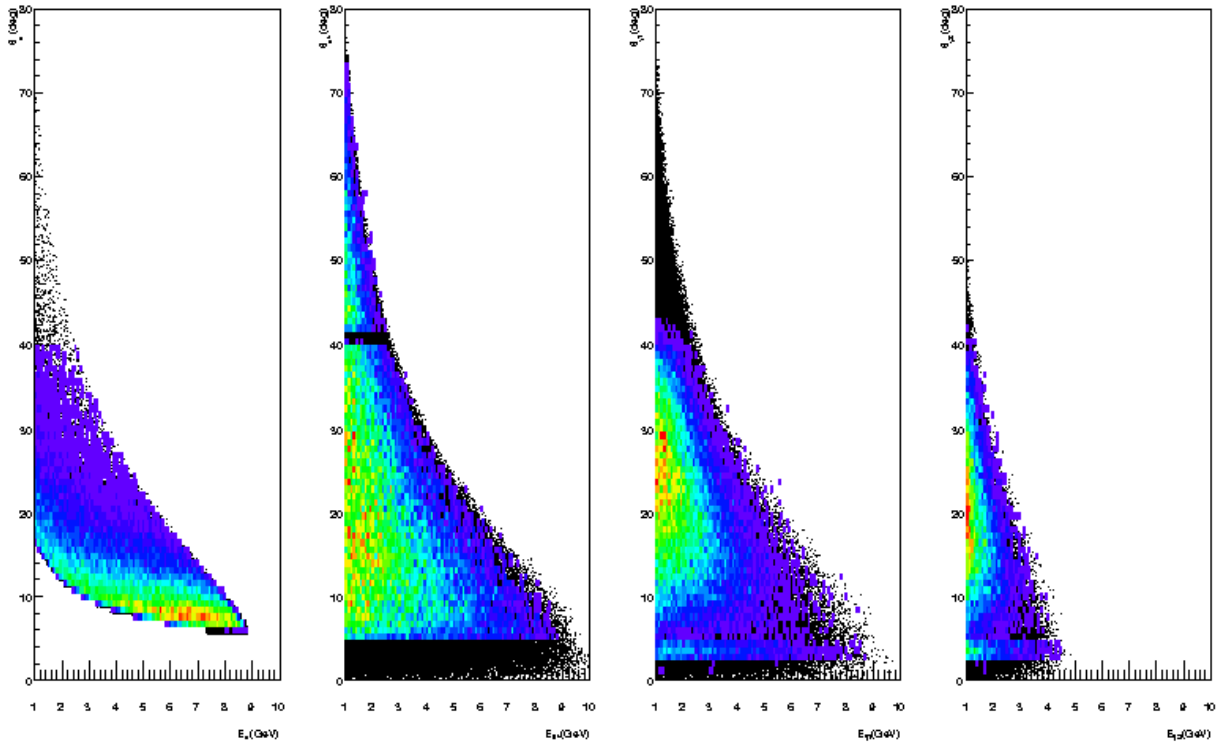


FIG. 42: Polar angle θ vs energy E for the electron (left panel), the π^+ (center panel) and the photons coming from the π^0 decay in the $ep \rightarrow en\rho^+ \leftrightarrow \pi^+\pi^0 \leftrightarrow \gamma\gamma$ reaction according to our event generator. Black points: without any requirement on the detection of the particles. Colored points: with the requirement of the detection of an electron, a π^+ and 2 photons in CLAS12.

2. Acceptance

The acceptance of CLAS12 has been determined by again using the FASTMC code. We show in Fig. 43 the x_B , W , Q^2 and t distributions of the generated events (black lines) and those of the accepted events (red, green and blue lines). The red curve corresponds to the “topology”: electron, π^+ and 2 photons detected in CLAS12. The green curve corresponds to the “topology”: electron,

π^+ and neutron detected in CLAS12. Neutrons can be detected in CLAS12 in the Electromagnetic Calorimeter EC ($4.5^\circ < \theta_n < 40^\circ$ with $\approx 30\%$ of efficiency) or in the new Central Neutron Detector CND ($40^\circ < \theta_n < 70^\circ$ with $\approx 10\%$ of efficiency). Figure 44 shows the (p_n, θ_n) phase space of the neutron when we require an electron, a π^+ and a neutron in

the final state. One finds that about 20 % of neutrons can be detected in the CND. On the Fig. 43, we remark that the large $-t$ region is better accessed in the second “topology” when we require the detection of the neutron. By making the ratio of the accepted distributions to the generated ones, so that the (integrated) acceptance values of CLAS12, determined by FASTMC, for the $ep \rightarrow en\rho^+ \leftrightarrow \pi^+\pi^0$ reaction are in average of the order of few percent (2-5%), of course depending on the kinematics. For sake of completeness, we also present (blue curve) in Fig. 43 the “topology” : an electron, a π^+ , a neutron and 2 photons detected in CLAS12, i.e. all five particles of the final state detected in CLAS12. This corresponds of course to the lowest acceptance.

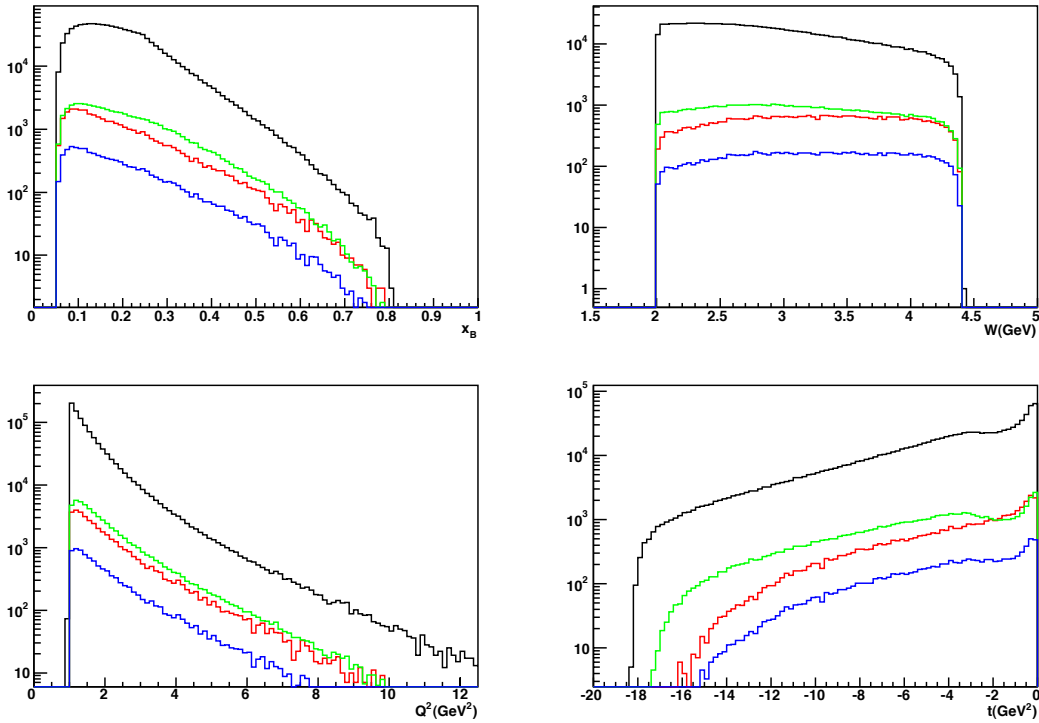


FIG. 43: Distributions of the generated events (black curves) and of the accepted events (red, green and blue curves) in CLAS12, as determined by FASTMC, as a function of x_B , W , Q^2 and t . The red curve corresponds to the “topology” : an electron, a π^+ and 2 photons detected in CLAS12, the green curve corresponds to the “topology” : an electron, a π^+ and a neutron detected in CLAS12 and the blue curve corresponds to the “topology” : an electron, a π^+ , a neutron and 2 photons detected in CLAS12.

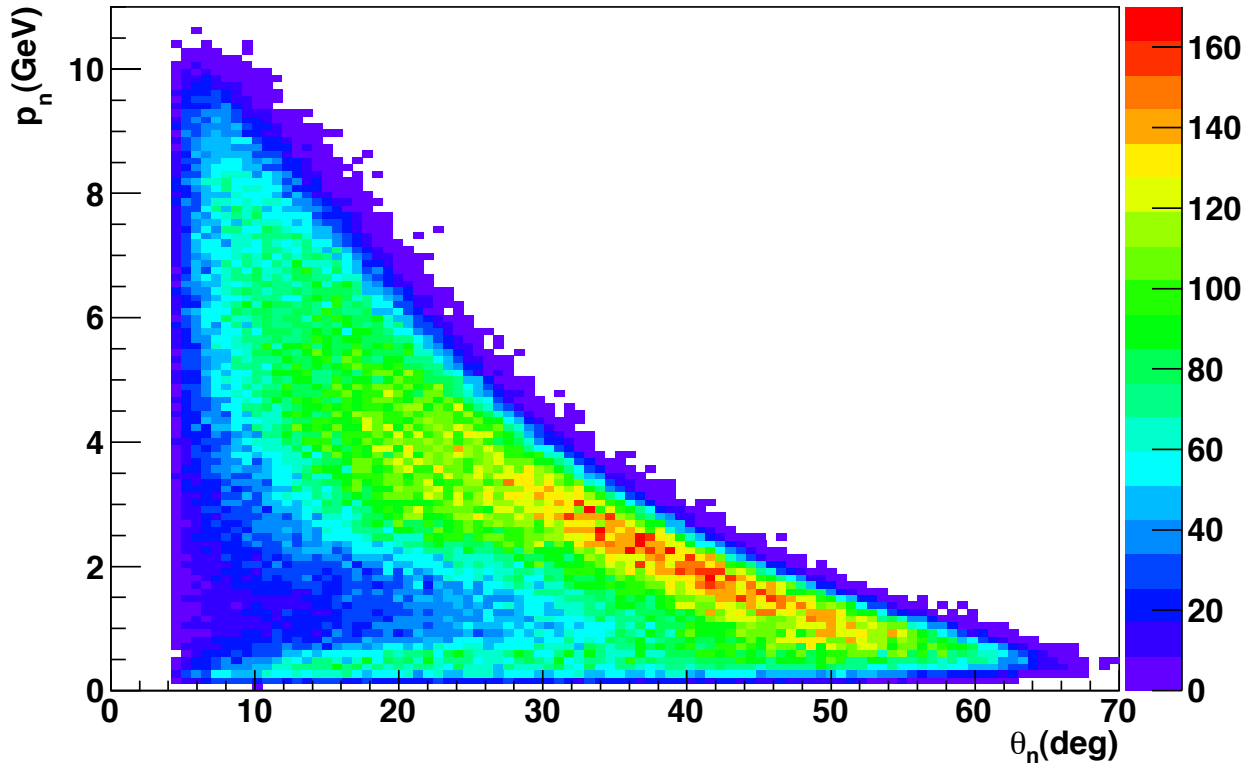


FIG. 44: Momentum p_n vs polar angle θ_n for the neutron in the $ep \rightarrow en\rho^+ \leftrightarrow \pi^+\pi^0 \leftrightarrow \gamma\gamma$ reaction with the requirement of the detection of an electron, a π^+ and a neutron in CLAS12.

D. ω channel

1. Kinematics

We plan to measure the $ep \rightarrow ep\omega \leftrightarrow \pi^+\pi^-\pi^0 \leftrightarrow \gamma\gamma$ reaction by detecting the scattered electron, the proton, the π^+ and the π^- . The π^0 is determined from the missing mass $M_X(ep\pi^+\pi^-X)$. Fig. 45 shows the kinematical planes (Q^2, x_B) , (Q^2, W) and (Q^2, t) which can be accessed with an 11 GeV electron beam for the $ep \rightarrow ep\omega \leftrightarrow \pi^+\pi^-\pi^0 \leftrightarrow \gamma\gamma$ process. The distributions have been generated according to realistic cross sections using the generator GENEV. In Fig. 45, the black areas show the theoretical phase spaces which are in principle accessible. The superposed colored areas show these same phase spaces when we request the detection in CLAS12 (using the FASTMC code) of an electron, a proton, a π^+ and a π^- in the final state.

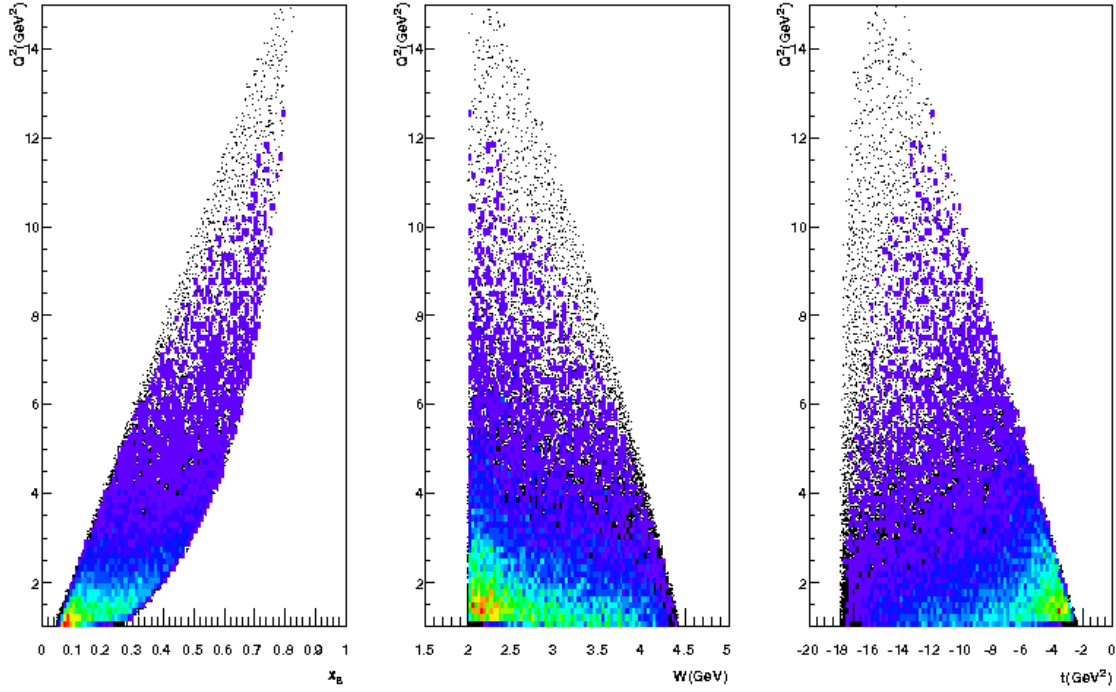


FIG. 45: Kinematic planes Q^2 vs x_B , W and t for the $ep \rightarrow ep\omega \leftrightarrow \pi^+\pi^-\pi^0 \leftrightarrow \gamma\gamma$ reaction. Black points: without any requirement on the detection of the particles. Colored points: with the requirement of the detection of an electron, a proton, a π^+ and a π^- in CLAS12 (using the CLAS12 FASTMC code)

Fig. 46 shows the (θ, E) phase spaces of the required detected particles in the final state: the electron, the proton, the π^+ and the π^- .

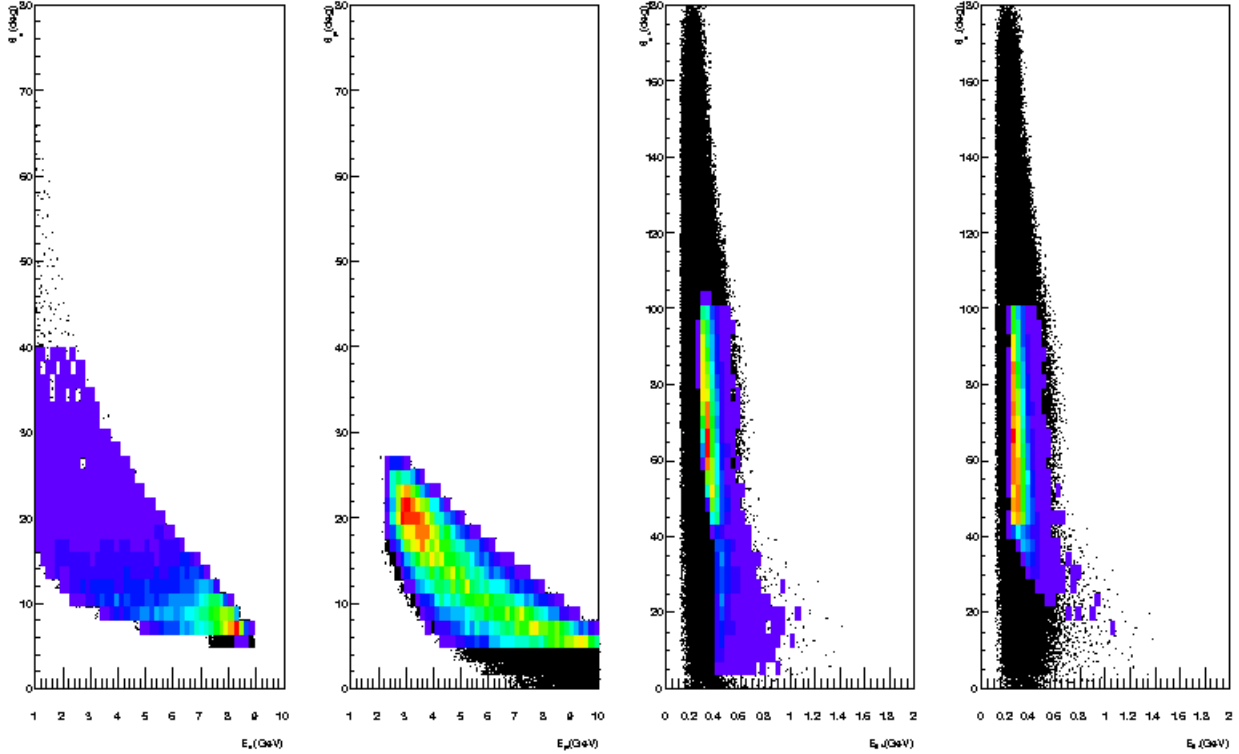


FIG. 46: Polar angle θ vs energy E for the electron (left panel), the proton, the π^+ and the π^- in the $ep \rightarrow ep\omega \leftrightarrow \pi^+\pi^-\pi^0 \leftrightarrow \gamma\gamma$ reaction according to our event generator. Black points: without any requirement on the detection of the particles. Colored points: with the requirement of the detection of an electron, a proton, a π^+ and a π^- in CLAS12.)

2. Acceptance

The acceptance of CLAS12 has been determined by again using the FASTMC code. We show in Fig. 47 the x_B , W , Q^2 and t distributions of the generated events (black lines) and those of the accepted events (red, green and blue lines). The red curve corresponds to the “topology”: electron, proton, π^+ and π^- detected in CLAS12. By making the ratio of these distributions, we see that the (integrated) acceptance values of CLAS12, determined by FASTMC, for the $ep \rightarrow ep\omega \leftrightarrow \pi^+\pi^-\pi^0 \leftrightarrow \gamma\gamma$ reaction are in average of the order of 1-2%, of course depending on the kinematics.

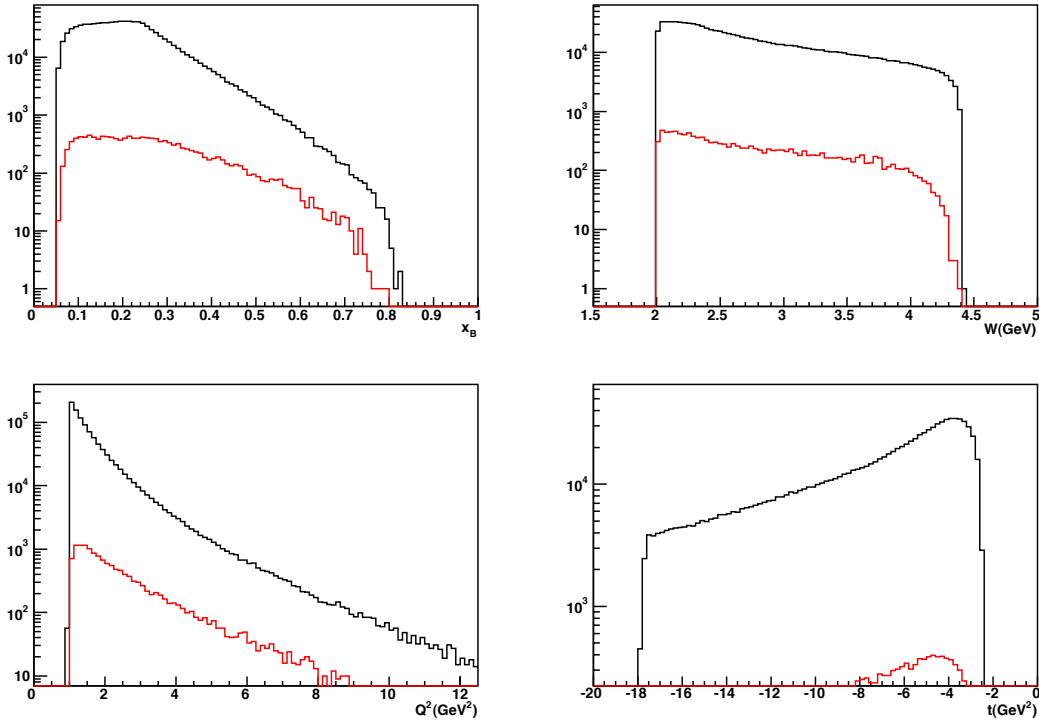


FIG. 47: Distributions of the generated events (black curves) and of the accepted events (red) in CLAS12, as determined by FASTMC, as a function of x_B , W , Q^2 and t . The red curve corresponds to the “topology” : an electron, a proton, a π^+ and a π^- detected in CLAS12.

VIII. BIBLIOGRAPHY

-
- [1] A. V. Efremov, A. V. Radyushkin, *Theor. Math. Phys.* **42**, 97-110 (1980).
 - [2] G. P. Lepage, S. J. Brodsky, *Phys. Rev.* **D22**, 2157 (1980).
 - [3] J. C. Collins, L. Frankfurt, M. Strikman, *Phys. Rev.* **D56**, 2982-3006 (1997). [hep-ph/9611433].
 - [4] D. Mueller, D. Robaschik, B. Geyer, F. M. Dittes, J. Horejsi, *Fortsch. Phys.* **42**, 101 (1994). [hep-ph/9812448].
 - [5] X. -D. Ji, *Phys. Rev.* **D55**, 7114-7125 (1997). [hep-ph/9609381].
 - [6] A. V. Radyushkin, *Phys. Rev.* **D56**, 5524-5557 (1997). [hep-ph/9704207].
 - [7] P. Faccioli, A. Schwenk, E. V. Shuryak, *Phys. Rev.* **D67**, 113009 (2003). [hep-ph/0202027].
 - [8] P. Schweitzer, M. Strikman, C. Weiss in preparation.

- [9] L. Frankfurt, M. V. Polyakov, M. Strikman, D. Zhalov, M. Zhalov, “Novel hard semiexclusive processes and color singlet clusters in hadrons,” [hep-ph/0211263].
- [10] B. Pire, K. Semenov-Tian-Shansky, L. Szymanowski, “A Spectral representation for baryon to meson transition distribution amplitudes,” Phys. Rev. **D82** (2010) 094030. [arXiv:1106.1851 [hep-ph]].
- [11] P. V. Pobylitsa, M. V. Polyakov, M. Strikman, Phys. Rev. Lett. **87**, 022001 (2001). [hep-ph/0101279].
- [12] M. Strikman, C. Weiss, “Exclusive electroproduction of strange mesons with JLab 12-GeV,” [arXiv:0804.0456 [hep-ph]].
- [13] S. V. Goloskokov and P. Kroll, Eur. Phys. J. C **42** (2005) 281; Eur. Phys. J. C **50** (2007) 829.
- [14] I. V. Anikin, D. Y. Ivanov, B. Pire, L. Szymanowski, S. Wallon, Nucl. Phys. **B828** (2010) 1-68. [arXiv:0909.4090 [hep-ph]].
- [15] S. V. Goloskokov, P. Kroll, Eur. Phys. J. **C42**, 281-301 (2005). [hep-ph/0501242].
- [16] M. S. Bhagwat, M. A. Pichowsky, C. D. Roberts and P. C. Tandy, Phys. Rev. **C68** (2003)
- [17] K. Goeke, M. V. Polyakov and M. Vanderhaeghen, Prog. Part. Nucl. Phys. **47**, 401 (2001).
- [18] M. Diehl, Phys. Rept. **388**, 41 (2003).
- [20] S. Ahmad, G. R. Goldstein, S. Liuti, Phys. Rev. **D79**, 054014 (2009), [arXiv:0805.3568 [hep-ph]].
- [20] S. Ahmad, G. R. Goldstein and S. Liuti, Phys.Rev.D79:054014,2009.
- [21] V. Belitsky, A.V. Radyushkin, Phys. Rept. **418**, 1 (2005).
- [22] L. L. Frankfurt, P. V. Pobylitsa, M. V. Polyakov and M. Strikman, “Hard exclusive pseudoscalar meson electroproduction and spin structure of a nucleon”, Phys. Rev. D **60**, 014010 (1999)
- [23] J. P. Lansberg, B. Pire, L. Szymanowski, “Hard exclusive electroproduction of a pion in the backward region’, Phys. Rev. **D75** (2007) 074004.
- [24] M. Vanderhaeghen, P.A.M. Guichon, M. Guidal, Phys. Rev. D **60**, 094017 (1999); M. Guidal, M. V. Polyakov, A. V. Radyushkin and M. Vanderhaeghen, Phys. Rev. D **72**, 054013 (2005).
- [25] M. Polyakov and C. Weiss, Phys. Rev. D **60** (1999) 114017.
- [26] Ahmed Fradi, (PhD thesis, University of Orsay (2009).
- [27] M. Guidal and S. Morrow, arXiv:0711.3743 (hep-ph), proceedings of the workshop ”Exclusive Reactions at High Momentum Transfer”, Jefferson Lab, 2007.

- [28] S.V. Goloskokov (Dubna, JINR), P. Kroll (Wuppertal U. and Regensburg U.) Published in Eur. Phys. J. **65** (2010) 137-151
- [29] F. Cano and J. M. Laget, Phys. Lett. B **551** (2003) 317.
- [30] K. Lukashin et al.(CLAS Collaboration) Phys. Rev. **C63:065205**,2001.
- [31] F. Cano and J-M. Laget, Nucl.Phys. A699 (2002) 356-359. arXiv:0209362(hep-ph)
- [32] J.P. Santoro et al. (CLAS Collaboration) Phys. Rev.**C78**,025210,(2008).
- [33] M. Guidal, J.-M. Laget and M. Vanderhaeghen, Nucl. Phys. **A 627**, 645 (1997).
- [34] P.D.B. Collins, T.D.B. Wilkie, (Durham U.) Z.Phys.C7:**357**,1981.
- [35] M. Diehl, W. Kugler, A. Schafer and C. Weiss. Phys.Rev.D72:034034,2005, Erratum-
ibid.D72:059902,2005.
- [36] S. A. Morrow et al., Eur. Phys. J. **A** (2009).
- [37] <http://www-hermes.desy.de/>, public plots, fig. 00-031.
- [38] D.G. Cassel et al., Phys. Rev. D **24** (1981) 2787.
- [39] K. Schilling and G. Wolf, Nucl. Phys. B **61** (1973) 381.
- [40] B.Lehmann-Dronke, P. V. Pobylitsa, M. V. Polyakov, A. Schaefer and K. Goeke, Phys. Lett. B 475 (2000) 14
- [41] B. Lehmann-Dronke, A. Schaefer, M. V. Polyakov and K. Goeke, Phys. Rev. D 63 (2001) 114001
- [42] V. M. Braun and N. Kivel, Phys.Lett. B501(2001) 48-53
- [43] N. Warkentin, M. Diehl, D. Yu. Ivanov, and A. Schaefer, Eur.Phys.J. A32 (2007) 273-291
- [44] M. Diehl, T. Gousset, B. Pire, and O.V. Terayev, [hep-ph/9901233]
- [45] I. Anikin, B. Pire, L. Szymanowski, O. Teryaev, and S. Wallon, Phys.Rev.D71:034021,2005.